The role of Cr and Mo alloying element additions on the kinetics and effects of Upper Bainite formation in quench and tempered plate steels

By

Lindsay Josephine Leach

Supervised by

Prof W.E. Stumpf and Dr C.W. Siyasiya

Submitted in partial fulfilment of the requirements for the degree of

Master of Science (Applied Science) Metallurgical Engineering

In the

Department of Materials Science and Metallurgical Engineering,

Faculty of Engineering, Built Environment and Information Technology,

University of Pretoria

South Africa

February 2013

UNIVERSITEIT VAN PRETORIA
UNIVERSITY OF PRETORIA
YUNIBESITHI YA PRETORIA

ACKNOWLEDGEMENTS

I would firstly like to thank God for the being an unfailing source of strength.

I extend my sincere gratitude to my supervisors Professor Stumpf and Dr Siyasiya for their insightful guidance and encouragement.

I thank my parents Joseph and Angeline Leach for the continuous love and support they give me.

The help of Carel Coetzee, Dr Kevin Banks and the staff of the Industrial Minerals and Materials Research institute in training of the SEM, Gleeble and Bähr dilatometer is greatly appreciated.

I wish to thank Louise Ackerman, Sarah Havenga and Elsie Snyman-Ferreira for their cheerful support in administrative matters.

The provision of financial support and provision of materials by ArcelorMittal South Africa is acknowledged.

I wish to thank Professor Robert Knutsen of The Centre for Materials Engineering at the University of Cape Town for assistance with their Instrumented Charpy testing unit.

I wish to thank Dr N. van der Berg of the Department of Physics, University of Pretoria for his discussions and help with shadowing of carbon extraction replica samples and Chris van der Merwe of the Laboratory for Microscopy and Microanalysis for his assistance with TEM microscopy.

Finally I extend my gratitude to my good friends Asimenya Kapito and Given Maruma whose companionship made the duration of this study a pleasant and memorable one.

UNIVERSITEIT VAN PRETORIA
UNIVERSITY OF PRETORIA
YUNIBESITHI YA PRETORIA

THE ROLE OF Cr AND Mo ALLOYING ELEMENT ADDITIONS ON THE KINETICS AND EFFECTS OF UPPER BAINITE FORMATION IN QUENCH AND TEMPERED PLATE STEELS

Supervisor: Professor WE Stumpf

Co-Supervisor: Doctor CW Siyasiya

Department: Materials Science and Metallurgical Engineering

Degree: Master of Science (Metallurgy)

ABSTRACT

The aim of the work presented was to investigate the effects of upper bainite on impact toughness in quench and tempered low alloy plate steels. The experimental research included construction of CCT diagrams by dilatometry, verification of phases by optical microscopy (OM), Vickers hardness, scanning electron microscopy (SEM), transmission electron microscopy (TEM) on precipitates extracted by carbon replica and by electrolytic means and finally impact testing of Charpy specimens with mixed bainite:martensite microstructures.

Bainite was formed in High Chromium Low Molybdenum (HCrLMo) and in High Molybdenum Low Chromium (HMoLCr) steel samples by isothermal annealing within the bainite C-curve of the respective CCT diagrams. The isothermal kinetics of the upper bainite transformation was modelled with the Johnson Mehl Avrami Kolmogorov (JMAK) model. Avrami exponents of 1.4 and 1.3 were obtained for the HCrLMo and HMoLCr steels respectively which indicated linear growth with a considerable lengthening rate of laths and negligible thickening.

The measurably slower growth kinetics in the HMoLCr steel as observed in the JMAK model and the higher hardenability with reference to its CCT diagram, suggested a strong Mo alloying element effect. The stronger effect of Mo compared to Cr was attributed to a solute drag like effect.

The effect of upper bainite in a tempered martensitic matrix was investigated for the following amounts of bainite; 0%, 10%, 25%, 60%, 75%, 90% and 100%. The impact toughness of the mixed bainite:martensite samples was evaluated against the toughness of 100% bainite and 100% martensite. It was demonstrated that upper bainite reduces the total

UNIVERSITEIT VAN PRETORIA
UNIVERSITY OF PRETORIA
YUNIBESITHI YA PRETORIA

absorbed impact energy by an adverse effect on crack nucleation energy and crack propagation energy.

Keywords: bainite, bainite:martensite structures, toughness, instrumented impact testing, dilatometry, isothermal transformation.

Publications and Conference Presentations

1. L.J. Leach, C.W. Siyasiya, W.E. Stumpf: Effect of dual phase microstructure on the toughness of a Cr-Mo low alloy plate steel – Presented at the Ferrous and Base Metals Development Network Conference, Magaliesburg, South Africa, 15-17 October 2012 – Published conference proceedings: Symposium series S73, Paper F09.
2. L.J. Leach, C.W. Siyasiya, W.E. Stumpf: Effect of dual phase microstructure on the toughness of a Cr-Mo low alloy plate steel – Accepted for publication in the Journal of the South African Institute of Mining and Metallurgy
3. L.J. Leach, C.W. Siyasiya, W.E. Stumpf: Effect of the alloying elements Cr and Mo on isothermal transformation kinetics in two plate steels – In preparation.

UNIVERSITEIT VAN PRETORIA
UNIVERSITY OF PRETORIA
YUNIBESITHI YA PRETORIA

Table of Contents

UNIVERSITEIT VAN PRETORIA
UNIVERSITY OF PRETORIA
YUNIBESITHI YA PRETORIA

UNIVERSITEIT VAN PRETORIA
UNIVERSITY OF PRETORIA
YUNIBESITHI YA PRETORIA

UNIVERSITEIT VAN PRETORIA
UNIVERSITY OF PRETORIA
YUNIBESITHI YA PRETORIA

UNIVERSITEIT VAN PRETORIA
UNIVERSITY OF PRETORIA
YUNIBESITHI YA PRETORIA

UNIVERSITEIT VAN PRETORIA
UNIVERSITY OF PRETORIA
YUNIBESITHI YA PRETORIA

Table of Figures

UNIVERSITEIT VAN PRETORIA
UNIVERSITY OF PRETORIA
YUNIBESITHI YA PRETORIA

UNIVERSITEIT VAN PRETORIA
UNIVERSITY OF PRETORIA
YUNIBESITHI YA PRETORIA

UNIVERSITEIT VAN PRETORIA
UNIVERSITY OF PRETORIA
YUNIBESITHI YA PRETORIA

UNIVERSITEIT VAN PRETORIA
UNIVERSITY OF PRETORIA
YUNIBESITHI YA PRETORIA

UNIVERSITEIT VAN PRETORIA
UNIVERSITY OF PRETORIA
YUNIBESITHI YA PRETORIA

UNIVERSITEIT VAN PRETORIA
UNIVERSITY OF PRETORIA
YUNIBESITHI YA PRETORIA

UNIVERSITEIT VAN PRETORIA
UNIVERSITY OF PRETORIA
YUNIBESITHI YA PRETORIA

List of Tables

List of Abbreviations

AQ	As quenched
B	Bainite

UNIVERSITEIT VAN PRETORIA
UNIVERSITY OF PRETORIA
YUNIBESITHI YA PRETORIA

BCC	Body Centred Cubic
BE	Back Scattered Electrons
CCT	Continuous Cooling Transformation
EDS	Energy Dispersive Spectroscopy
F	Ferrite
FCC	Face Centred Cubic
HCrLMo	High Chromium Low Molybdenum
HMoLCr	High Molybdenum Low Chromium
HSLA	High Strength Low Alloy
JMAK	Johnson Mehl Avrami Kolmogorov
M	Martensite
NMP	Mole fraction
NPLE	No Partition Local Equilibrium
OM	Optical Microscope
P	Pearlite
Q&P	Quench and Partitioned
RD	Rolling direction
SDLE	Solute Drag Like Effect
SE	Secondary Electrons
SEM	Scanning Electron Microscope
SN	Sympathetic Nucleation
TEM	Transmission Electron Microscope
TTT	Time Temperature Transformation

UNIVERSITEIT VAN PRETORIA
UNIVERSITY OF PRETORIA
YUNIBESITHI YA PRETORIA

UTS	Ultimate Tensile Strength
YS	Yield Strength

UNIVERSITEIT VAN PRETORIA
UNIVERSITY OF PRETORIA
YUNIBESITHI YA PRETORIA

1 Chapter 1

1.1 Introduction

Structural steels are produced on an industrial scale as plate steels which are hot rolled in a mill and then quenched and tempered to achieve their final strength. Due to their use, it is imperative that structural steels are manufactured to standards conforming to the desired qualities.

Firstly, good reliability is necessary as the steel undergoes fabrication processes involving bending, shearing, grinding, welding, drilling and punching without any detriment to its properties. Such properties include sufficient ductility, strength and notch toughness. Weldability is improved by limiting the addition of carbon to relatively low values, hence low carbon steels serve this purpose well, although comparable properties are obtained with High Strength Low Alloy steels (at a higher cost) and higher carbon mild steels. Alloy additions to the steels improve hardenability. In so doing, the quench severity may be reduced thus averting quench cracks. This is achieved by the addition of amounts of Manganese greater than 1% and smaller amounts of the strong carbide formers Chromium and Molybdenum as well as Boron, the latter to enhance the hardenability even more. Residual Sulphur reacts with the Mn and during hot rolling, and MnS stringers may develop. These compounds often result in non-isotropy of mechanical properties and so-called “shape control” additives such as Ca and Ce are often used to ensure rounded non-metallic inclusions.

Despite rigorous efforts to ensure good quality steel products, it may so happen that in one aspect or another, the product falls short of a certain requirement. When martensitic hardenability is insufficient in the centre of a steel plate it tends to have a different structure to the martensite that forms on the surface. Lower cooling rates within the centre result in greater retention of heat and the possibility of formation of a higher temperature transformation product is likely. This compromises the integrity of the material, firstly by the inhomogeneity of the material and secondly, by the type of additional transformation product that forms and the collective effect this imposes on the mechanical property requirements of

UNIVERSITEIT VAN PRETORIA
UNIVERSITY OF PRETORIA
YUNIBESITHI YA PRETORIA

the material. The stress systems to which the steel is exposed mostly require that strength and toughness are optimal and the steel must possess a good measure of resistance to failure. Therefore, a sufficient amount of ductility is desired in these steels as a signal of imminent collapse and a guarded measure against brittle fracture resistance. In this regard, microstructural properties exert a significant influence. The presence of inclusions, their morphology and distribution is also an important factor.

It is imperative that such plate steels manufactured for structural purposes possess reliability and integrity taking into consideration the factors that may influence or compromise the performance of the final product.

1.2 Problem statement

Plate steels with insufficient hardenability may consist of a combination of two phases, namely lath martensite and bainite. In many studies, dual phase microstructures of martensite and lower bainite are shown to have improved mechanical properties including strength and toughness [1, 2]. However, it is doubtful that the same can be said for dual phase upper bainite and martensite. This being so by the inherent structural difference that exists between upper and lower bainite. Therefore, this study endeavours to determine the quantitative effect of upper bainite in quench and tempered martensitic steel with regards to impact energy, thereby establishing the microstructural tolerances for quench and tempered plate steels.

UNIVERSITEIT VAN PRETORIA
UNIVERSITY OF PRETORIA
YUNIBESITHI YA PRETORIA

2 Chapter 2: Literature survey

There has been extensive research on the models of bainite formation and the factors that influence the transformation. This chapter is an overview of the literature on bainite characteristics and mechanical properties typical of steels with bainitic microstructures.

2.1 Alloying elements and the austenite to bainite transformation

Continuous Cooling and Isothermal Transformation diagrams are a powerful metallurgical tool as they are an accurate means of predicting microstructure-property relationships in steels, properties which are modifiable in accordance with the combination of alloying elements present. Equilibrium solubility temperatures/phases are altered such that the critical temperatures, i.e A_{c1} (equilibrium temperature at which austenite forms during heating), A_{c3} (temperature at which transformation of ferrite to austenite is complete), M_s (martensite start) and B_s (bainite start) temperatures are readily altered by these elements. This is proven in the quantitative empirical relationships between critical temperatures and alloying element combinations that have been established. Moreover, equilibrium phase regions in steels are enlarged or reduced by the relative amounts of alloying elements that are either ferrite formers or austenite formers.

Ferrite formers such as Cr, Si and Mo stabilise the ferrite regions and the austenite formers Ni, Mn and C stabilise the austenite regions. In addition to this, Ni, Cr and Mo are known to exert a significantly positive effect on the depth of hardenability. When added in sufficient quantities, V and Mo will form coherent carbides that are beneficial for strength while incoherent Cr carbides are beneficial for improved wear-resistance. However, small additions of Mo and particularly Boron for instance, retard the austenite to ferrite and pearlite transformations thus allowing bainite to form more readily, see Figure 2.1.1. Additions of 0.3 and 0.6wt% Mo to a High Strength Low Alloy (HSLA) steel increase the amount of bainite that forms.

UNIVERSITEIT VAN PRETORIA
UNIVERSITY OF PRETORIA
YUNIBESITHI YA PRETORIA

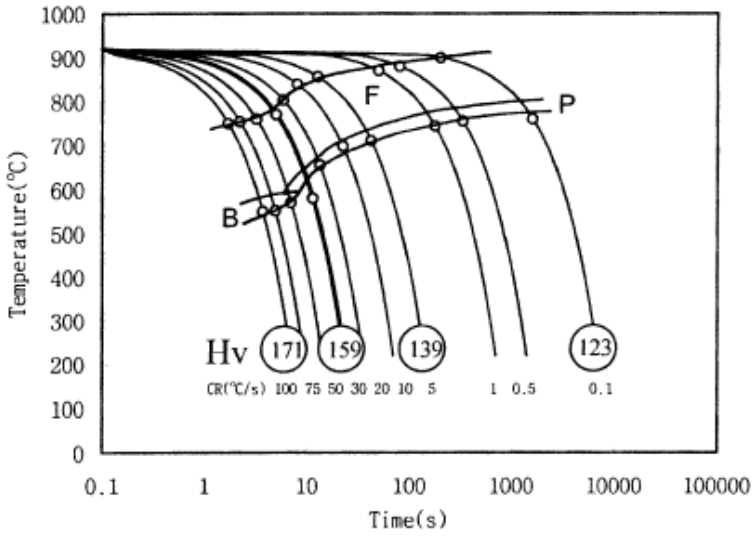

(*a*)

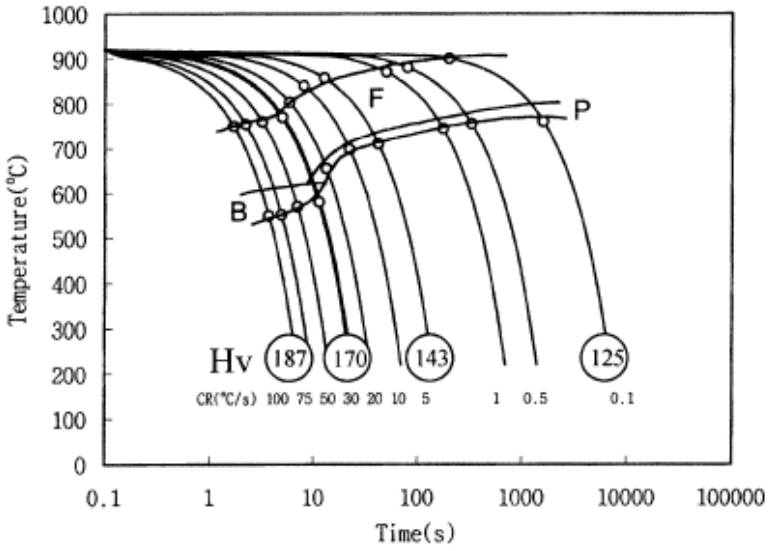

(*b*)

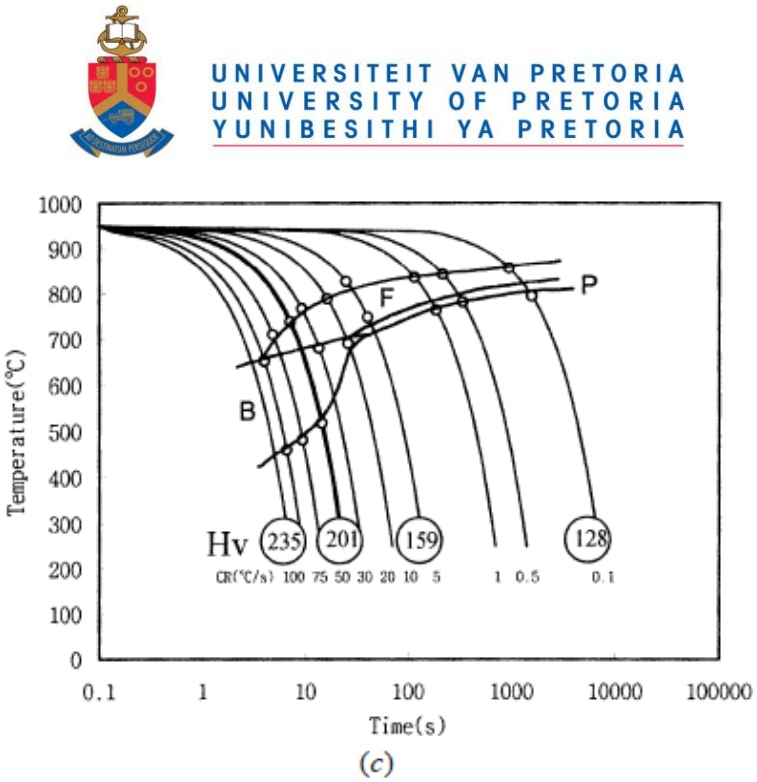

Figure 2.1.1 Effect of Mo additions to a Low Alloy steel with (a) 0.03wt% Nb (b) 0.03wt% Nb-0.3wt% Mo and (c) 0.03wt% Nb-0.6wt% Mo [3].

Small amounts of boron remarkably increase the steel's hardenability, thus reducing the amount of expensive alloying element additions required, i.e. Cr, Mo or Ni. The hardenability effect with additions of between 10 and 30 ppm of boron is caused by the segregation of solute boron to austenite grain boundaries where it reduces the interfacial energy between austenite grains and thus slows the nucleation of pro-eutectoid ferrite and pearlite on these grains. Formation of $Fe_{23}(C,B)_6$ or $M_{23}(C,B)_6$ by excessive amounts of boron (generally 50 ppm and higher) at the austenite grain boundaries severely deteriorates hardenability because the boro-carbide is a nucleation site for ferrite [4].

As mentioned above, the main mechanism responsible for boron hardenability is that it reduces preferential sites for ferrite nucleation by reduction of the grain boundary energy, i.e. a thermodynamic effect. However, other mechanisms proposed for the hardenability effect [4] are that;

1) The self-diffusion coefficient of iron at grain boundaries is reduced and thus the ferrite nucleation rate is also reduced, i.e. a kinetic effect;

2) The very act of boron segregation to austenite grain boundaries eliminates preferential sites for ferrite nucleation (thermodynamic effect) and

UNIVERSITEIT VAN PRETORIA
UNIVERSITY OF PRETORIA
YUNIBESITHI YA PRETORIA

3) Fine borides that are coherent with the matrix form along the boundaries, eliminating ferrite nucleation between the boride and matrix, i.e. a structural thermodynamic effect.

During quenching, quenched-in vacancies allow for the formation and diffusion of the vacancy-boron complex into the grain boundary and boron is thus prevented from returning to the grain interior [5].

Boron segregation can also lead to the formation of BN, Fe_2B and oxides. Low alloy steels usually contain small amounts of boron; 0.001 – 0.003wt.% [6]. Boron in such quantities slows the austenite decomposition which allows for lower quenching rates.

In the intermediate temperature range where bainite forms, the austenite grain boundary is thus stabilised by boron. This causes a lowering of the upper limiting temperature of the C-curve for bainite, i.e. the B_s [7]. In addition to decreasing the B_s temperature, there is an increase in the proportion of bainite obtainable and a refinement of the lath size with boron additions [4].

A long holding time causes boron segregation and subsequent precipitation of borides at austenite grain boundaries. Such an excessive amount of boron drastically decreases the steel's hardenability. Hardenability initially increases with increasing boron content up to an optimum boron level after which no improvement and even a decline in its effectiveness is found [5]. In combination with Mo, the optimum amount of boron increases as the addition of Mo retards the precipitation of the boro-carbides $M_{23}(C,B)_6$ [8]. In the execution of an experiment to determine austenitising temperature effects on boron segregation in alloys soaked at 900℃, boron led to no observable precipitation while those austenitised at 1100℃ had boro-carbides on their grain boundaries [5]. Therefore, an optimal boron concentration is generally considered to be between 10 and 30 ppm to ensure enhanced hardenability.

Cementite formation in bainite is delayed by high Al or Si content, usually in amounts exceeding 1wt% for Si. Consequently, the resulting microstructure is described as "carbide-free" bainite [9-12]. It is interesting that a study on a no Si-containing alloy showed that the bainitic ferrite subunits grow at a considerably higher rate with regards to plate lengthening than bainitic ferrite in which interlath carbide formation is supressed by the addition of Si

UNIVERSITEIT VAN PRETORIA
UNIVERSITY OF PRETORIA
YUNIBESITHI YA PRETORIA

[13]. The reason proposed is that the carbides are additional sinks for carbon in close proximity to the bainitic ferrite and thus increase the driving force for ferrite growth. It is thought after the first ferrite plate forms, further development is triggered by the carbide, which in turn triggers nucleation of another ferrite lath and so forth. When measured against Widmanstätten ferrite, which is considered the carbide-free analogue to upper bainite because of the orientation relationship of the ferrite plates with the matrix, the latter has even higher growth rates. It would, therefore, seem that the difference arises from the formation of the carbides, which seem to accelerate the growth rate of bainite [12].

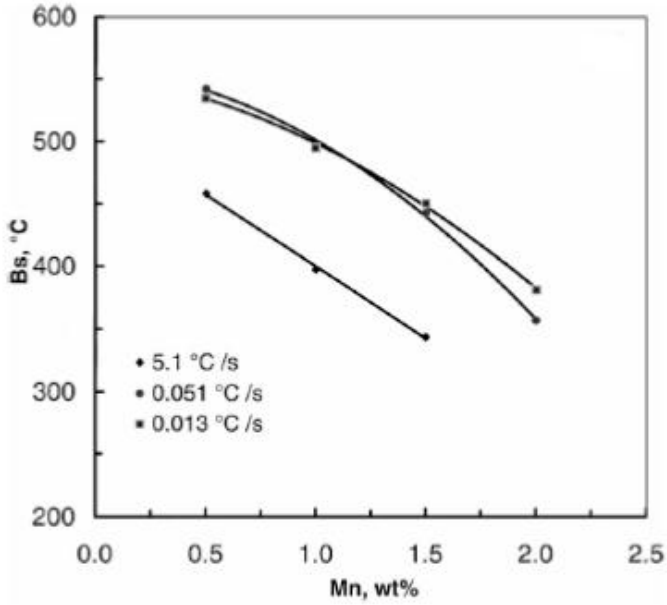

(a)

UNIVERSITEIT VAN PRETORIA
UNIVERSITY OF PRETORIA
YUNIBESITHI YA PRETORIA

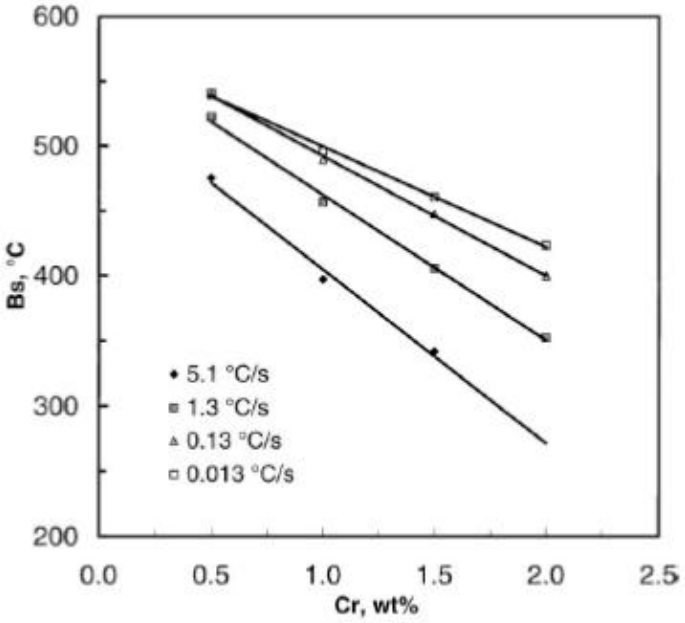

(b)

Figure 2.1.2 The effects of (a) Mn and (b) Cr on the B_s temperature as determined by Artificial Neural Network (ANN) modelling [14].

Mn decreases the free energy difference between ferrite and austenite as it is a strong austenite stabiliser and the incubation period is then prolonged by the decrease in Gibbs free energy. The effect of Mn on the B_s is shown in Figure 2.1.2 (a).

Cr is highly effective in reducing the B_s (Figure 2.1.2 (b)) and increasing the incubation period of the bainite reaction. However, Mn is more effective in shifting the bainite region towards longer times in the CCT diagram.

Si and Al function by removing any oxygen present in the steel. In addition to this, Si has also been shown to suppress the formation of cementite during the austenite to bainite transformation resulting in a carbide-free bainite [15]. Si suppresses the B_s slightly and decreases the overall reaction kinetics of bainite formation.

Another beneficial quality of Al is the formation of its nitride, AlN. When it is formed, this compound binds the free nitrogen and thus reduces the free nitrogen content of the steel which would otherwise be detrimental to ductility and toughness because of the embrittlement effect of free nitrogen in a ferritic lattice.

UNIVERSITEIT VAN PRETORIA
UNIVERSITY OF PRETORIA
YUNIBESITHI YA PRETORIA

Titanium forms a stable nitride. When used in combination with Boron, the steel's hardenability is further improved by alleviating Boron-Nitride formation and thus promoting the existence of elemental Boron.

2.2 Kinetics

2.2.1 Nucleation and growth transformations

In a reaction where nucleation occurs homogeneously, the volume transformed from (V) to a new phase (V^{β}) after a time interval t is proportional to the untransformed volume and can be expressed as a first order rate process:

$$\frac{dV^{\beta}}{dt} = k(V - V^{\beta}) \qquad \text{eq 2.1}$$

where k is the rate constant.

A particle will originate at a time τ, known as the incubation period, before which there is no detectable growth. Thus at $t > \tau$ the volume of new phase υ_τ is given by $\upsilon_\tau = Y_1Y_2Y_3\,(t - \tau)$ where Y_i represent principle growth velocities in three mutually perpendicular directions [16]. At the early stages of transformation, there is no interference between the growth fronts of the new β phase. Thus at an interval between the incubation $t = \tau$ and $t = \tau + d\tau$ the volume fraction of transformation product becomes:

$$dV_e = \upsilon_\tau V_o {}^{v}I\, d\tau \qquad \text{eq 2.2}$$

where V_e is the extended volume, V_o the untransformed volume and ${}^{v}I$ is the nucleation rate per unit volume. Extended space is defined as regions where particles can grow through each other and where particles can nucleate in areas which are already transformed [17]. The new phase in the untransformed regions is given by $dV = (1 - \frac{V}{V_o})\, dV_e$ which becomes:

$$\frac{dV}{V_o - V} = \upsilon_\tau {}^{v}I\, d\tau$$

Integrating the above expression and setting $X = \frac{V}{V_o}$ leads to:

UNIVERSITEIT VAN PRETORIA
UNIVERSITY OF PRETORIA
YUNIBESITHI YA PRETORIA

$$\ln(1-X) = -\int_0^{\tau} 0\, d\tau - \int_{\tau}^{t} \eta\, Y_1 Y_2 Y_3\, \nu I (t-\tau)^3 d\tau$$

where η is a shape factor. Assuming that $^{\nu}I$ is constant, the general expression obtained is:

$$V = 1 - \exp(-kt^n) \qquad \text{eq 2.3}$$

The general equation 2.3, known as the Johnson Mehl Avrami Kolmogorov equation, can be applied to most S-shaped transformation curves. It is based on the supposition that the growing regions do not interfere with each other and case of impingement between growing regions is dealt with by the concept of extended volume fraction proposed by Avrami [16].

2.2.2 The Johnson Mehl Avrami Kolmogorov equation

In the JMAK equation (eq 2.3) k is a temperature dependent constant given by:

$$k = \frac{1}{4}\eta Y_1 Y_2 Y_3\, ^{\nu}I \qquad \text{eq 2.4}$$

where R is the gas constant in kJ/mol.K and T is the absolute temperature and Q is the activation energy. The time exponent n for bainite is a dimensionless quantity generally having values ranging from 1 to 4 for most transformations [16].

Equation 2.3 models the time dependence of an isothermal phase transformation and at different isothermal transformation temperatures, the activation energy Q for the mechanism of the phase formation can be derived from equation 2.4.

The physical interpretation of the exponent n (which is derived from the slope of the graph of $\ln\ln(1/(1-V_f))$ against $\ln t$) is that it accounts for the dimensionality of the growth. Pearlite, for instance has been found to have an *n*-value of 4 [17], which represents constant nucleation rate and three dimensional growth of pearlite at grain corners. Bainite on the other hand has been found to have n values of roughly 2 [18], which is indicative of a constant nucleation rate and linear growth. The lengthening of bainite plates is faster relative to the thickening of the plates which is said to occur after growth has reached completion, hence growth is regarded as one dimensional.

UNIVERSITEIT VAN PRETORIA
UNIVERSITY OF PRETORIA
YUNIBESITHI YA PRETORIA

Possible values of the constant n are given in the table below. It is often used as a criterion of the mechanisms that accompany a transformation. A change in the value of n in a given transformation is indicative of a change in mechanism though it cannot be used to predict the exact nature of the transformation mechanism.

Table 2.1 Avrami exponents in relation to nucleation and growth

Conditions	n
All shapes growing from small dimensions, increasing nucleation rate	$>2\frac{1}{2}$
All shapes growing from small dimensions, constant nucleation rate	$2\frac{1}{2}$
All shapes growing from small dimensions, decreasing nucleation rate	$1\frac{1}{2}$ - $2\frac{1}{2}$
All shapes growing from small dimensions, zero nucleation rate	$1\frac{1}{2}$
Growth of particles of appreciable initial volume	1 - $1\frac{1}{2}$
Needles and plates of finite long dimensions, small in comparison with their separation	1
Thickening of long cylinders (needles) (e.g. after complete edge impingement)	1
Thickening of very large plates (e.g. after complete edge impingement)	$\frac{1}{2}$
Precipitation on dislocations (very early stages)	$\sim\frac{2}{3}$

For transformations occurring in a thin sheet, growth along the plane of thickness is over relatively fast. The reaction is then considered to be two dimensional and the growth rate previously expressed in terms of the three mutually perpendicular planes is now confined to two planes. That is to say, the growth rate is proportional to $\eta Y_1\ Y_2\ (t - \tau)^2$. Values of the exponent n in this case are limited to between 2 and 3. Similarly, in a thin wire, growth is confined to a direction along the length of the wire and is thus one-dimensional. The value of n is now between 1 and 2.

The experimental value of n obtained is partly influenced by the method used. A technique which records information in one dimension, such as length change, measures the transformation kinetics in that direction alone and the resulting n is between 1 and 2 as for a one-dimensional transformation. Maintaining three-dimensional results would require

UNIVERSITEIT VAN PRETORIA
UNIVERSITY OF PRETORIA
YUNIBESITHI YA PRETORIA

sampling in all 3 directions [16]. Although n is regarded as a constant, some studies have shown a temperature dependence of n [16, 19] as shown in Figure 2.2.1.

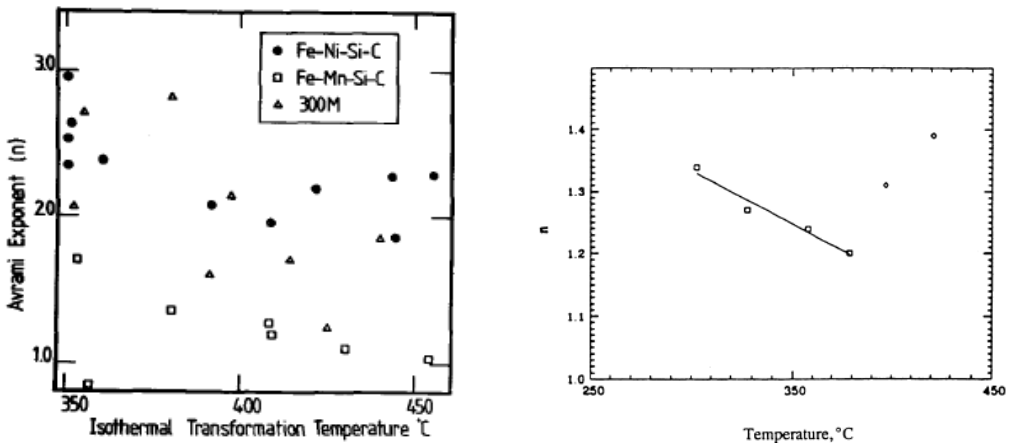

(a) (b)

Figure 2.2.1 Temperature dependence of the Avrami exponent n (a) in Fe-Ni-Si-C, Fe-Mn-Si-C and 300M steels [19] and (b) in a 0.66%C steel [16].

The assumptions on which the JMAK equation is based are that of random nucleation, constant nucleation rate, three dimensional growth and constant growth rate. The value of n is thus a function of the nucleation rate and the type of site at which nucleation occurs. The increasing *n*-values shown in Figure 2.2.1 by Fang et al [16] were found to be due to an increase in the number of nucleation sites.

When the formation of bainite is modelled with the JMAK equation, generally an exponent of 1 or 2 is found. Fang et al [16] used n as a transformation sensitive parameter in a 0.69wt% C steel to determine the temperature limits of a transformation product and obtained separate C-curves for upper and lower bainite but with some overlap. However, there is not always a transition in the value of the exponent n as the transformation temperature changes from upper bainite to lower bainite [18] as was found for the medium carbon steel (see Figure 2.2.3) studied by Caballero et al [18].

When modified to suit non-isothermal conditions, it is shown that the Avrami exponent is still a useful parameter in a qualitative assessment of the kinetics. Gupta et al [20] showed that each cooling rate yields a specific exponent and that its change with a decrease in cooling

UNIVERSITEIT VAN PRETORIA
UNIVERSITY OF PRETORIA
YUNIBESITHI YA PRETORIA

rates is related to the morphological changes of the transformation product. A cooling rate of 105℃/min gave an exponent of 1, indicating one dimensional growth. The corresponding microstructure was one of bainitic ferrite plates with interlath films of retained austenite. At much lower cooling rates an Avrami exponent of 3 was obtained. The corresponding bainite microstructure was coarser than that at higher cooling rates, indicating significant thickening of the bainite laths.

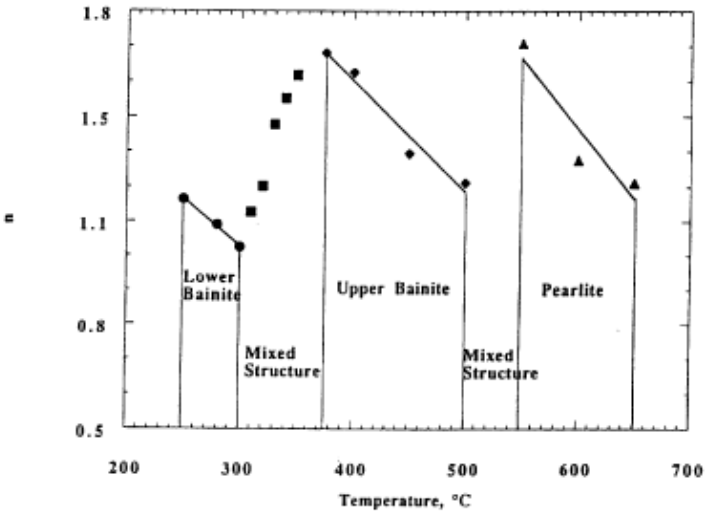

UNIVERSITEIT VAN PRETORIA
UNIVERSITY OF PRETORIA
YUNIBESITHI YA PRETORIA

Figure 2.2.2 Correlation of Avrami exponents with temperature and transformation products [16].

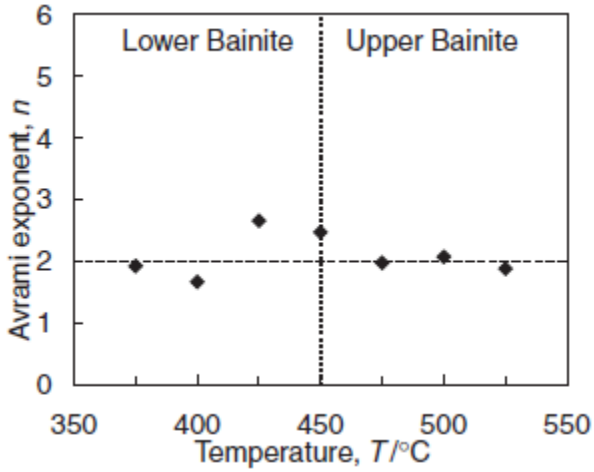

Figure 2.2.3 Average Avrami exponent n of 2 is shown for both upper and lower bainite in a 0.31C-1.22Mn-0.25Si-0.14Cr-0.10Ni steel (in wt%) [18].

In the work done by Caballero et al, the Avrami exponents obtained for upper and lower bainite structures in a medium carbon steel were found to be close to 2 [18]. They indicated that the bainitic reaction occurred by linear growth of ferrite plates nucleated at a constant rate on the austenite grain surfaces. Thickening of the plates was negligible relative to their lengthening. The two bainite morphologies were not distinguishable by any significant difference between their *n* values [18].

In another study [21] it was found that lower and upper bainite possessed different *n* values with the former generally possessing higher *n* values than the latter. The observation was made on six different alloy steels, shown in Table 2.2. The variation in Avrami exponents was interpreted as being the result of different transformation mechanisms.

Table 2.2 n values obtained for upper and lower bainite in different alloy steels [21].

n	Steels					
Structures	15CrMnMoV	18Cr2Ni4W	30CrMnSiNi2	40CrMnSiMoV	GCr15	9CrSi
Granular structure	3.8	2.0	---	---	---	---
Upper bainite	3.5	1.8	3.5	2.0	6.4	3.3
Lower bainite	1.7	0.6	2.8	0.6	4.2	2.4

UNIVERSITEIT VAN PRETORIA
UNIVERSITY OF PRETORIA
YUNIBESITHI YA PRETORIA

2.3 Bainite formation models

2.3.1 General features

Bainite is referred to generally as a non-lamellar aggregate of ferrite and carbide to distinguish it from pearlite. Crystallographic mechanisms and features of bainitic and Widmanstätten ferrite are similar according to Bhadeshia et al with the exception being that the latter is formed with carbon diffusion as the rate limiting factor and the former without carbon diffusion [12]. Due to the marked similarities that exist between bainite and martensite and Widmanstätten ferrite, various postulates have been brought forward on the mechanisms of bainite formation.

Figure 2.3.1 is an illustration of a widely accepted mechanism for bainite formation. In high silicon steels, carbide precipitation is suppressed or even eliminated, consequently, the transformation mechanism is believed to involve only the nucleation of ferrite sheaves [22, 23]. This is utilised commercially in the manufacture of steels with a high level of resistance to cleavage fracture and void formation.

UNIVERSITEIT VAN PRETORIA
UNIVERSITY OF PRETORIA
YUNIBESITHI YA PRETORIA

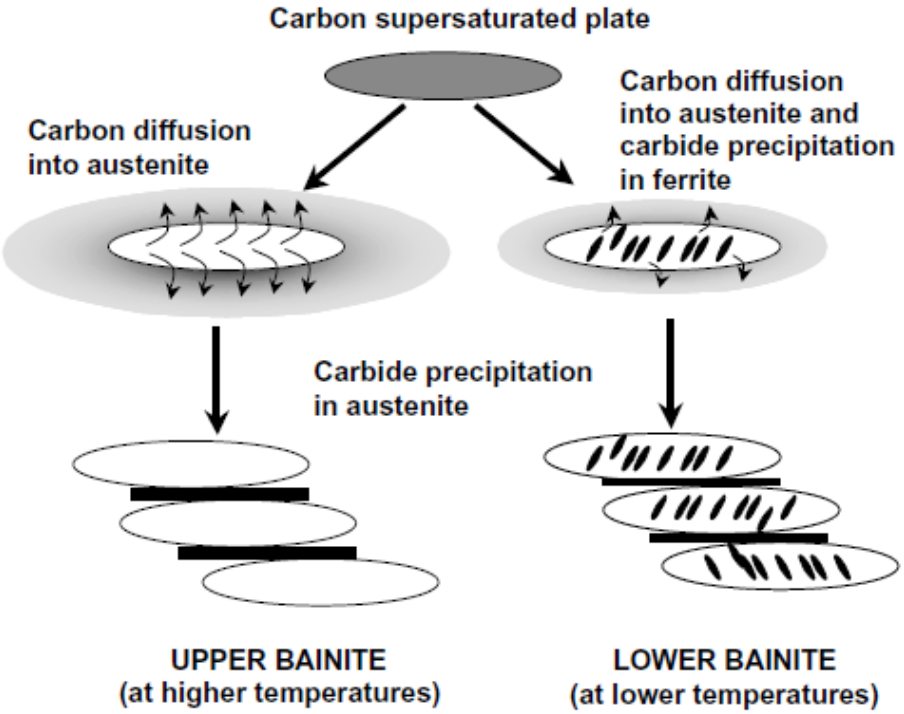

Figure 2.3.1 The mechanism of formation of upper and lower bainite [23].

According to some authors, the transformation mechanisms for upper and lower bainite are not fundamentally dissimilar. Bainitic ferrite grows with a supersaturation of carbon in both cases but it is in the partitioning of the surplus carbon from the ferrite into the residual austenite or its precipitation within the ferrite where the difference arises. The prevalence of either process will determine the type of bainite obtained. Moreover, the faster the partitioning of carbon into the untransformed austenite, the less likely is precipitation within the ferrite and the more likely structure is upper bainite. Hence at temperatures in the region of the lower bainite start temperature, it is possible to obtain both upper and lower bainite in a microstructure as in Figure 2.3.2 below [18].

UNIVERSITEIT VAN PRETORIA
UNIVERSITY OF PRETORIA
YUNIBESITHI YA PRETORIA

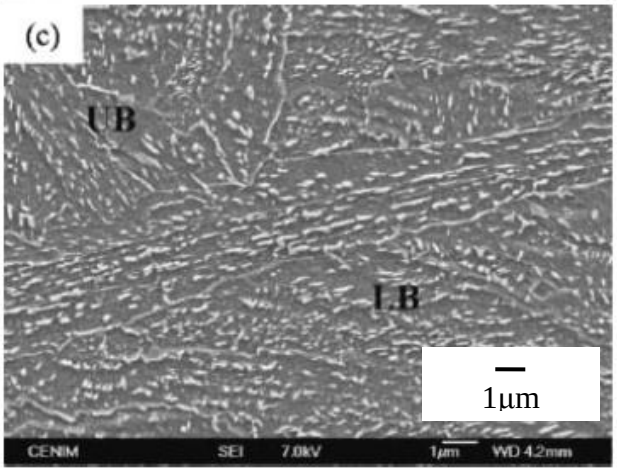

Figure 2.3.2 SEM of a Medium Carbon steel isothermally transformed for 900s at 450^{0}C [18]. UB is upper bainite and LB is lower bainite.

At the transition temperature between upper and lower bainite, which is believed to be at 350℃ [11, 24], the kinetics of the bainite reaction changes. It is thus possible to form both upper and lower bainite at temperatures in the region of the transition temperature.

The transition temperature from upper to lower bainite is not a fixed value as it varies with the carbon content. As can be seen from Figure 2.3.3 the transition temperature initially increases to a maximum before decreasing to a stable value.

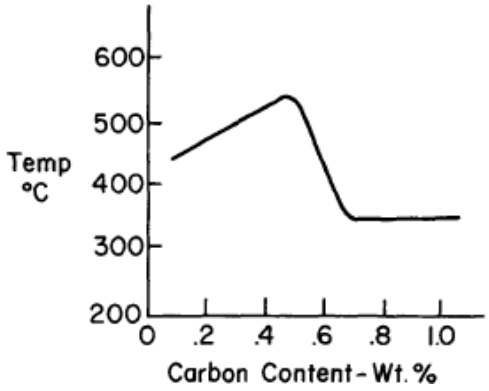

Figure 2.3.3 The transition temperature between upper and lower bainite as a function of carbon content [25].

The width of a bainitic ferrite plate increases with the isothermal transformation temperature as shown in Figure 2.3.4. At higher isothermal transformation temperatures, the yield strength of the austenite decreases and therefore there is plastic relaxation in the austenite bordering

UNIVERSITEIT VAN PRETORIA
UNIVERSITY OF PRETORIA
YUNIBESITHI YA PRETORIA

the newly formed bainite plates, allowing the plates to widen more. Dislocations are thus induced in the austenite and they pose a resistance to the advance of the bainite:austenite interface [18].

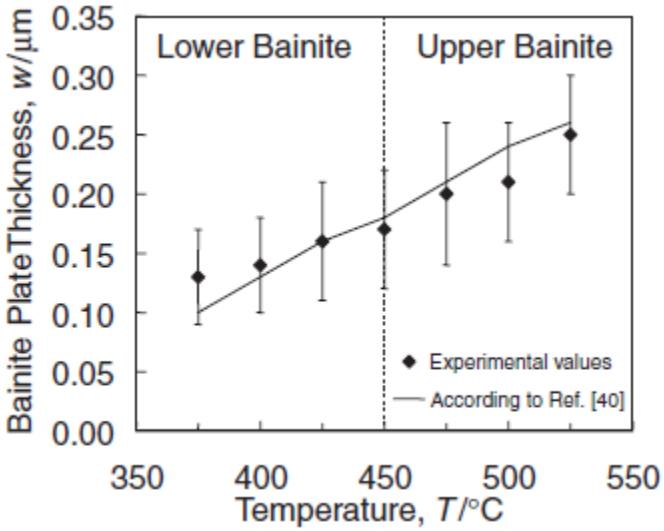

Figure 2.3.4 The decrease of ferrite plate thickness with decreasing isothermal treatment temperature of a medium carbon steel [18].

2.3.1.1 Lower bainite

The two main morphological variants of bainite (upper bainite and lower bainite) are distinguishable by the precipitation and distribution of the iron carbide. Lower temperatures of formation lead to a finer carbide dispersion within the ferrite laths. Lower bainite, as shown in the SEM micrographs of Figures 2.3.5 and 2.3.6 below, has plate-like carbides aligned at an angle of approximately 55° to the long axis of the ferrite lath due to their orientation relationship with specific crystallographic ferrite planes. The carbide may be ε-carbide ($Fe_{2.4}C$) or cementite and precipitates within the ferrite lath and thus precipitation is from ferrite rather than austenite. It is presumed that this is a result of the lower carbon diffusion rates at the reduced temperatures at which lower bainite forms, whereby rejection of carbon atoms into the adjacent austenite is delayed.

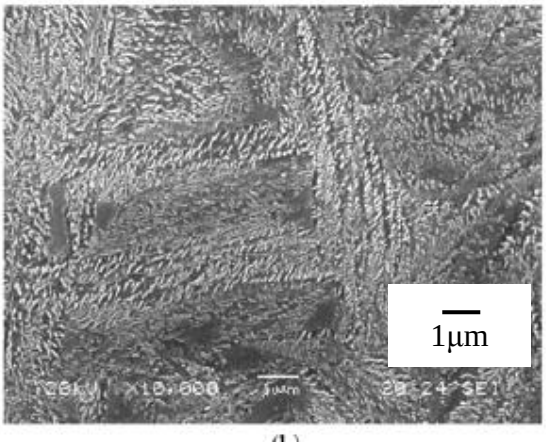

Figure 2.3.5 SEM micrograph of lower bainite in a 2358 steel austempered at 260℃ for 100 minutes [26].

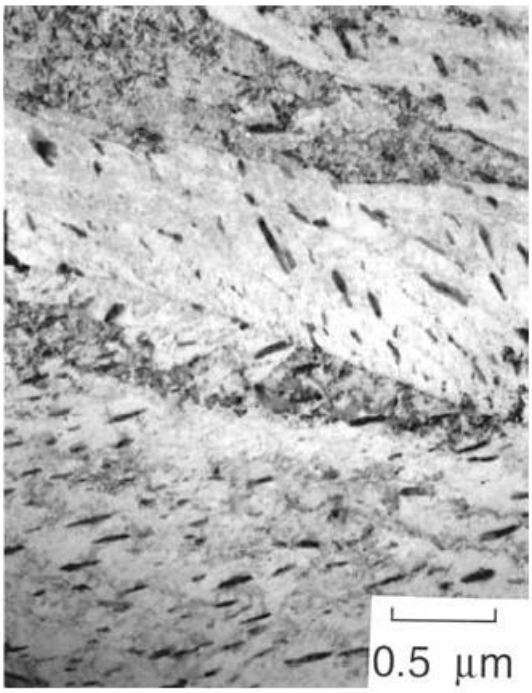

Figure 2.3.6 TEM micrograph of lower bainite showing the parallel intralath carbides within ferrite laths [27].

UNIVERSITEIT VAN PRETORIA
UNIVERSITY OF PRETORIA
YUNIBESITHI YA PRETORIA

2.3.1.2 Upper bainite

Upper bainite is distinguishable from lower bainite by the distribution of carbides that lie along and between the ferrite laths. The cementite precipitates from the carbon enriched austenite between the ferrite laths [22, 27]. Lower bainite is predominantly plate-like whereas upper bainite forms elongated laths. The laths grow from austenite grain boundaries in a Kurdjumov Sachs orientation relationship [28]. Each lath grows by repeated nucleation of ferrite subunits which grow to a limited size and collectively form a sheaf, as Figure 2.3.7 shows.

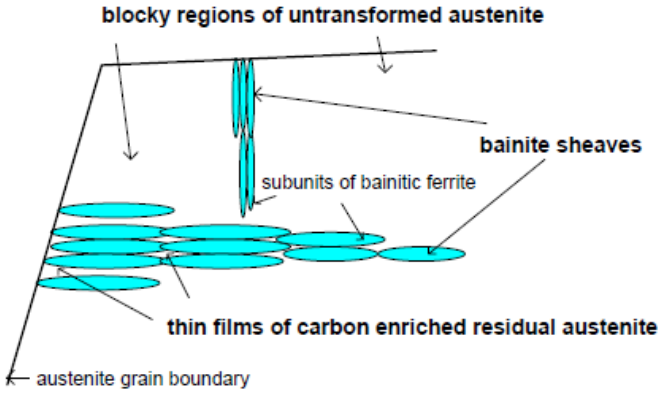

Figure 2.3.7 Formation of upper bainite by repeated nucleation of sheaves [28]

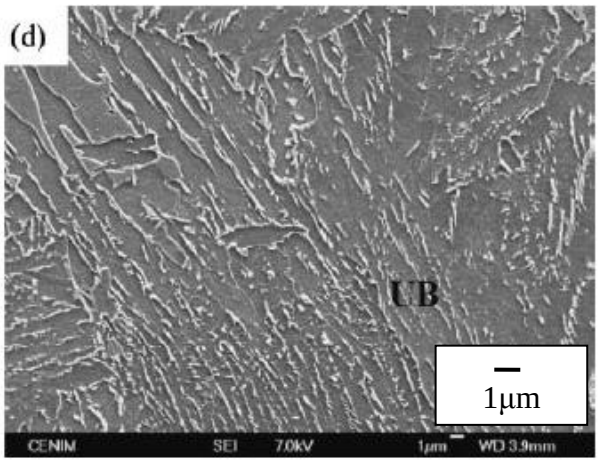

Figure 2.3.8 SEM micrograph of upper bainite in a 0.31C-1.22Mn-0.14Cr-0.25Si steel isothermally transformed at 525℃ for 900s [18].

Whilst the ferrite plates of lower bainite have a high aspect ratio, increased thickness of the plates and thus smaller aspect ratios are characteristic of upper bainite [29]. The SEM

UNIVERSITEIT VAN PRETORIA
UNIVERSITY OF PRETORIA
YUNIBESITHI YA PRETORIA

micrograph of Figure 2.3.8 shows upper bainite in a 0.31C-1.22Mn-0.14Cr-0.25Si steel. Higher micro-hardnesses (295-315 HV) were found for a lower bainite structure which consists of small sheaves of straight laths with thicknesses less than 1µm. Coarser bundles of lower hardnesses (240-265 HV) and wider laths on the other hand, characterised upper bainite [30].

2.3.2 The Displacive model

In the context of a displacive transformation, bainitic ferrite forms by a shear mechanism and the subsequent precipitation of carbides is a secondary reaction which occurs by diffusion of carbon into the residual austenite [19, 28, 31]. In accordance with shear or martensitic transformation characteristics, the bainitic transformation is diffusionless and occurs by the coordinated movement of atoms [28]. The transformation shares some characteristics of the martensite formation.

Displacive transformations, such as is proposed for the bainite reaction, involve the simultaneous shear transformation of a substitutional lattice and diffusion of interstitial species, which in this case is carbon. The main features between bainite and martensite are compared in Table 2.3.

Table 2.3 Comparison of the transformation characteristics of bainite α_b with martensite α' and Widmanstätten ferrite α_w [28].

	α'	α_b	α_w
Nucleation and growth reaction	√	√	√
Plate shape	√	√	√
Diffusionless nucleation	√	×	×
Carbon diffusion during	×	√	√
Substitutional diffusion during	×	×	×
Confined to austenite grains	√	√	√
Large shear	√	√	√
Invariant plane strain shape	√	√	√
Diffusionless growth	√	√	×
Carbon diffusion during growth	×	×	√
Substitutional diffusion during	×	×	×
Glissile interface	√	√	√

UNIVERSITEIT VAN PRETORIA
UNIVERSITY OF PRETORIA
YUNIBESITHI YA PRETORIA

Consistency of a comment with the transformation concerned is indicated by $(\surd)$, *inconsistency by* $(\times)$.

The growth is initially diffusionless [22] and the upper limiting temperature at which bainite forms is T_o, which is defined as the temperature at which austenite and ferrite of the same composition have equal free energies. Figure 2.3.9 shows a schematic illustration of the T_o curve on a phase diagram. The stored energy of 400 J/mol due to the invariant plane strain change in shape during the formation of bainitic ferrite is accounted for in the T_o' curve. The T_o curve on a temperature/carbon plot has a negative slope, showing that austenite can accommodate more carbon at lower temperatures. According to Bhadeshia et al [27] there is no diffusion of substitutional solute elements and their effect is only a thermodynamic shift in the T_o. The majority of alloying elements decrease the carbon concentration at the T_o curve except for Si, Al and Co, which increase the carbon concentration [23]. Alloying elements shift the T_o curve thus the maximum possible carbon concentration in retained austenite can be optimised.

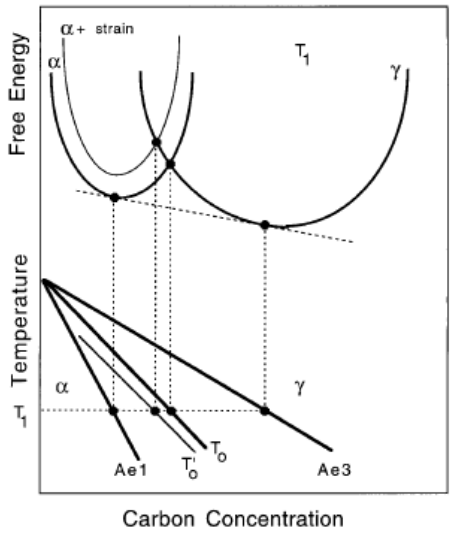

Figure 2.3.9 Diagram of austenite and ferrite free energies and T_o curve on the phase diagram.

2.3.2.1 Surface Relief

The formation of both upper and lower bainite is accompanied by a martensite-like surface relief typical of invariant plane strain deformation. It is thus thought that the surface relief of

UNIVERSITEIT VAN PRETORIA
UNIVERSITY OF PRETORIA
YUNIBESITHI YA PRETORIA

bainite is evidence of a displacive or shear-driven transformation mechanism akin to a martensitic transformation. According to the displacive mechanism, bainite is a transformation product resulting from cooperative movement of atoms which produces growth by shear. The austenite:ferrite interface moves without any thermal activation and the reaction is initially diffusionless and involves high growth rates given the absence of a temperature dependence [32]. Figure 2.3.10 shows the surface relief that develops when bainite forms.

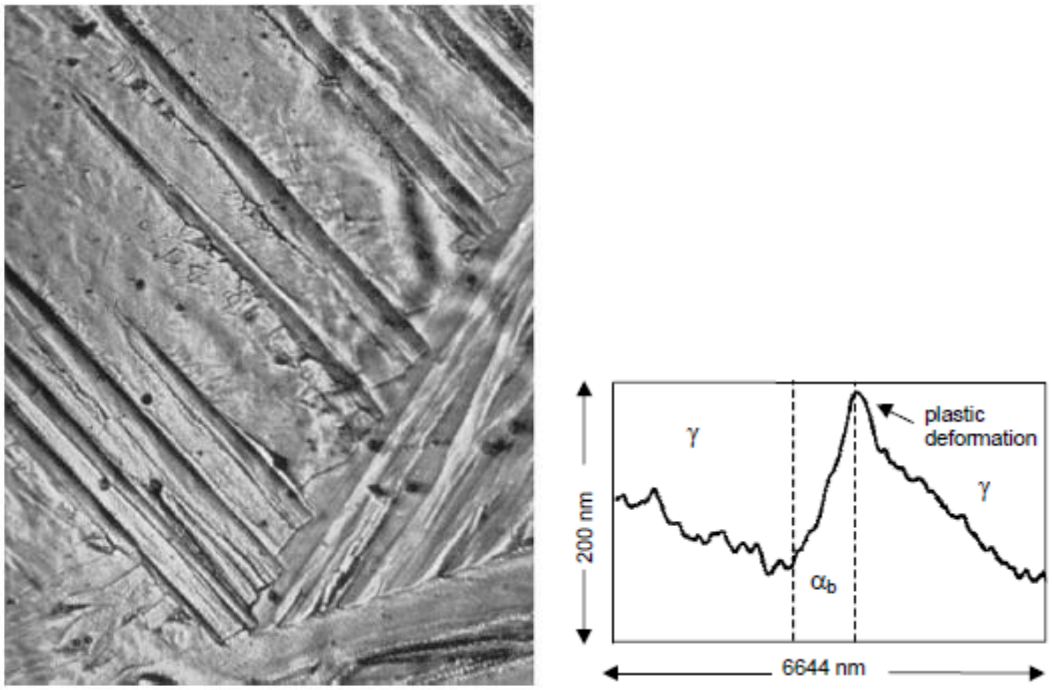

(a) (b)

Figure 2.3.10 (a) Surface relief of bainite for a 0.33C-0.74Mn-3.47Ni (wt%) steel treated at 574℃ for 22hr. Magnification 300x [12]. (b) An atomic force microscope scan across a bainite sub-unit with surface relief [28].

Unlike martensite, bainite forms at higher temperatures where the austenite cannot elastically accommodate the shape deformation and thus in regions adjacent to bainite, it experiences plastic deformation [28]. The plastic deformation restricts the growth of each bainite plate thus each plate grows to a limited size (much smaller than the austenite grain size) before successive nucleation of new plates, giving rise to the sheaf morphology (see Figure 2.3.7).

UNIVERSITEIT VAN PRETORIA
UNIVERSITY OF PRETORIA
YUNIBESITHI YA PRETORIA

The observation by Ko et al [25] and Bhadeshia [33] of surface relief on bainite as with martensite brought about the conclusion that both structures form or nucleate by lattice shear, however, with the bainite growth rate then governed by carbon diffusion. Due to the lower growth rate of bainite relative to martensite, Ko and Cottrell proposed that bainite growth is controlled by carbon diffusion. The surface relief was considered vital evidence in support of the displacive theory and for growth that occurs by migration of a glissile ferrite:austenite interface where the bainite that forms inherits the carbon content of the austenite from which it forms [12].

2.3.3 The Diffusional model

The diffusional or reconstructive model ascribes the nucleation and growth of bainite to a carbon diffusion controlled process [12]. The diffusion controlled transformation of austenite to bainite is said to occur by a diffusional ledge movement mechanism [28, 34]. Diffusional growth of bainite, according to Hultgren [35], occurs under full local equilibrium along the A_{e3} phase boundary by short-range diffusion at ledges in the austenite:ferrite interface. Upper bainite grows by movement of austenite:ferrite interfaces of low coherency and lower bainite by the movement of more coherent interfaces which require little self-diffusion [24]. Within the diffusional model, as with the displacive model, martensite, Widmanstätten ferrite and bainite are a continuous series of transformation products that result from increased carbon trapping as the transformation temperature is reduced [36].

At lower transformation temperatures, substitutional atoms diffuse much slower than interstitial atoms and therefore no diffusion of substitutional elements is observed. Hultgren first found that there was no partitioning of alloying elements between ferrite and carbide during the formation of bainite. It is generally agreed that bainite forms under para-equilibrium conditions whereby only carbon partitions between austenite and ferrite. The upper limiting temperature for bainite forming in the reconstructive model is given by the B_s rather than the T_o temperature. Hillert examined the relationship between the B_s and T_o as a function of carbon concentration and found that their respective slopes differed and that they intersected at some point [35]. Bainite formed at carbon concentrations greater than the upper

UNIVERSITEIT VAN PRETORIA
UNIVERSITY OF PRETORIA
YUNIBESITHI YA PRETORIA

limit x_{To} imposed by the T_o line. In a similar experiment, Agren et al [12] also found that bainite forms at carbon contents greater than given by the T_o curve (see Figure 2.3.13).

2.3.3.1 The Kinetic definition

The B_s is the temperature above which it is not possible for bainite to form. It lies considerably below the eutectoid temperature and is the upper limit to the kinetically determined bainite C-curve [25], [37]. The C-curve identifying bainite is intermediate with respect to the temperature ranges for martensite and polygonal ferrite/pearlite. The C-curve on the CCT represents the nucleation and early stage growth [14].

The addition of alloying elements has a significant effect on the B_s. Several authors [38] have established equations of the B_s temperature as influenced by the addition of alloying elements to a plain carbon steel. According to phase transformation theory, the formation of each phase is reflected by a C-curve in a CCT diagram. However, both upper and lower bainite are contained within the same C-curve of a CCT diagram.

2.3.4 The Stasis

The formation of a maximum amount of ferrite that is significantly less than the amount indicated by the lever rule as applied to the para-equilibrium A_{e3} line or $\gamma/\gamma+\alpha$ phase boundary, is referred to as the incomplete transformation or the transformation stasis [28]. As the B_s is approached, it is found that in some steels the bainite transformation ceases momentarily and at times for lengthy periods before it resumes and achieves the volume fraction predicted by the lever rule. The incompleteness of the bainite transformation is inevitably linked to the mechanism of transformation and is thus accounted for in both displacive and diffusional models.

UNIVERSITEIT VAN PRETORIA
UNIVERSITY OF PRETORIA
YUNIBESITHI YA PRETORIA

2.3.4.1 The Influence of T_o

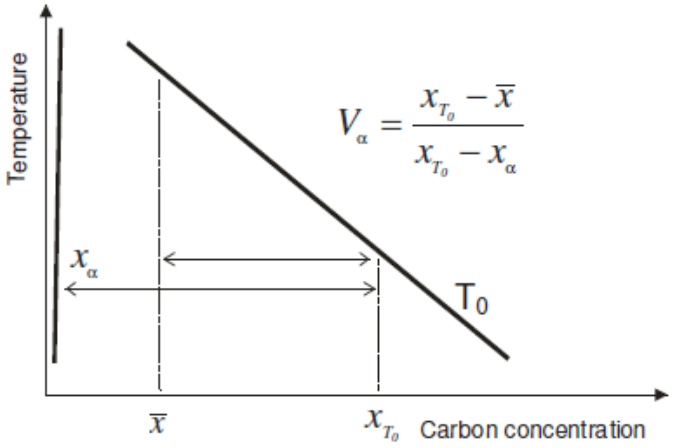

Figure 2.3.11 The lever rule as applied to the T_o line to find the maximum volume fraction of bainite that can form at a specific temperature under diffusionless conditions.

Figure 2.3.11 is an illustration of the lever rule applied to the T_o on a phase diagram. The T_o curve typically lies between the A_{e1} and A_{e3} temperatures, therefore applying the lever rule to the A_{e3} curve where equilibrium conditions are obtained, gives the amount of bainite that ought to form at a specific temperature. The reaction is incomplete in terms of its failure to reach completion with respect to the equilibrium amounts predicted by applying the lever rule to the A_{e3} curve [27].

With reference to the displacive model, the incomplete transformation may be explained by considering the progressive accumulation of carbon from bainitic ferrite. For instance, consider the initial diffusionless formation of a plate of bainite. Due to the low solubility of carbon in ferrite, excess carbon from the newly formed bainitic ferrite plate is rejected into the surrounding austenite. The next plate of bainitic ferrite that grows does so from carbon enriched austenite. The process is repeated during the growth of bainite so that each successive plate grows from a consistently higher carbon enriched austenite such that the process ceases when the carbon concentration in the austenite reaches the T_o curve [18, 35]. Thus the reaction is incomplete as the equilibrium composition as given by the A_{e3} curve is not attained [28]. To illustrate the relation of the incomplete reaction to the T_o curve, carbon concentrations of residual austenite in isothermally transformed steels were plotted on a phase diagram together with the A_{e3}, T_o and T_o' curves, which were determined by

UNIVERSITEIT VAN PRETORIA
UNIVERSITY OF PRETORIA
YUNIBESITHI YA PRETORIA

thermodynamic assessment. The results are given in Figures 2.3.12 and 2.3.13. The authors found that the reaction stopped when the carbon concentration in the residual austenite was closer to the T_o curves than to the A_{e3}.

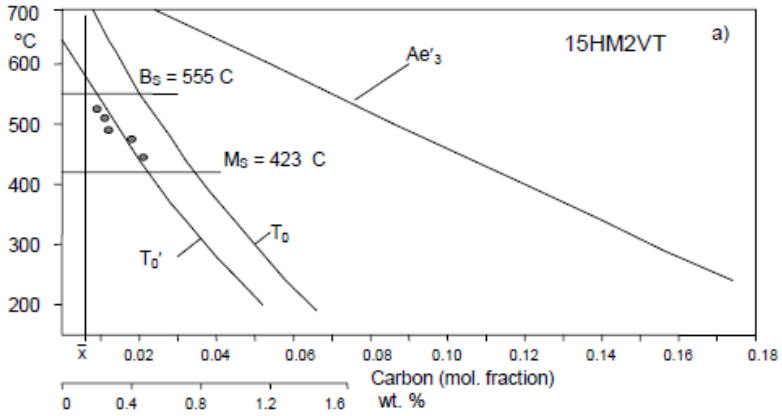

Figure 2.3.12 Phase diagram showing calculated A_{e3}, T_o and T_o' curves and experimental carbon concentration of residual austenite after isothermal bainite formation in a 15H2VT steel [28].

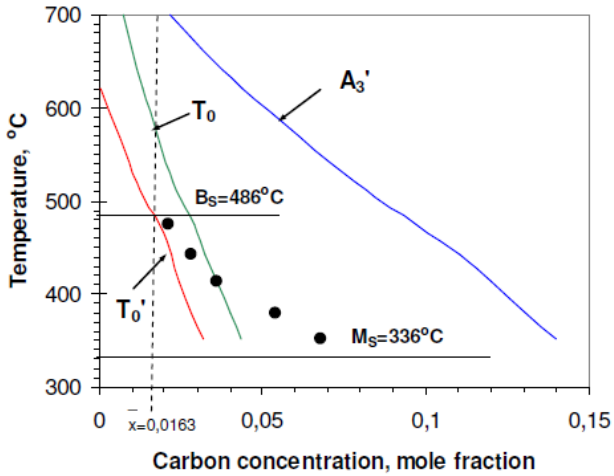

Figure 2.3.13 Phase diagram showing calculated A_{e3}, T_o and T_o' curves and experimental carbon concentration of residual austenite after isothermal bainite formation in an Fe-Cr-Si-C steel [39].

It can be seen from Figures 2.3.12 and 2.3.13 that for a given carbon concentration, a larger undercooling below T_o allows a larger quantity of bainite to form. Likewise, with lower undercoolings at transformation temperatures approaching T_o, smaller amounts of bainite are

UNIVERSITEIT VAN PRETORIA
UNIVERSITY OF PRETORIA
YUNIBESITHI YA PRETORIA

formed [27]. Diffusionless growth of bainite, therefore, requires that the carbon concentration in the austenite is below that given by the T_o curve.

2.3.4.2 The Solute Drag-Like Effect

The framework for a solute drag-like effect is created in the context of a diffusional mechanism of bainite formation, particularly at higher temperatures as in upper bainite. The solute drag-like effect accounts for retarded transformation of austenite to bainite by the involvement of substitutional solute atoms during the transformation. There are various solute drag-like models which illustrate the capacity of involvement of substitutional solute atoms:

Hultgren first observed that there is no partitioning of alloying elements between ferrite and bainitic carbide. This “no partitioning”, in the view of Hillert, could also be explained by a no partitioning local equilibrium (NPLE) [35]. The concept incorporates the participation of alloying elements during the formation of bainite by considering an alloying element accumulation adjacent to the moving interface which Hillert termed a ‘spike’. If the spike is of a thickness below atomic dimensions, it is more likely to move into the moving austenite:ferrite interface and effects of such an alloy element aggregate within the interface would be similar to the solute drag effect originally proposed by Cahn [40].

Another explanation for the incomplete reaction bay in the TTT diagram and for the overall reduced kinetics was established by Aaronson et al [41] whose work on the diffusional reaction of pro-eutectoid ferrite in Fe-C-X alloys (where X is a substitutional alloying element which significantly reduces the activity of carbon in austenite) showed that nonequilibrium absorption of the element X to austenite:ferrite grain boundaries occurs. Since growth occurs under para-equilibrium conditions, accumulation of substitutional solute atoms in the austenite:ferrite boundaries occurs when the moving boundary retains some solute atoms in excess of their average concentration in the alloy [42-44]. In alloys where X is an element that reduces the activity of carbon [41], the carbon concentration gradient in the austenite ahead of the growth front is reduced. Stasis will occur when the reduction in carbon activity at the α:γ grain boundaries leads to a carbon activity which is the same as that further from the boundary such that there is no gradient of the carbon activity in the austenite. The

UNIVERSITEIT VAN PRETORIA
UNIVERSITY OF PRETORIA
YUNIBESITHI YA PRETORIA

diminished carbon concentration gradient, which drives the growth of ferrite, slows the ferrite growth kinetics [45].

One quantitative explanation for the stasis based on the solute drag effect, is that involving ortho- and para-equilibrium austenite/ferrite phase boundaries on an Fe-C-Mo phase diagram [36]. Under para-equlibrium, the fraction transformed is given by:

$$f = (c^2 - c^0)/(c^2 - c^\alpha) \qquad \text{eq 2.5}$$

and under local equilibrium it is given by

$$f = (c^3 - c^0)/(c^3 - c^\alpha) \qquad \text{eq 2.6}$$

where c^0, c^α , c^2 and c^3 are the carbon concentrations in the bulk ferrite, at the para-equilibrium $\gamma/\alpha+\gamma$ and local equilibrium at the $\gamma/\alpha+\gamma$ phase boundaries respectively. Solute drag forces the boundaries to the left in Figure 2.3.14 and smaller transformed fractions are obtained.

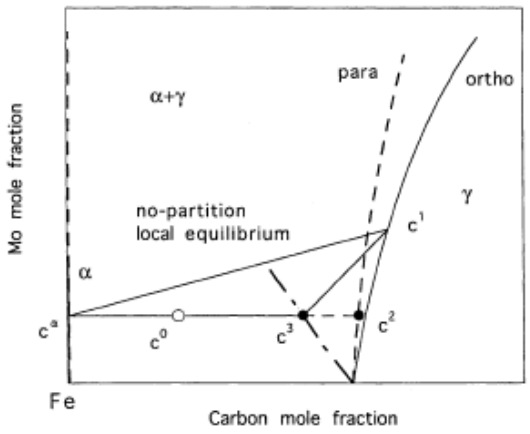

Figure 2.3.14 Isothermal section of a Fe-C-Mo phase diagram where solute drag results in lower volume fractions of ferrite with the lever rule applied to the para-equilibrium (dashed) boundary.[36].

The rate of formation of bainite is limited, though not necessarily controlled by diffusion of carbon, and also by the diffusion of substitutional elements and interfacial reactions. In Fe-C steels, the absence of substitutional alloying elements and thus without their slower diffusion

UNIVERSITEIT VAN PRETORIA
UNIVERSITY OF PRETORIA
YUNIBESITHI YA PRETORIA

rate, allows higher reaction rates. The alloying elements are, therefore, responsible for the slower kinetics in alloy steels [46].

The decomposition of austenite to bainite tends to be more complete as the transformation temperature decreases and the stasis is thus more likely to occur in the upper bainite range [24].

The incomplete transformation in steels, in addition to being temperature dependent, is also dependent on the chemical composition. In some steels where the stasis is not observed, it is as a result of the overlap of the bainite and pearlite C-curves which interfere with the reaction at higher temperatures. Where carbide forming elements capable of separating the C-curves are present, the stasis is more observable. The addition of Mo to steel produces a bay in the TTT diagram as well as the incomplete transformation of austenite to bainite. Figure 2.3.15 below shows sigmoidal curves that vary in the extent to which the formation of bainite is stalled. Curve IV is subdivided into 3 sections with the middle stage having a slope of zero where df/d(log t) = 0. At this point f, which is the volume fraction of austenite transformed, is less than that allowed by the lever rule. As the temperature and compositions are varied from the conditions under which stasis occurs, the curve changes from III to curve II, where a non-zero gradient is found at the middle stage and eventually to curve I where no stasis is observed. In the type I curve, JMAK type kinetics is consistent throughout the transformation. It was found for this steel that the stasis will develop only when specific C-Mo ratios are exceeded [42].

UNIVERSITEIT VAN PRETORIA
UNIVERSITY OF PRETORIA
YUNIBESITHI YA PRETORIA

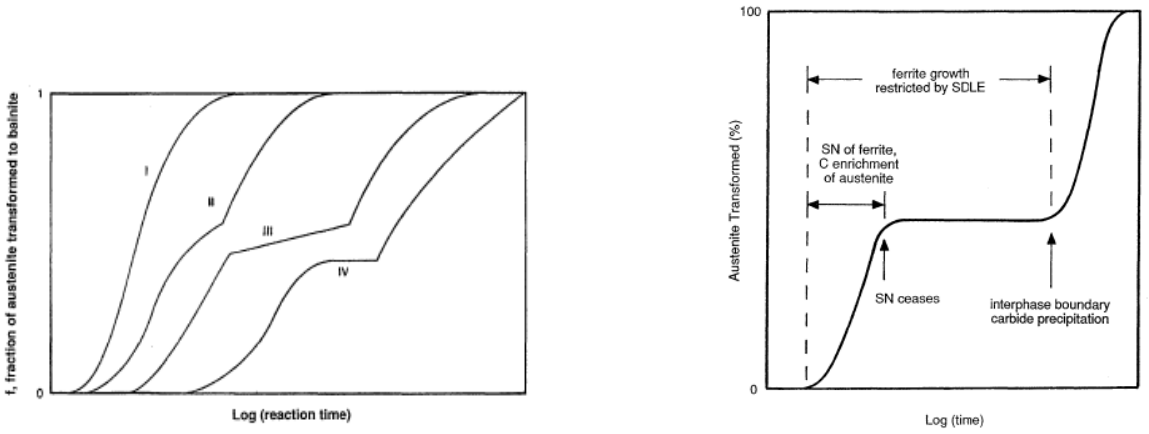

Figure 2.3.15 Schematic illustrations of reaction kinetic behaviour below the B_s and the sequence of transformation [47]. SN = sympathetic nucleation and SDLE = solute drag-like effect.

2.4 Mechanical properties

2.4.1 Ductile and brittle fracture

The fracture of a metal occurs in either a ductile or brittle manner. Ductile fractures are characterised by formation and coalescence of microvoids while brittle fractures occur by cleavage in a transgranular or by intergranular manner.

The shape and orientation of ductile dimples are indicative of the manner of loading experienced during fracture [48]. Homogeneous plastic strain in the loading direction produces equiaxed dimples. A non-uniform force instead produces dimples elongated in the direction of crack extension. Microvoids that initiate the formation of dimples tend to nucleate at regions of local strain discontinuity such as inclusions and grain boundaries.

Brittle fracture is characterised by cleavage fracture. This is a low energy type of fracture that propagates intragranularly along cleavage planes. River patterns or chevron markings are a key feature of brittle crack propagation and can aid in locating the origin of a crack by tracing back the direction of crack propagation. Cleavage occurs on specific, low-index crystallographic planes and it is the mismatch of these planes across grain or subgrain boundaries that produce cleavage steps and ultimately, river patterns. In this way, obstruction

UNIVERSITEIT VAN PRETORIA
UNIVERSITY OF PRETORIA
YUNIBESITHI YA PRETORIA

to advancement of a cleavage crack is created. Misorientation at grain boundaries also causes tearing in the vicinity of the grain boundary together with localized deformation [49].

2.4.2 Effect of precipitates on fracture

In microstructures containing a hard or brittle second phase, embrittlement is likely to occur and often leads to brittle fracture. The type of bainite that forms in a steel affects its fracture resistance. Lower bainite generally shows improved toughness, ductility and strength in comparison to upper bainite [50]. Steels containing upper bainite as a secondary decomposition product are susceptible to brittle fracture. In such instances, the Ductile to Brittle transition temperature is raised and the Upper Shelf Energy is lowered as shown in Figure 2.4.1. The influence of precipitate morphology is thus illustrated schematically for the case of upper and lower bainite.

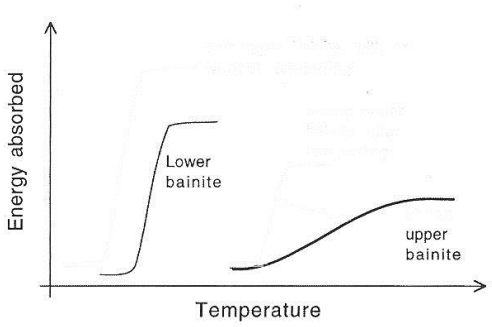

Figure 2.4.1 Schematic illustration of the difference in upper shelf energy of lower and upper bainite.

The simplest mechanism for nucleation of a microcrack as suggested by Stroh [49] and as illustrated in Figure 2.4.2, is the result of a stress concentration produced at the tip of a dislocation pile-up when the material is subjected to stress. In dual phase steels containing precipitates or carbides, the pile up may terminate at a carbide interface. Under such circumstances, the stress generated at the tip of the dislocation pile-up may lead to cracking of the carbide or decohesion at the carbide:matrix interface. This is especially likely if the particle is of a brittle nature. The effect of brittle precipitates is incorporated in the Smith model [51]:

UNIVERSITEIT VAN PRETORIA
UNIVERSITY OF PRETORIA
YUNIBESITHI YA PRETORIA

$$\sigma_f > [\frac{4E_{\gamma f}}{\pi(1-\nu^2)C_o}]^{1/2} \quad \text{eq 2.6}$$

where σ_f is the fracture stress, γ_f is the effective surface energy of the interface between the grain and precipitate, C_o is the thickness of the precipitate, ν is Poisson's ratio and E is Young's Modulus. A dislocation pile-up will cause a grain boundary precipitate to fracture if the stress exceeds a certain value which is in part dependent on the precipitate morphology by the term C_o. From this model, it is evident that coarser precipitates will lower the fracture stress (σ_f). McMahon and Cohen found that the incidence of a microcrack forming increased with increasing thickness of carbides and decreasing test temperature [85].

Brittle grain boundary films not only facilitate crack nucleation, they also reduce energy for crack propagation, thus cracks grow easily [51].

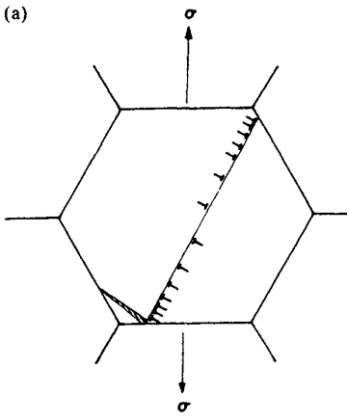

Figure 2.4.2 Microcrack formation by dislocation pile-up.

2.4.3 Effect of a bainitic microstructure on fracture

A bainite packet is defined as a group of parallel laths that subdivide an austenite grain. The packets are separated by high angle boundaries. The packet is further divided into blocks by smaller lath bundles. Laths are separated by small angle boundaries. Consequently, a crack is only slightly deviated at lath boundaries, as shown in Figure 2.4.3, while higher angle boundaries such as exist at extremities of a grain are capable of significantly changing direction of microcrack propagation and even arresting its motion. Boundaries are considered

UNIVERSITEIT VAN PRETORIA
UNIVERSITY OF PRETORIA
YUNIBESITHI YA PRETORIA

to be highly angular in the order of: prior austenite grain boundaries, block and packet boundaries [52].

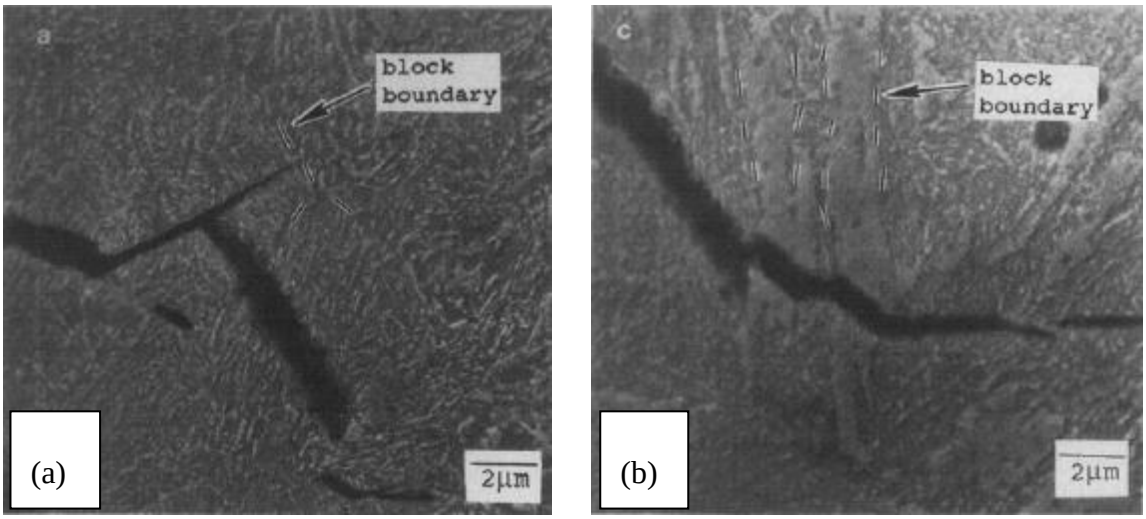

Figure 2.4.3 SEM micrograph of crack deflection at (a) high angle boundaries and (b) low angle boundaries in lower bainitic microstructure of a 4150 steel transformed at 375℃ [53].

It is worth noting, that in upper bainitic structures, the crack passes or proceeds seemingly oblivious of the carbides present and smooth cleavage cracks are found, such as in Figure 2.4.4 below.

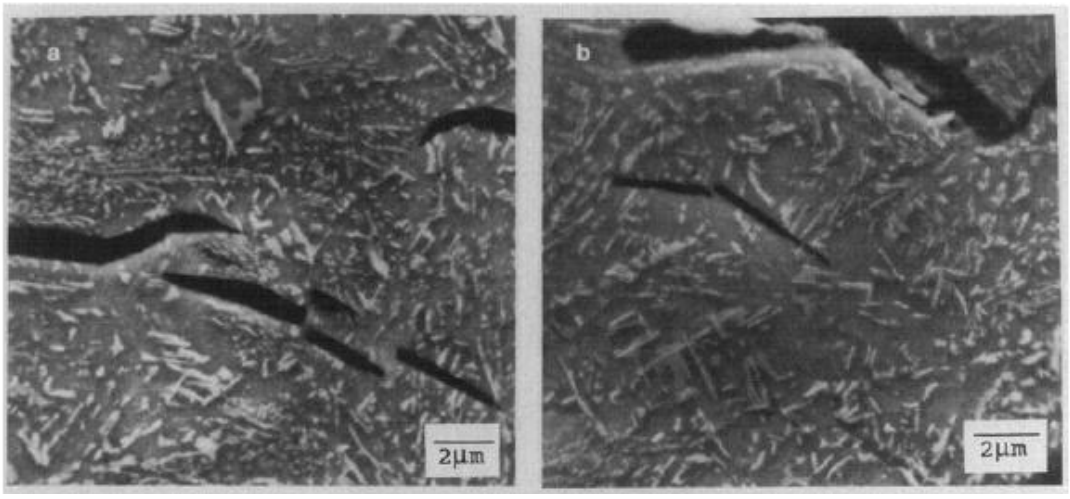

Figure 2.4.4 SEM micrograph of cleavage cracks in upper bainite in a steel transformed at 450℃ [53].

UNIVERSITEIT VAN PRETORIA
UNIVERSITY OF PRETORIA
YUNIBESITHI YA PRETORIA

Zhi-jun et al [52] considered the effect of packet and block boundaries on crack propagation. In body-centred-cubic structured low alloy steel cracks extend along the [100] cleavage planes, as shown by the analysis that was based on the [100] angle between adjacent blocks within a packet. They found that the angle of the [100] planes within the same block was similar to that of adjacent blocks in different packets. Thus having shown the similar effects of blocks and packets on the hindrance of crack propagation, it was concluded that the block is the main substructure controlling toughness rather than the packet. The large angle transition of a crack as it encounters a high angle boundary is the underlying factor behind the linear proportional relationship between high angle boundary length and toughness.

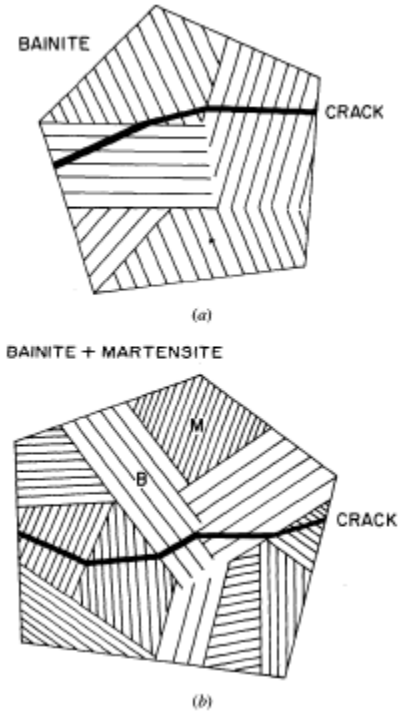

Figure 2.4.5 Cleavage crack deflection in a fragmented austenite grain at (a) bainite packet boundaries and (b) at bainite + martensite packet boundaries.

When subdivision of an austenite grain by martensite and bainite packets occurs, a finer facet size is obtained as shown in Figure 2.4.5 (b). In upper bainitic structures, it is often found that the packet size is smaller than the cleavage facet size due to the deflections at the colony boundaries Figure 2.4.5 (a). As illustrated in Figure 2.4.5 above, deviation of a crack is promoted by fragmentation of a prior austenite grain as illustrated in Figure 2.4.6. Several

UNIVERSITEIT VAN PRETORIA
UNIVERSITY OF PRETORIA
YUNIBESITHI YA PRETORIA

studies show that the aforementioned subdivision tends to have an effect analogous to that of grain size refinement on improved impact toughness [1, 52, 54, 55].

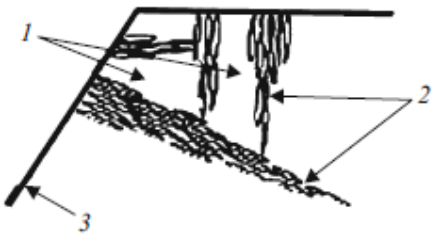

Figure 2.4.6 Diagram showing fragmentation of a prior austenite grain due to formation of bainite sheaves (2) within austenite (1) where growth starts at the austenite grain boundary (3).

2.4.4 Hardness of bainitic microstructures

The main factors responsible for the hardness of bainitic microstructures are the plate thickness and the location of the cementite particles. Lower transformation temperatures lead to harder microstructures. The reason is for this is the decrease in lath width with lower transformation temperatures and the density increase of carbides within the bainitic ferrite plates [18]. Figure 2.4.7 shows the change in hardness as the isothermal transformation temperature increases.

UNIVERSITEIT VAN PRETORIA
UNIVERSITY OF PRETORIA
YUNIBESITHI YA PRETORIA

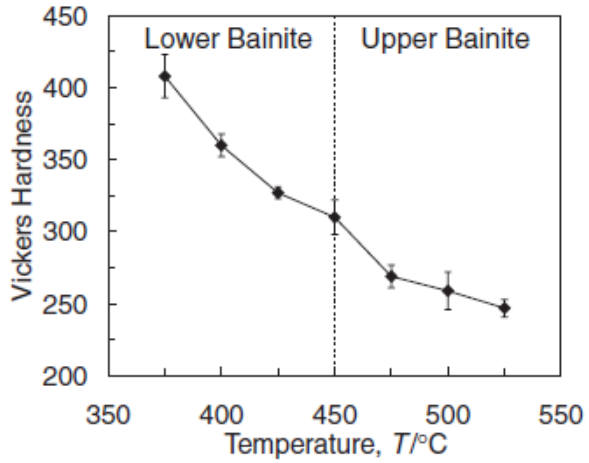

Figure 2.4.7 Hardness decrease with isothermal transformation temperature increase [18].

Plastic relaxation in the austenite at the higher isothermal transformation temperatures generates dislocations which resist the advance of the austenite:ferrite interface. Since the lengthening rate is higher than the thickening rate, the bainitic ferrite plate thickness would thus increase with higher transformation temperatures. The result is that with lower temperature bainite, higher hardness's are attained as the plate width is smaller at these temperatures.

2.4.5 Effect of bainite on toughness

The positive influence of bainite has been associated with the fragmentation of the prior austenite grains as shown in Figure 2.4.5 above. The crack intersects the laths without much deviation and its direction of propagation is altered only as it passes from one packet to another. Retained austenite may hinder the progress of a crack. Fractographic analysis of upper bainite-martensite fracture surfaces in Figure 2.4.8, revealed coarser fractures in a cleavage and detachment mode. Plastic deformation at the tip of a crack formed in upper bainite is minimal and the fracture mechanism becomes cleavage and less plastic deformation ensues. In microstructures consisting of lower bainite:martensite, the existence of cleavage fracture was limited to regions consisting of martensite only.

UNIVERSITEIT VAN PRETORIA
UNIVERSITY OF PRETORIA
YUNIBESITHI YA PRETORIA

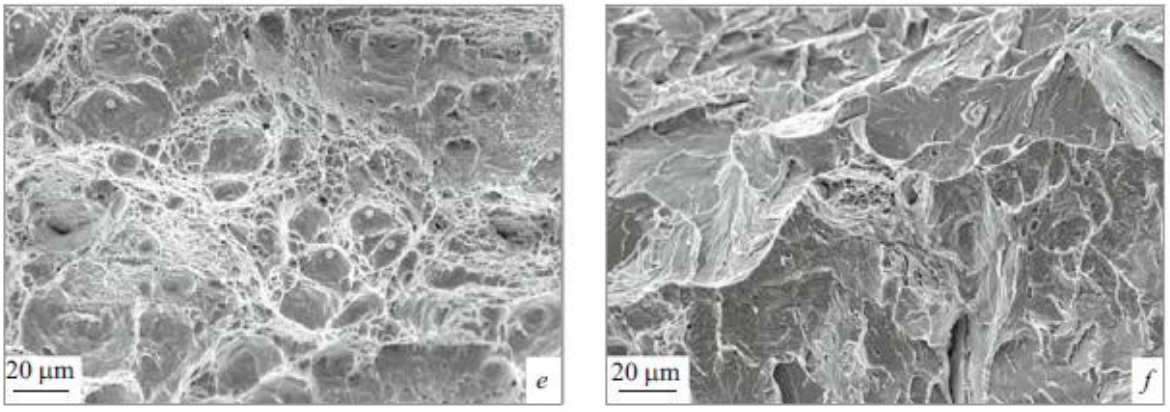

Figure 2.4.8 Fracture surfaces of a 26Kh1MFA steel consisting of (a) martensite and lower bainite and (b) martensite and upper bainite [1].

The decrease in impact toughness for the structure in Figure 2.4.8 (b) is attributed to heterogeneous distribution of carbides of a coarse morphology. In such cases, crack deflection only occurred on intersection with high-angle martensite packet boundaries.

The good impact toughness of lower bainite is due to the high density of high-angle boundaries presented by the morphological packets and blocks that make up its microstructure. A propagating cleavage crack encountering such a block boundary will change its plane of propagation in accordance with the crystallography ahead of the boundary. In order for effective deflection to be attained, the crystallographic misorientation between boundaries ought to be greater than 15°. Ferrite plates aligned at 15° and lower consist of crystallographic packets [56].

The subdivision of a prior austenite grain by laths and packets of martensite and bainite has a significant effect by the crack propagation energy absorption that occurs at the boundaries of these subunits. In one study [2] it was shown that the size of packets and laths was smallest in a mixed bainite-martensite microstructure. The packet size was 28µm and the lath size 2µm. The martensitic microstructure had larger packet and lath sizes of 47 and 4µm respectively and the largest substructure sizes measured were for the bainitic structures of 60µm and 9µm.

Instrumented impact tests, which measure the crack initiation and propagation energies separately, show very low fracture energy for upper bainite structures [57]. A rapid decrease

UNIVERSITEIT VAN PRETORIA
UNIVERSITY OF PRETORIA
YUNIBESITHI YA PRETORIA

of crack propagation energy was found for fracture in upper bainite microstructures in Figures 2.4.9 and 2.4.10. Fracture surfaces observed consisted entirely of cleavage facets.

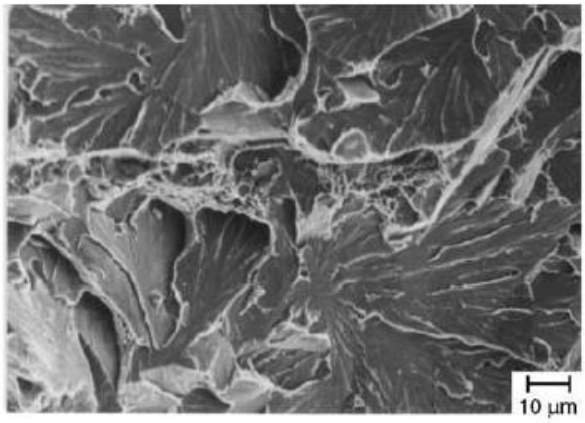

Figure 2.4.9 Cleavage fracture of an AISI 4340 steel isothermally transformed to upper bainite at 430℃ [57].

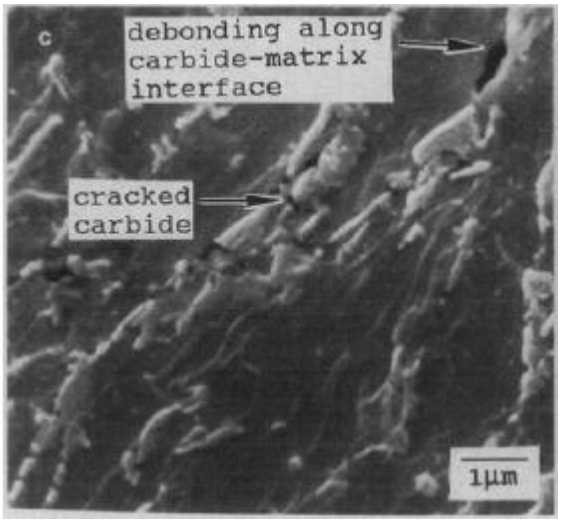

Figure 2.4.10 SEM micrograph of Carbide cracking and debonding in upper bainitic microstructure of a AISI 4150 steel isothermally transformed at 450℃ for 24hrs [53].

Steel alloyed with 2.3wt% Si to produce carbide-free upper bainite and subjected to low temperature tempering at 180℃, showed a fracture surface consisting of an even distribution of fine dimples [58]. These initiation points were considered to have been local regions of high residual stresses produced during the formation of martensite. Tempering at 250℃

UNIVERSITEIT VAN PRETORIA
UNIVERSITY OF PRETORIA
YUNIBESITHI YA PRETORIA

eliminated these initiation points by reducing the micro-stresses in the martensite and large dimples were then found [58].

According to the above authors, structures consisting of 10 - 30% bainite in martensite, formed by isothermal transformation at a temperature above the M_s followed by quenching to martensite, had the same strength as martensite although they showed no improvement of toughness or ductility. An increase of the bainite content to 36% resulted in a quasi-cleavage brittle fracture surface. It was suggested that the micro-ductility decreased due to the higher levels of carbon enrichment of austenite which then produced a harder and more brittle martensite.

When the isothermal treatment temperature was increased from 300℃ to 400℃, the YS/UTS ratio was increased together with a simultaneous decrease in Charpy impact energy. This can be attributed to the finer and more homogeneous distributions of carbides, a higher dislocation density and higher bainitic ferrite aspect ratios found in the lower bainite formed at 300℃ [29].

UNIVERSITEIT VAN PRETORIA
UNIVERSITY OF PRETORIA
YUNIBESITHI YA PRETORIA

3 Chapter 3: Experimental procedures

3.1 Metallography

3.1.1 Secondary Electron Microscopy

Scanning Electron Microscopy (SEM) is a microstructural characterisation technique that utilises the interaction of primary electrons with a sample surface. It is useful in obtaining higher lateral resolution and depth of field images than can be obtained with the conventional optical microscope. Incident electrons that leave the surface of a sample, known as Back Scattered Electrons (BE), are quantified by the backscattering coefficient (η), which is a function of the atomic number. Due to this dependence, BE mode is usually used for identifying compositional contrasts on a sample. Regions of the sample surface with higher atomic number appear brighter than areas of low atomic number. The contrast differences become more visible with lower atomic numbers. BE SEM is thus a means of qualitatively identifying microstructural constituents.

Secondary Electrons (SE) are produced by the interaction of the incident beam electrons with the loosely bound electrons on the sample surface. SE mode is useful for topographic contrast as the secondary electrons to incident electrons ratio (δ) is more sensitive to the tilt angle (i.e. angle between the incident beam and sample surface) than to the atomic number. However, the backscattering coefficient also shows a strong dependence on the tilt angle and BE is thus also used to image surface morphology [59].

Samples mounted in bakelite were prepared for SEM examination by grinding and polishing. Silicon carbide paper of 180, 220, 340, 400, 600 and 800 grit was used to grind samples in this sequence with a continuous flow of water. Samples were then polished to a mirror finish using 3µ and 1µ diamond suspension paste or alumina suspension mixture. The polished samples were then etched in a 2% Nital solution.

UNIVERSITEIT VAN PRETORIA
UNIVERSITY OF PRETORIA
YUNIBESITHI YA PRETORIA

3.1.2 Transmission Electron Microscopy

The Transmission Electron Microscope (TEM) is an instrument used most effectively in high resolution studies of the metallic microstructures. Electrons produced as the source of illumination are transmitted through the sample, which must be thin enough to allow the passage of electrons. Electrons that strike the thin film can either be diffracted by the atomic planes or pass through as transmitted electrons. Interactions of the sample with the electron beam that produce diffracted electrons results in images with internal structural detail of very high resolution of the order of nanometres. The diffracted beams produce dark field images while transmitted electrons produce bright field images.

TEM was used to examine precipitates extracted from samples by the two methods given below in subsections 3.1.3 and 3.1.4.

3.1.3 Carbon extraction replica sample preparation

The procedure for extraction replica sample preparation was as follows:

Mounted samples were etched for approximately 60 seconds using 2% Nital before coating with Au-Pd at an angle small enough to cast a shadow on a surface feature. A coat of carbon was then laid on vertically above the sample surface. The replicas were removed by immersion in 5% Nital for a period of time sufficient to detach the coating from the sample surface. They were floated off in demineralised water and carefully captured on TEM Copper grids. In a final step, the grid was dried on filter paper.

3.1.4 Electrolytic extraction

Samples of dimensions 15x10x10 mm were heat treated to form a completely upper bainite microstructure. The bainitic carbide was extracted from the samples electrolytically as follows:

A 35% HCl was diluted in de-ionised water to obtain a solution of 10% HCl, which was the electrolyte. An insulated copper wire was attached to the sample with conductive epoxy, which was set in a furnace at 100℃. The connection was then mounted in cold curing resin to

UNIVERSITEIT VAN PRETORIA
UNIVERSITY OF PRETORIA
YUNIBESITHI YA PRETORIA

protect it from being corroded. The cathode consisted of a stainless steel electrode. The copper wire connected to the sample formed the anode. The electrode potential of Fe in the reaction Fe^{2+}+ e ↔ Fe is ≈ -0.447V thus a potential of 0.50V was maintained via a potentiostat connected to the circuit. Figure 3.1.1 shows the circuit setup used.

The residue collected was rinsed in ethanol by centrifuging repeatedly to remove the electrolyte. Centrifuging was done at a speed of 18000 rpm for a minimum of 10 times. The rinse was to remove all traces of electrolyte and as Figure 3.1.2 shows, the ethanol turned yellow after the first few rinses. The electrolyte was completely washed off the residue when the ethanol returned colourless after centrifuging.

To examine the extracted precipitates in the TEM, a drop containing residue suspended in solution with ethanol was dispersed on a thin carbon substrate on Cu grids and allowed to dry.

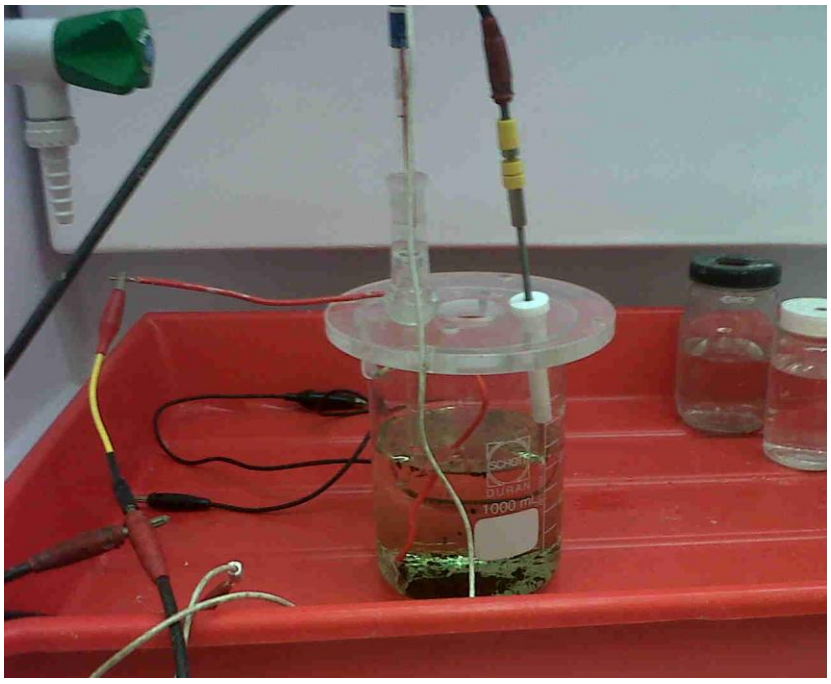

Figure 3.1.1 Circuit used for electrolytic extraction.

UNIVERSITEIT VAN PRETORIA
UNIVERSITY OF PRETORIA
YUNIBESITHI YA PRETORIA

Figure 3.1.2 Tinted ethanol in the beaker after centrifuging and centrifuged sample with extracted precipitate collected at the bottom.

3.1.5 Etchants

Samples mounted for optical microscopic examination were etched by swabbing a 2% Nital solution prepared from Nitric acid (2%) and Ethanol (98%).

A 10% Sodium Metabisulphite colour etchant was used to distinguish between bainite and martensite. The solution consisted of approximately 10g $Na_2S_2O_5$ dissolved in 100ml distilled water. Specimens ground and polished to mirror finish were immersed face up in the etchant followed by gentle agitation till there was visible darkening of the polished surface. The samples were viewed under polarised light to enhance colouration in which bainite is tinted blue and martensite brown [60].

3.2 Thermal analysis

3.2.1 Dilatometry

An induction type dilatometer heats a sample suspended inside an induction-heating coil by passage of a current through the coil. The electrically conductive sample is heated in an induction coil in a vacuum chamber at pressure 0.05Pa. Figure 3.2.1 shows the chamber of the dilatometer used. A reduction in the current flowing through the coil as well as an influx of inert gas (Helium or Nitrogen) controls the cooling. Valves inject blasts of He or Nitrogen gas during quenching at maximum rates of $100Ks^{-1}$ when in deformation mode. Higher

UNIVERSITEIT VAN PRETORIA
UNIVERSITY OF PRETORIA
YUNIBESITHI YA PRETORIA

cooling and heating rates of up to 2500Ks^{-1} and 4000Ks^{-1} respectively are achieved in quench mode, depending on the pressure with which the gas is released.

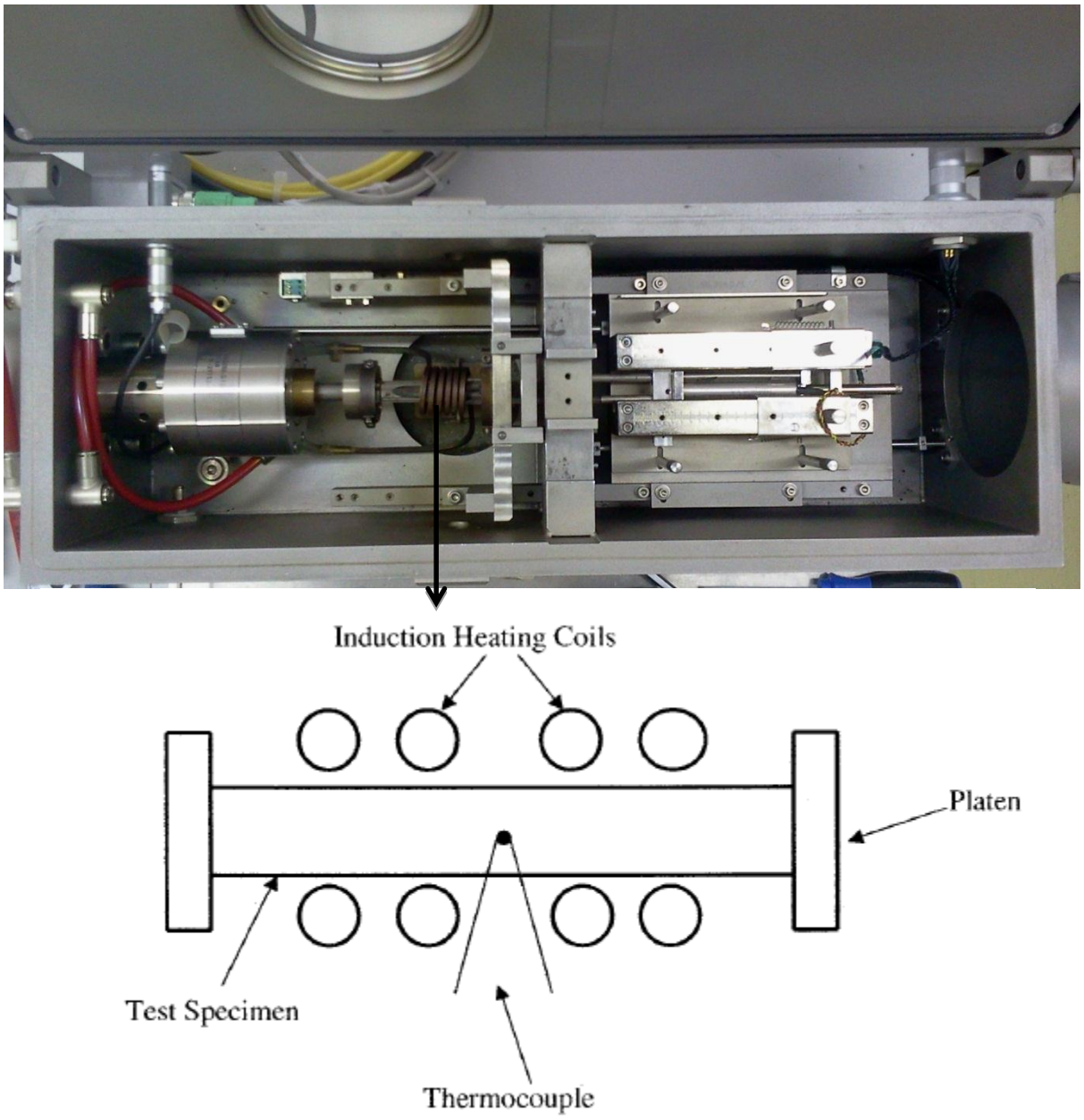

Figure 3.2.1 The chamber of a Bähr DIL 805 dilatometer. The schematic diagram shows the coils surrounding a test specimen.

Temperature changes of the sample are measured by a thermocouple that is spot-welded to the sample. Usually an S-type thermocouple was used.

UNIVERSITEIT VAN PRETORIA
UNIVERSITY OF PRETORIA
YUNIBESITHI YA PRETORIA

The use of a dilatometer is based on the dimensional change that occurs on heating and cooling of steels. The dimensional change occurs as a result of thermal strain or crystallographic change. Thermal strain is a result of temperature change and is usually linear. The change in strain of the sample is measured by push-rod apparatus located at the longitudinal ends of the specimen. During crystallographic phase change, the change in strain is detectable due to the difference in density of the body centred cubic (BCC) and face centred cubic (FCC) unit cells. BCC ferritic structures are stable up to the A_{e3} temperature which for pure iron is A_{c1} = 910℃. Above the upper critical temperature, FCC austenite is stable. On a heating cycle, the non-linear volume change associated with the BCC to FCC transformation is read off a strain-temperature plot. Figure 3.2.2 shows one such plot. A phase transformation is thus distinguishable by the deviation from linear thermal strain. The start and finish of formation of microstructures is read off at the point of deviation from linear thermal strain on the strain-temperature plot obtained upon cooling. Continuous cooling transformation diagrams can be obtained by monitoring the transformation temperatures and times at various cooling rates [61].

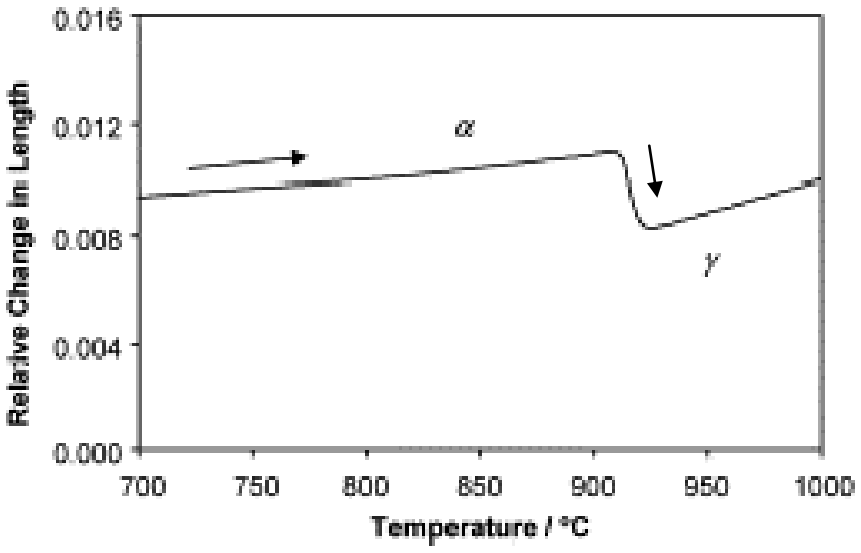

Figure 3.2.2 Diagram showing contraction during transformation of austenite to ferrite.

Solid cylindrical rods of 5mm diameter and 10mm length were machined from the steel plates in the rolling direction. An S-type thermocouple was welded to the surface of the longitudinal centre of the sample. Samples were heated in vacuum to the austenitising

UNIVERSITEIT VAN PRETORIA
UNIVERSITY OF PRETORIA
YUNIBESITHI YA PRETORIA

temperatures of at a rate of 1.5℃/s then soaked for 15minutes. During cooling to room temperature at various rates from the soaking temperature, critical points for the Partial CCT diagrams were determined. A Bähr DIL805 dilatometer was used for the thermal heat treatments. To avoid thermal cycling effects, no sample was reused.

Heat treatments were designed to produce partial CCT diagrams by varying the linear cooling rates as shown in the schematic figure below. The A_{c1} and A_{c3} temperatures were obtained by using low equilibrium cooling rates of 0.03℃/s.

Heat treatments to obtain microstructures consisting of bainite and martensite were obtained by isothermally holding the samples for various times. The schematic figure below shows the temperature cycle used;

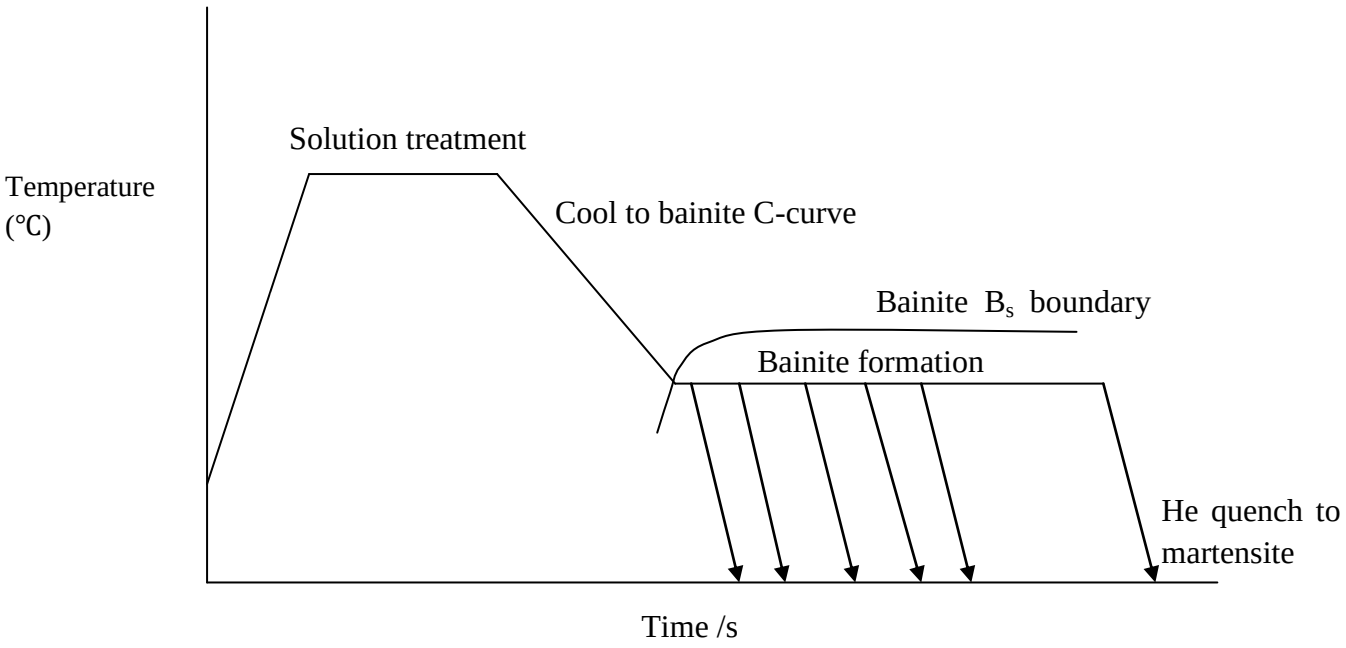

Figure 3.5 Schematic diagram of isothermal heat treatments.

The cooling rates to the bainite C-curve were designed to exclude incubation time from the holding time at the isothermal transformation temperatures. i.e. after cooling the isothermal treatment entered the bainite nose immediately.

UNIVERSITEIT VAN PRETORIA
UNIVERSITY OF PRETORIA
YUNIBESITHI YA PRETORIA

3.2.2 Gleeble

The temperature cycles of Figure 3.5 were simulated on a Gleeble 1500D™ thermomechanical simulator in which full size Charpy samples were heat treated to produce various proportions of bainite and martensite. The method was preferable to salt bath heat treatment as specific rates of heating and cooling could not be maintained in the latter and difficulty was encountered in controlling the microstructures produced in the specimens. However, in the Gleeble it is possible that a temperature gradient occurs between the surface and centre of a sample. This is due to direct electrical heating of the sample where the current concentrates more on the surface of the sample.

Standard Charpy samples of dimension 10x10x55 mm machined in the rolling direction of the low alloy steel plates were used. A K-type thermocouple welded to the centre of the sample controlled the temperature during heat treatment. Samples were notched after heat treatment. A total of 21 Charpy samples per steel were heat treated with three samples assigned to any given heat treatment.

3.3 Mechanical testing

3.3.1 Hardness

A quick and simple way of differentiating between phases is by the micro-hardness of a phase. This is useful for instance, when combinations of phases are obtained in samples continuously cooled from the austenitising temperature. A Micro-Vickers hardness tester was used for measuring the hardness of finer features and a Macro-Vickers hardness testing unit was used to measure the hardness profiles of the steel plates. A dwell time of 10s was used throughout all the tests and five readings were taken for every data point.

3.3.2 Instrumented Charpy impact

The impact toughness of dual phase bainite-martensite Charpy samples was measured by impact tests conducted with an instrumented Instron Dynatup 9210 impact tester. Figure 3.6 shows the drop tower of the instrumented impact tester that was used. To ensure sufficient thrust to fracture the steel samples, a mass of 19.54kg was suspended at a height of 1.65m

UNIVERSITEIT VAN PRETORIA
UNIVERSITY OF PRETORIA
YUNIBESITHI YA PRETORIA

above the position of the Charpy sample. The velocity of the tup was ≈ 3.9m/s, in accordance with standardised procedures which requires velocity in the range of 3 – 6m/s. The tests were conducted at ambient temperature. The sensor situated in the tup unit relays the information to a data acquisition system which records the variation of the force with time/displacements and integrates this information to energy-displacement numerical data on an Excel spread sheet.

Instrumented impact testing gives detailed information about the fracture history of a specimen. The total energy absorbed during the fracture of a Charpy specimen is distributed between elastic and plastic deformation as well as ductile and brittle propagation. Thus the sequence of events leading to failure of a sample can be analysed both visually and with load-displacement or load-time data.

UNIVERSITEIT VAN PRETORIA
UNIVERSITY OF PRETORIA
YUNIBESITHI YA PRETORIA

Figure 3.6 Drop tower of the instrumented impact tester utilised, Instron Dynatup 9210.

UNIVERSITEIT VAN PRETORIA
UNIVERSITY OF PRETORIA
YUNIBESITHI YA PRETORIA

4 Chapter 4: Results

4.1 Microstructures of as the received material

The chemical compositions of the steels used are given in Table 4.1. The steels are commercial grade low alloy plate steels taken from normal production by ArcelorMittal South Africa (Vanderbijlpark plant) in which they are hot rolled and quench and tempered.

Table 4.1 Chemical compositions of the steel plates in wt%.

	C	Mn	Si	Ni	Cr	Mo	Ti	Al	N	B
HC6	0.112	1.351	0.465	0.037	0.291	0.014	0.023	0.032	0.01	0.00243
HC7-03	0.171	1.076	0.295	0.024	0.728	0.226	0.002	0.098	0.01	0.0035
HC7-05	0.17	1.10	0.31	0.04	0.10	0.54	0.005	0.07	0.01	0.002

The HC7-05 steel will be referred to as the HMoLCr steel and the HC7-03 as the HCrLMo steel due to the relative Cr to Mo ratios in these two steels. The HC6 steel will be referred to as the C-Mn steel. The HCrLMo and C-Mn steel plates of thicknesses 41 and 32 mm respectively were first examined in the as-received condition which reportedly had undergone a quench and tempering treatment for the former low alloy steel and as-quenched for the latter C-Mn steel. Microstructural analyses were carried out on the HCrLMo and C-Mn steels by means of optical microscopy, scanning electron microscopy (SEM) and transmission electron microscopy (TEM). The micrographs were taken along the centre thickness of the plates. Note that the HMoLCr steel samples were received at a later stage of the study and therefore the initial analysis up till section 4.3 was conducted on the HCrLMo and C-Mn steels.

UNIVERSITEIT VAN PRETORIA
UNIVERSITY OF PRETORIA
YUNIBESITHI YA PRETORIA

4.1.1 The microstructure of the HCrLMo steel

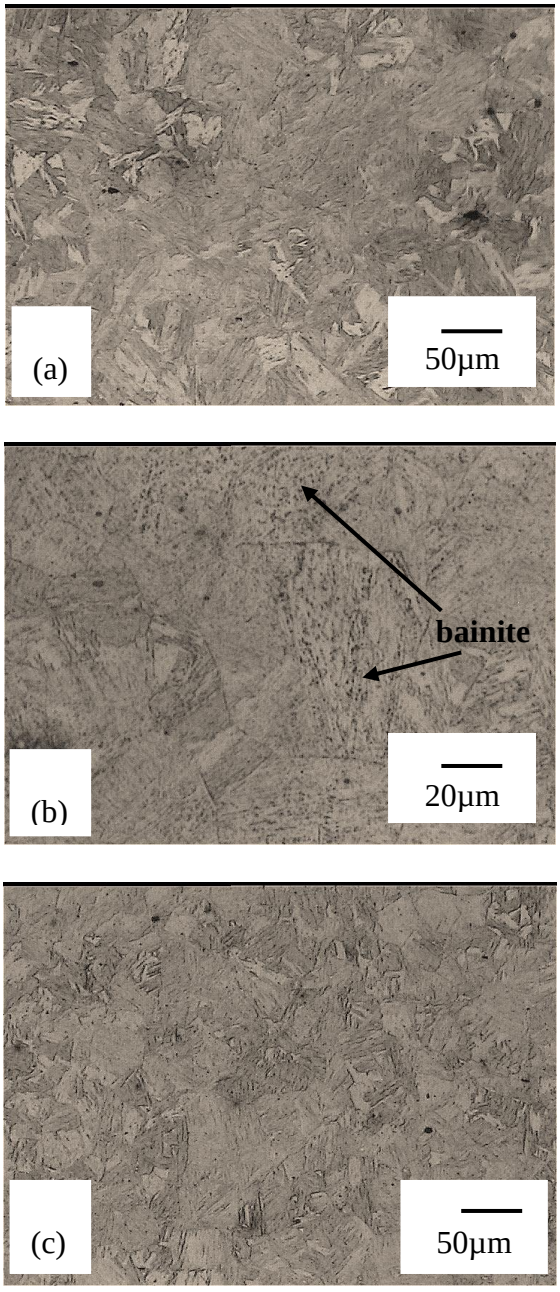

Figure 4.1.1 Optical images of the HCrLMo steel: 0.17C-1.076Mn-0.73Cr-0.23Mo-0.002B steel taken through the mid-thickness at (a) near the top surface (b) in the centre and (c) near the bottom surface.

The optical micrographs show the presence of martensite at the upper and lower surfaces (Figure 4.1.1 (a) and (c)) of the plate and some bainite at the centre (Figure 4.1.1(b)).

UNIVERSITEIT VAN PRETORIA
UNIVERSITY OF PRETORIA
YUNIBESITHI YA PRETORIA

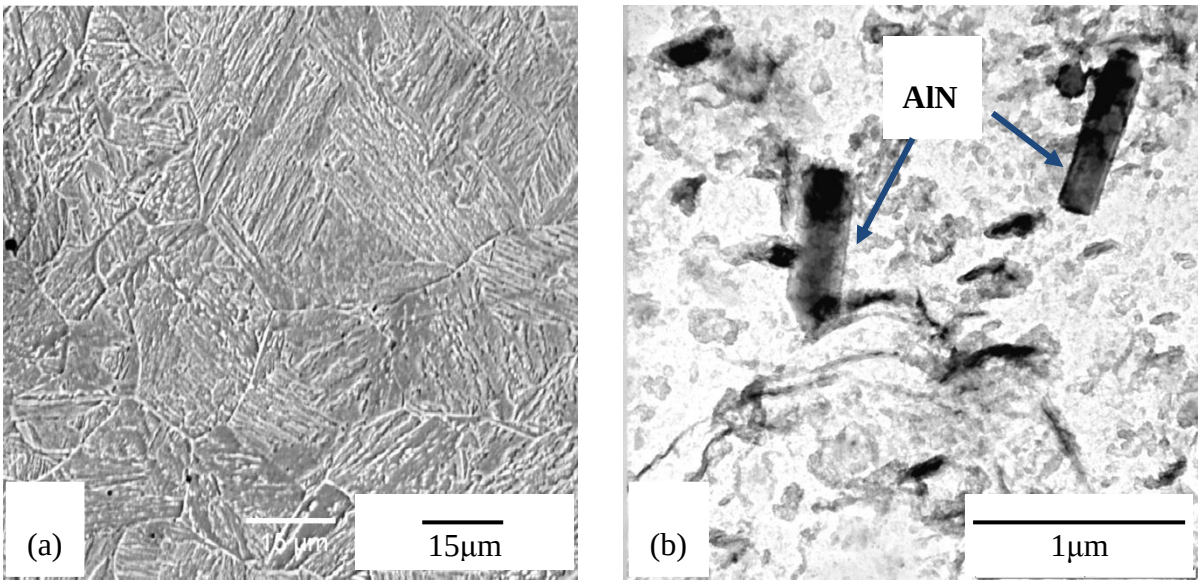

Figure 4.1.2 (a) SEM micrograph of the HCrLMo steel and (b) TEM micrograph of a carbon extraction replica taken from the HCrLMo steel.

The SEM micrograph in Figure 4.1.2 (a) shows grains of lath martensite. The large precipitates in the TEM micrograph in Figure 4.1.2 (b) are AlN particles. The smaller particles that seem to have formed with a specific crystallographic orientation are most likely to be the iron carbides formed in lower bainite.

4.1.2 The microstructure of the C-Mn steel

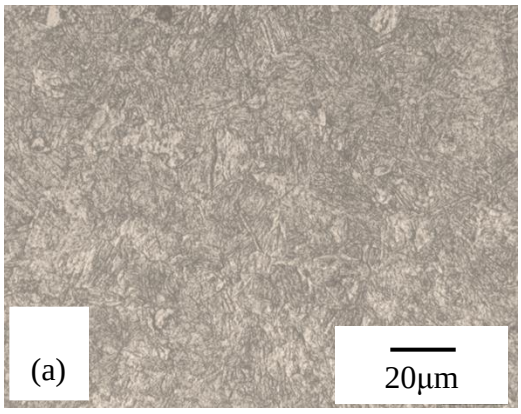

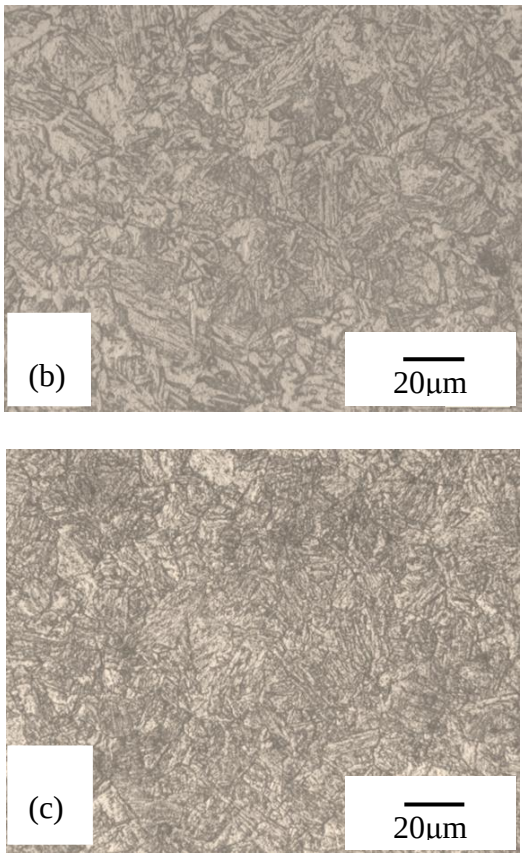

Figure 4.1.3 Optical micrographs of the C-Mn steel taken through the mid-thickness (a) near the top surface (b) in the centre and (c) near the bottom surface of the steel plate.

The optical micrographs taken near the top and bottom surfaces of the C-Mn steel plate showed a martensitic structure. The wider ferrite laths in the microstructure at the centre of the plate shown in the micrograph of Figure 4.1.3 (b) suggest that the structure may be bainite. The SEM micrograph of this lath structure in the centre of the plate is shown in Figure 4.1.3 (a).

UNIVERSITEIT VAN PRETORIA
UNIVERSITY OF PRETORIA
YUNIBESITHI YA PRETORIA

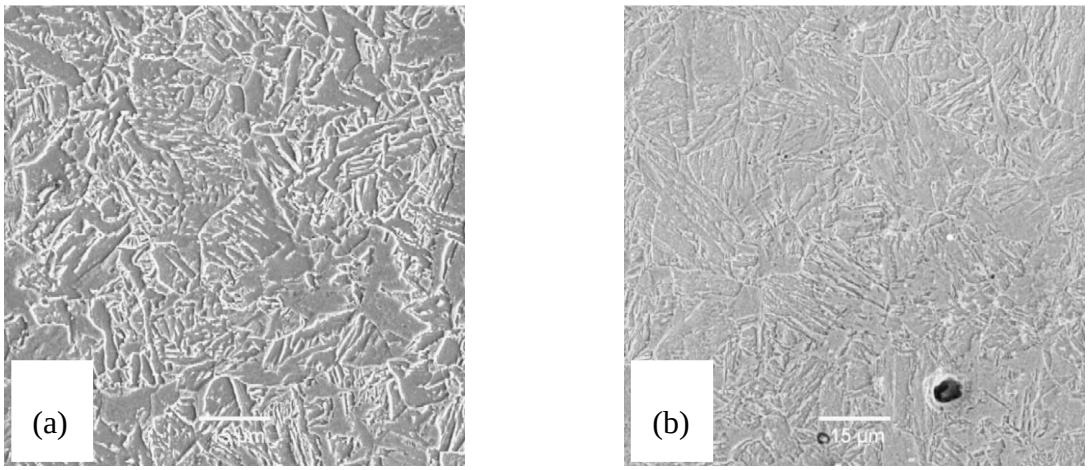

Figure 4.1.4 SEM micrographs of the C-Mn steel taken (a) in the centre and (b) near the surface of the plate.

The higher resolution SEM images of the C-Mn plate confirmed the morphology of the different microstructures that were present at the surface and centre of the plate. According to Béranger et al. [62], in steels with carbon levels less than 0.2wt% the volume fraction of cementite decreases and the shapes of the ferrite laths and lath bundles become more irregular and less distinct. Further evidence of the possibility that the microstructure at the centre of the plate is bainite was found in the carbon extraction replica in Figure 4.1.5 (b). The lath in the microstructure has a fine distribution of small carbides which are at a fixed orientation, as is typical of lower bainite.

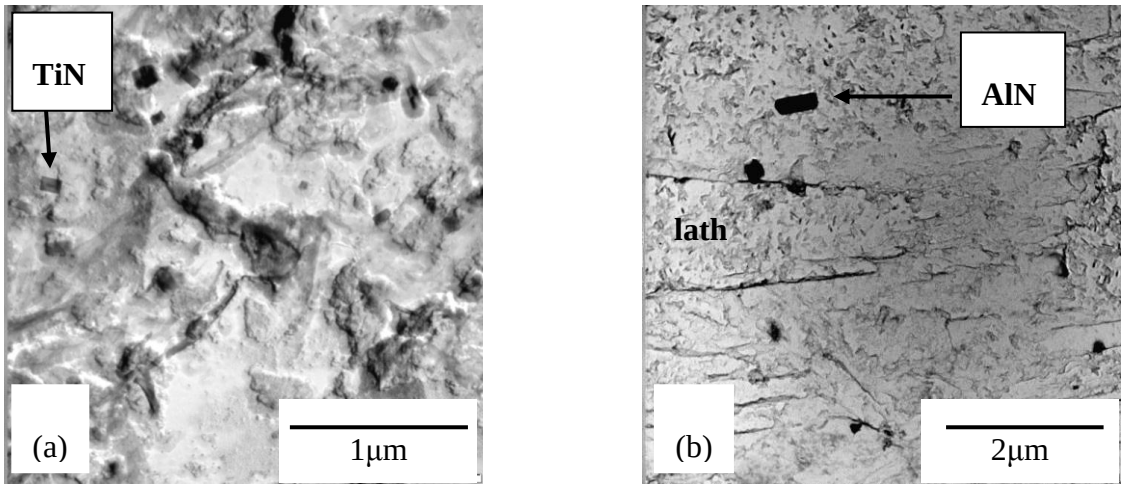

Figure 4.1.5 TEM micrographs of carbon extraction replicas taken from the C-Mn steel (a) shadowed with Au-Pd and (b) unshadowed replica. Note the lath with carbides of size less than 1µm.

Many of the precipitates in the carbon extraction replicas were either TiN or AlN as determined by EDS analysis.

4.2 Hardness Profiles

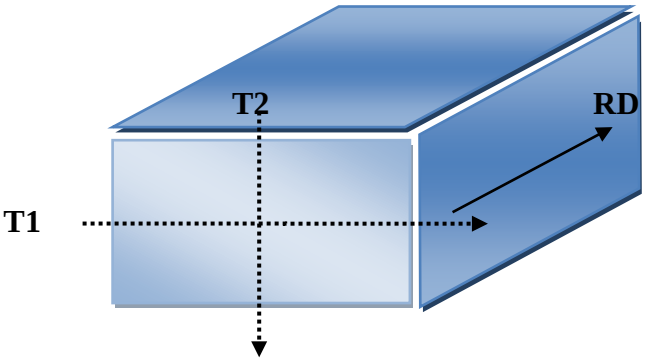

Figure 4.2.1 Schematic illustration of lines along which hardness measurements were taken on the C-Mn and HCrLMo steel plates. RD is the rolling direction. T1 is a path along the centre of the width of the plate and T2 is a path along the centre of the thickness of the plate.

Macro Vickers hardness measurements were determined directly on the surfaces of the as-received steel plates, which were ground to a smooth finish. The hardness indentations were made along paths T1 (width profile) and T2 (thickness profile) on a plane transverse to the rolling direction on the received samples. The test load used was 10kg.

UNIVERSITEIT VAN PRETORIA
UNIVERSITY OF PRETORIA
YUNIBESITHI YA PRETORIA

4.2.1 Hardness profiles of the HCrLMo steel plate near the surface

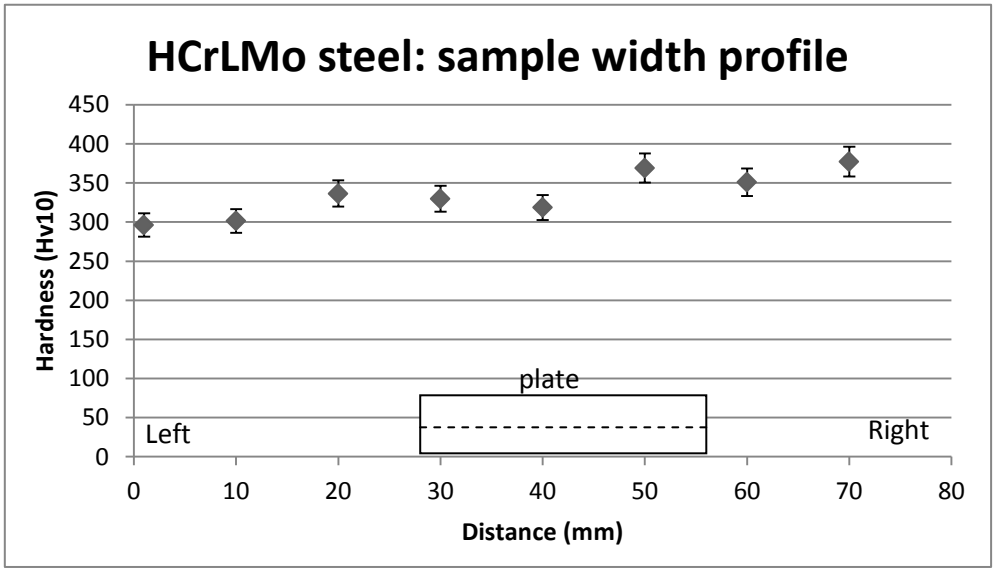

(a)

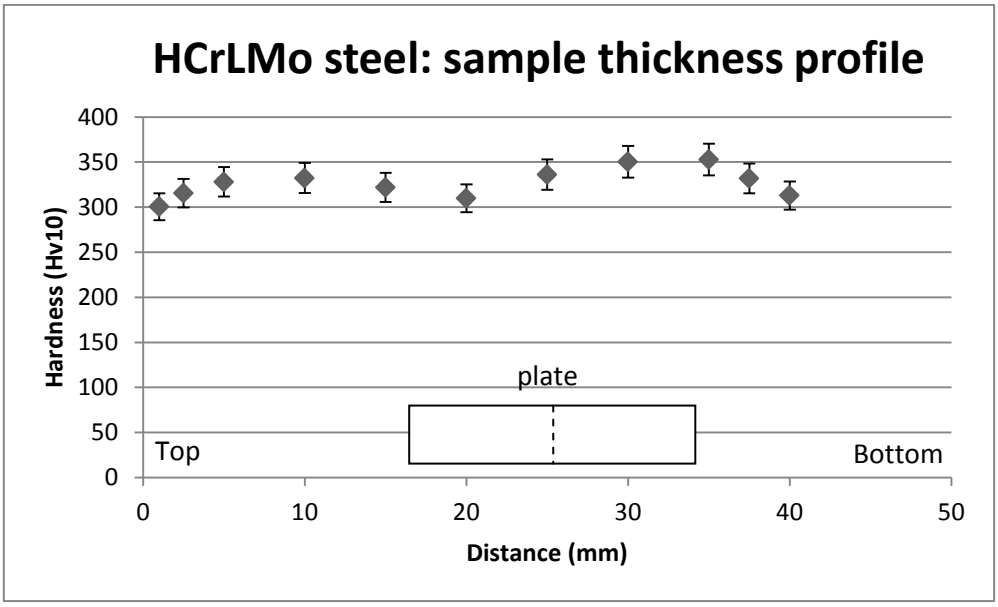

(b)

Figure 4.2.2 (a) Hardness profiles as measured along the centre thickness through the sample width and (b) measured along the centre width of the HCrLMo steel plate. Macro Vickers load: 10kg

Figure 4.2.2 (b) shows the hardness profile across the thickness of the HCrLMo steel plate. The lowest hardness is at the top and bottom edges of the plate and at the centre. It rises at

UNIVERSITEIT VAN PRETORIA
UNIVERSITY OF PRETORIA
YUNIBESITHI YA PRETORIA

about a quarter and three quarter way through the thickness by 31.8HV from the top surface of the plate and by 40HV from the bottom surface of the plate. The centre hardness was 309.9HV, which agreed at the point where the two measurement paths crossed.

The width profile in Figure 4.2.2 (a) increased linearly from the left surface to the right surface of the plate. Note that the edge's hardness's were taken as close to the periphery as was possible, i.e. ~ 2.5 mm from the edge without distortion of the indentation. The width referred to above is that of the received samples rather than the actual plate width produced by ArcelorMittal, which is much larger.

The dip in hardness at the plate centre can be correlated with the micrographs of Figure 4.1.1 (b) which present martensite together with bainite at this position. Bainite is softer than martensite and thus the plate's hardness is lower where some bainite is found. The micrographs of samples taken close to the top and bottom surfaces of the plate in Figure 4.2.2 (a) and (c) contained martensite and thus had a higher hardness. The presence of bainite in the steel plate resulted in a non-uniform microstructure which formed during cooling as a result of slower heat transfer from the steel plate during quenching. The steel plate during production is quenched in a quench brake press by sprays of water on both the top and bottom surfaces, it thus experiences the highest heat transfer at regions close to these surfaces. Slower heat transfer occurs towards the centre and consequently the slower cooling rate results in formation of bainite rather than martensite. The areas at half thickness (see Figure 4.2.2 (a)) are equidistant from the quenched surface and are therefore assumed to experience the same rate of heat transfer, hence no significant variation in width hardness profile was found.

UNIVERSITEIT VAN PRETORIA
UNIVERSITY OF PRETORIA
YUNIBESITHI YA PRETORIA

4.2.2 Hardness profiles of the C-Mn steel

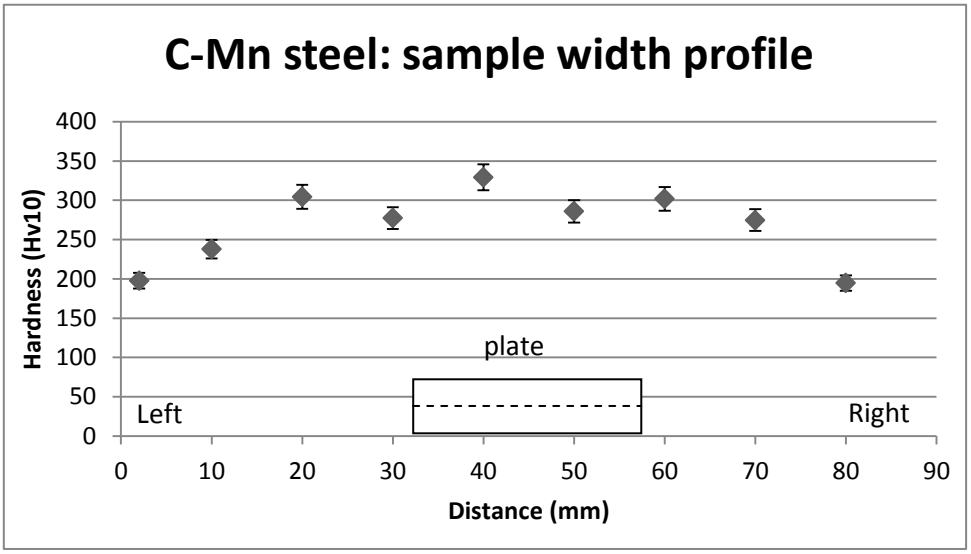

(a)

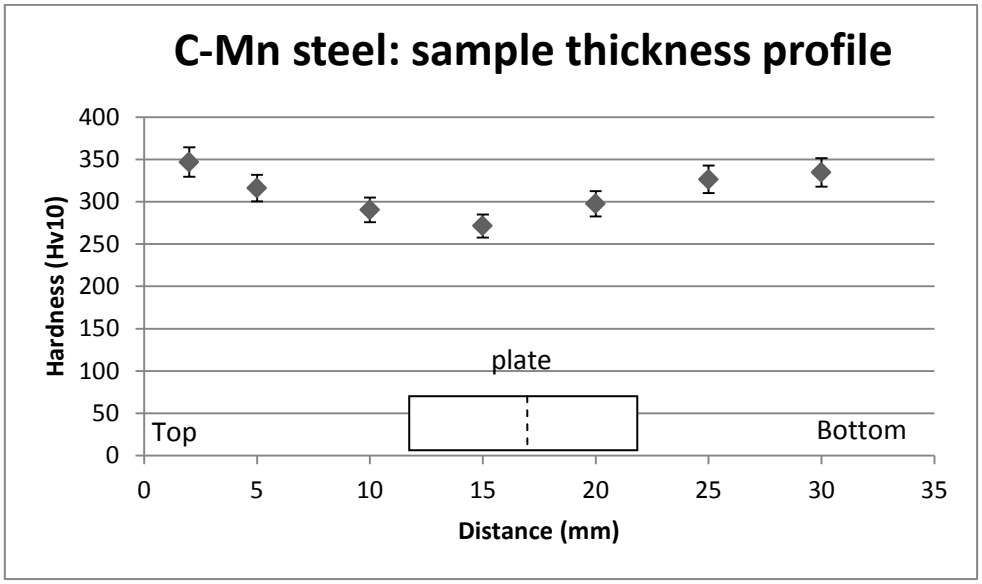

(b)

Figure 4.2.3 (a) Hardness profiles measured along the centre thickness and (b) along the centre width of the C-Mn steel plate. Macro Vickers load: 10kg

The hardness profile in Figure 4.2.3 (b) showed a decrease in hardness towards the centre. The hardness dropped by 75.5HV from the top surface and by 63.4HV from the bottom surface of the plate to a hardness of 271.3HV at the centre. On the contrary, the width

UNIVERSITEIT VAN PRETORIA
UNIVERSITY OF PRETORIA
YUNIBESITHI YA PRETORIA

hardness profile in Figure 4.2.3 (a) had the lowest hardness at the edges and peaked towards the centre with hardness in the region of 277 - 286HV.

As was described in section 4.2.1 for the HCrLMo steel, during quenching the gradient in cooling rate from the plate's surface to centre leads to the formation of different phases which results in a variation of hardness. Since the quench is only directed at the wide top and bottom surfaces and not at the two side edges, the thickness face experiences the least heat transfer and the width hardness profile in Figure 4.2.3 (a) testifies to this. The lowest hardness is found at the width extremities.

The C-Mn steel plate was received in the as-quenched condition and was untempered. By correlating the hardness measurements taken on the C-Mn steel plate with the amount of martensite corresponding to specific carbon contents [63] the amount of martensite contained in the plate can thus be estimated. The hardness data comparison shows that the centre of the plate most likely contains less than 50% martensite while the edges have 95 - 99% martensite.

Hardenability calculations were done for both the HCrLMo and C-Mn steels using a quench factor H = 1 and ASTM 7 grain size and alloying element multiplying factors D_X were obtained from standard tables ASTM A255-02 [63]. From this the Grossmann equivalent thickness for the C-Mn steel plate was found to be 45mm and that of the HCrLMo was 92.5mm. The actual plate thicknesses were 32mm and 41mm and complete hardening was therefore expected. However, the hardness profiles above show that the hardenability was compromised, most likely through inadequate quenching.

4.3 Tempering Characteristics

The tempering curves were plotted from an average of at least five Vickers hardness measurements. The macro-Vickers hardness tests were made on tempered samples using a test load of 10kg. Samples from the HCrLMo and C-Mn steel were austenitised at 900℃ and then quenched in water. Tempering was done in increments of 100℃ from a temperature of 100℃ to 600℃. After tempering, the samples were air cooled and the tempering curves were plotted as Vickers hardness against tempering temperature and are presented in Figures 4.3.1 and 4.3.2.

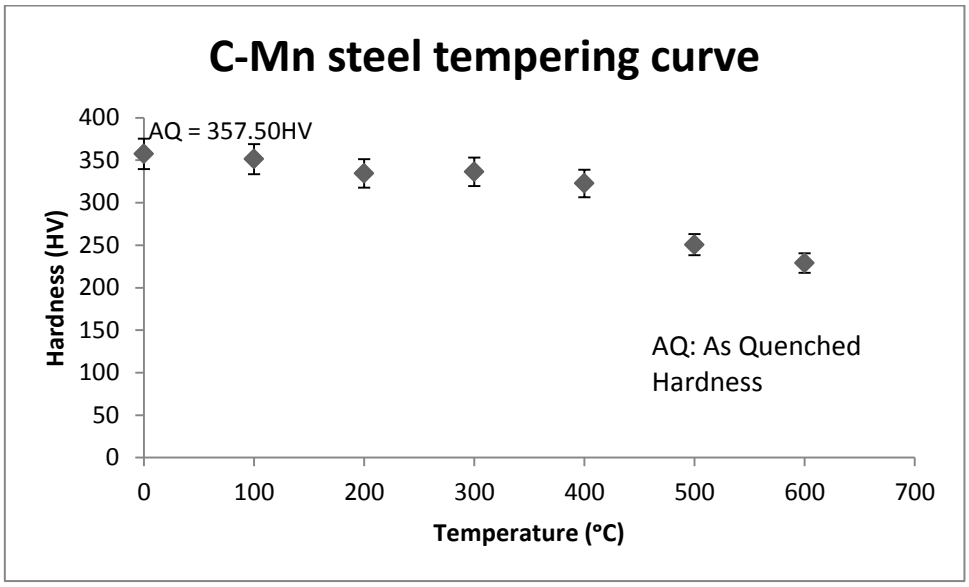

(a)

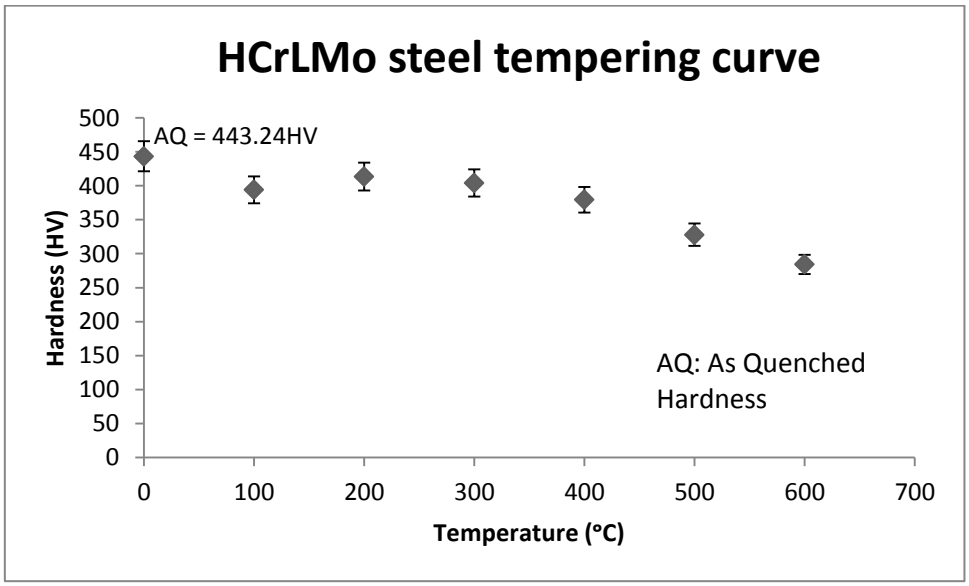

(b)

Figure 4.3.1 Tempering curves for (a) the C-Mn steel and (b) the HCrLMo steel. The samples were tempered for 30mins at temperature after soaking at 900℃ and water quenching. Macro Vickers hardness load: 10 kg with 5 readings per data point.

The C-Mn steel tempering curve in Figure 4.3.1 (a) showed a continual decrease in hardness as the tempering temperature was increased from 100℃ to 600℃. The first tempering

UNIVERSITEIT VAN PRETORIA
UNIVERSITY OF PRETORIA
YUNIBESITHI YA PRETORIA

treatment at 100℃ produced only a slight reduction in hardness while the largest hardness decrease (72.1HV) was found after tempering at 500℃.

The highest hardness for both steels was in the as-quenched state. For the HCrLMo steel, a hardness reduction of 49HV from the as-quenched hardness (443HV) occurred on tempering at 100℃. Thereafter an increase in hardness by 19.4HV was found on tempering at 200℃. This resulted in a slight peak in the tempering curve of Figure 4.3.1 (b). The results are discussed in section 5.1.

4.4 Continuous Cooling Transformation Diagrams

4.4.1 Preliminary tests

4.4.1.1 Determination of Austenitising Temperatures.

In order to establish the temperature at which homogeneous austenite is formed, dilatometric samples machined from the C-Mn and HCrLMo steels were heated to 1100℃ and 1200℃ respectively in a Bähr dilatometer. The high temperatures were used so that the specimen completely transforms to austenite and the linear region above the A_{c3} temperature in which the samples have completely transformed to austenite, could be identified. Figures 4.4.1 and 4.4.2 show the strain – temperature graphs obtained for the C-Mn and HCrLMo steels respectively.

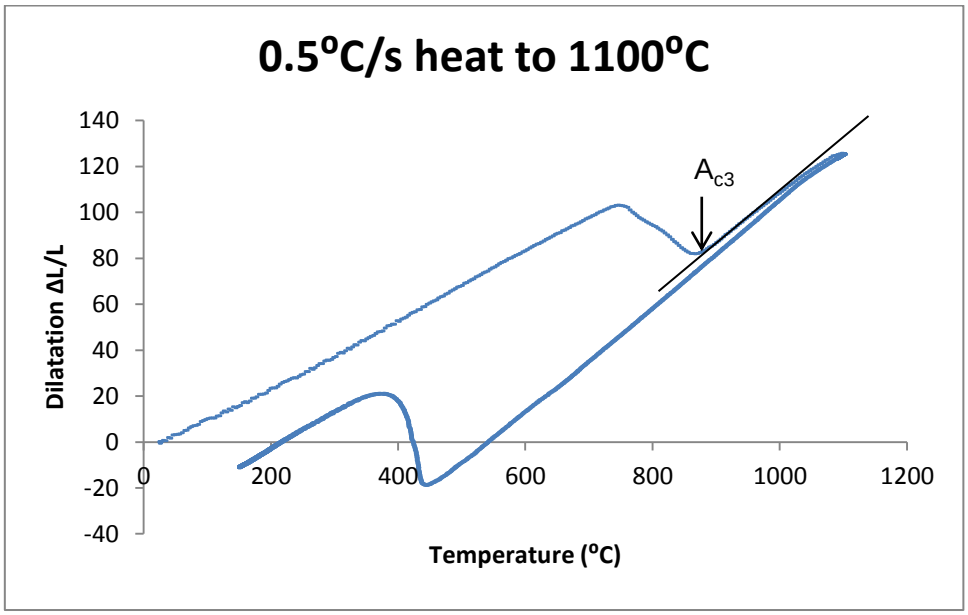

Figure 4.4.1 Dilatometric signal obtained for the C-Mn steel sample which was heated at 0.5℃/s to 1100 ℃ before slow cooling. The critical temperatures found were A_{c1} = 722.3℃ and A_{c3} = 865.3℃.

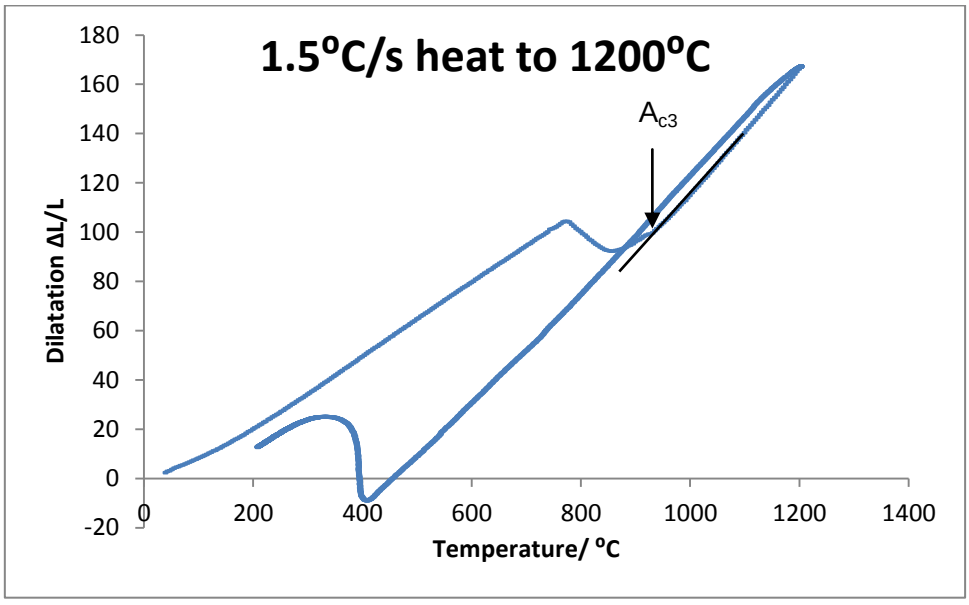

Figure 4.4.2 Dilatometric signal for the HCrLMo steel sample heated at 1.5℃/s to 1200℃ before slow cooling. Homogeneous austenite was obtained at 931.9°C, where the expansion became linear.

The experimental A_{c3} temperature obtained for the C-Mn steel was 865.3℃ and that for the HCrLMo was 931.9℃.

UNIVERSITEIT VAN PRETORIA
UNIVERSITY OF PRETORIA
YUNIBESITHI YA PRETORIA

In addition to the experimentally obtained temperatures, the A_{c3} temperatures were modelled according to the Kasatkin [38] equation which is given by:

$A_{c3} = 912 – 370C – 27.4Mn +27.3Si – 6.35Cr – 32.7Ni + 95.2V + 190Ti + 72.0\ Al + 64.5Nb + 5.57W + 332S +276P + 485N – 900B + 16.2C\ Mn + 32.3C\ Si + 15.4C\ Cr + 48.0C\ Ni + 4.32Si\ Cr – 17.3\ Si\ Mo – 18.6\ Si\ Ni + 4.80Mn\ Ni + 40.5\ Mo\ V + 174C^2 + 2.46Mn^2 – 6.86\ Si^2 +0.322Cr^2 + 9.90Mo^2 + 1.24Ni^2 – 60.2V^2$

The calculated and experimental tempertures are given in Table 4.2 below for the two steels.

Table 4.2 Experimental and calculated A_{c3} temperatures.

Steel	Calculated A_{c3}(^{o}C)	Experimental A_{c3} (^{o}C)
C-Mn	843.7	865.3
HCrLMo	847.2	931.9

The experimentally obtained A_{c3} temperature for the HCrLMo steel was 82℃ higher than the calculated value, while that for the C-Mn was higher by 22℃. Typically, austenitising temperatures are taken 50℃ above the A_{c3} temperature. Therefore a suitable austenitising temperature determined for the C-Mn steel was 916℃, an approximate 50℃ above the experimental A_{c3} temperature. The HCrLMo steel was subjected to further scrutiny since austenitising 50℃ above the experimental Ac_3 seemed rather high and was likely to result in grain growth.

Two samples from the HCrLMo steel were thus heated to 935℃ and 955℃ respectively before cooling in the dilatometer. The change in M_s temperature was considered due to the impact of complete carbide dissolution on transformation temperatures. A fully austenitised material with all of its alloying elements in solid solution will give a lower M_s temperature on quenching and the latter can then be used as an indication of the effectiveness of the solution treatment.

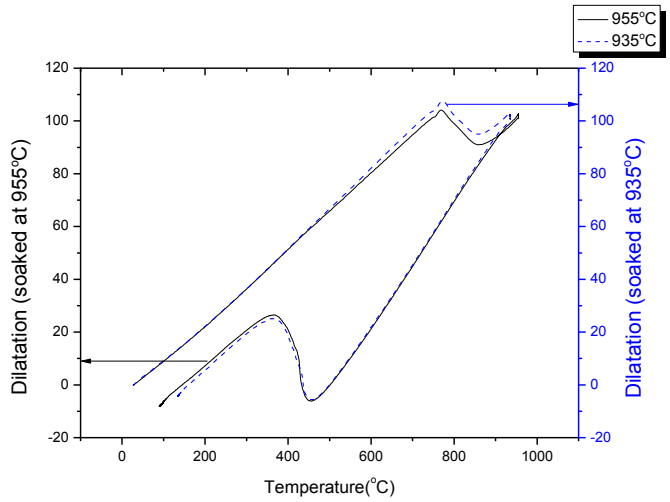

Figure 4.4.3 Superimposed dilatometric signals of austenitisation of HCrLMo steel samples at 955℃ and 935℃ and cooled at 10℃ /s.

Figure 4.4.3 shows dilatometric signals of samples of the HCrLMo steel austenitised at 955℃ and 935℃ respectively. No difference was found in the M_s temperature of these two samples. This indicated that soaking of the HCrLMo steel samples at 955℃ did not induce any further dissolution of carbides than soaking them at 935℃.

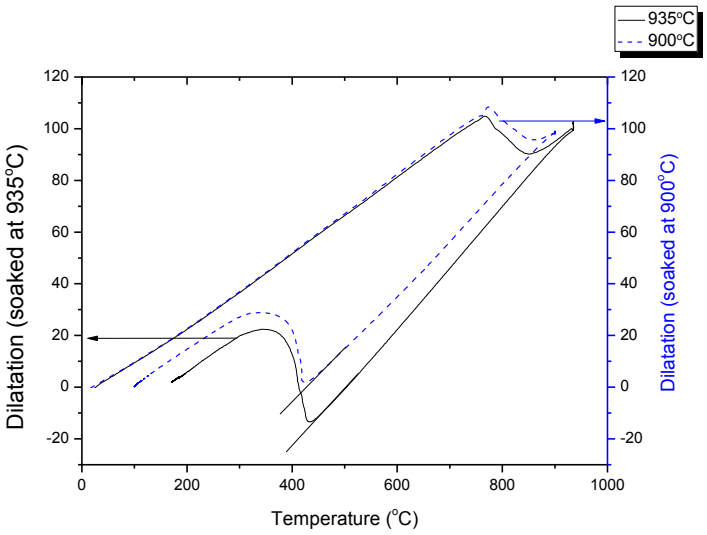

Figure 4.4.4 Superimposed dilatometric signals of HCrLMo steel samples austenitised at 900℃ and 935℃ respectively and cooled at 18℃/s.

The change in M_s temperature was also considered between samples austenitised at 900℃ and 935℃. The M_s obtained for the sample austenitised at 900℃ was surprisingly lower than

UNIVERSITEIT VAN PRETORIA
UNIVERSITY OF PRETORIA
YUNIBESITHI YA PRETORIA

that for the sample soaked at 930℃ (undissolved carbides at 900℃ should lead to a higher M_s). However, the difference was small.

Next, the effect of austenitising temperature on grain growth was considered. The grain sizes of samples solution treated at 900℃ and 935℃ respectively were measured on optical micrographs using the linear intercept method. At 935℃ the mean linear intercept was 26.7µm and 20.8µm at 900℃. Thus a rise in austenitisng temperature by 35℃ resulted in an increase in grain size by 5.9 microns. It is known that austenite grain size can affect hardenability and thus cause a shift in the CCT diagram.

However, it was found that austenitising the HCrLMo samples at 930℃ did not shift the CCT diagram significantly if compared to a soaking temperature of 900℃. Table 4.3 shows the transformation temperatures obtained after austenitising HCrLMo samples at 900℃ and 930℃ respectively and cooling at the same rates. The transformation temperatures from 2 to 18℃/s are the temperatures at which bainite began to form whilst those at 30℃/s represented the M_s. The relatively small difference between the transformation temperatures implied that CCT curves constructed from the two austenitising temperatures would be similar.

Table 4.3 Transformation temperatures obtained after austenitising HCrLMo steel samples at 900℃ and 930℃ and cooling at different rates.

Cooling rate (^{o}C/s)	Transformation temperature after soaking at 930^{o}C	Transformation temperature after soaking at 900^{o}C	Absolute difference (^{o}C)
2	558.0	572.1	14.1
5	519.8	517.0	2.8
10	476.0	472.3	3.7
18	441.6	439.0	2.6
30	434.8	421.0	13.8

4.4.1.2 Carbide and nitride dissolution

Thermocalc simulations of the dissolution temperature of AlN show that at all the austenitising temperatures used for the HCrLMo steel these precipitates are not dissolved. However, some amount of dissolution for the C-Mn steel is expected in the region of 900℃ although complete dissolution of AlN is only attained at about 1000℃.

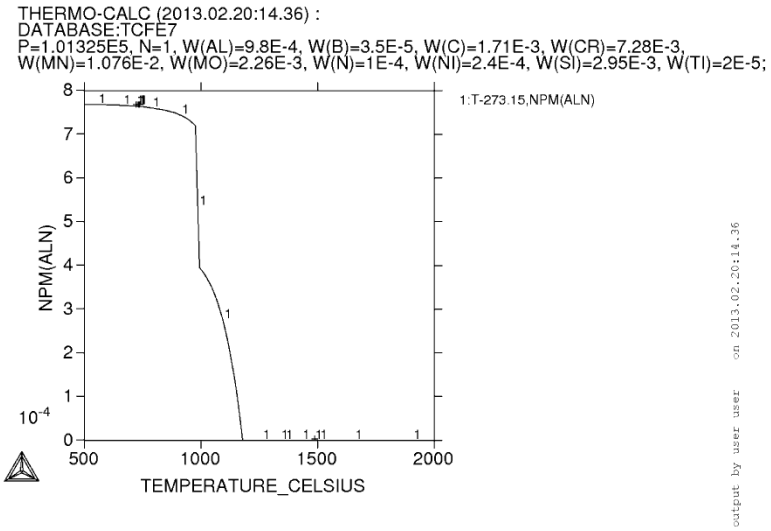

(a)

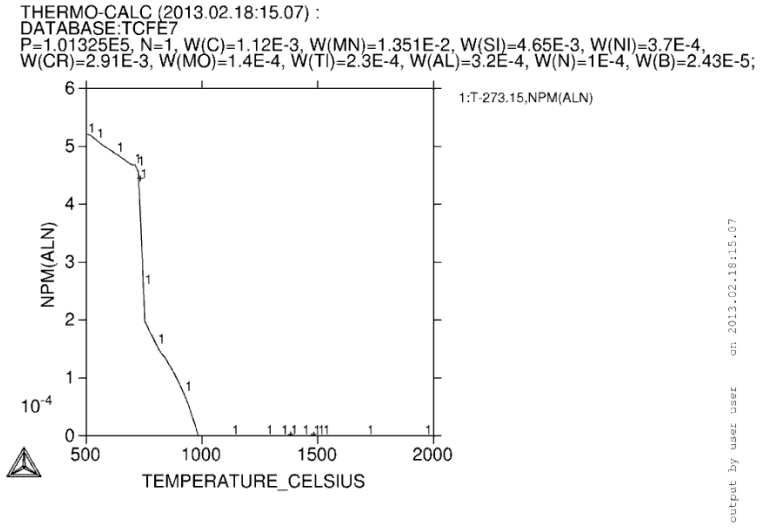

(b)

Figure 4.4.5 Thermocalc graphs of temperature versus AlN content for (a) the HCrLMo steel and (b) C-Mn steel. NMP = mole fraction.

A high austenitising temperature of 1000℃ at which complete dissolution of AlN would be achieved according to Figure 4.4.5, also promotes excessive grain growth. This was therefore ruled out as a possible austenitising temperature.

UNIVERSITEIT VAN PRETORIA
UNIVERSITY OF PRETORIA
YUNIBESITHI YA PRETORIA

Optical micrographs of the samples which were austenitised at 930℃, 935℃ and 955℃ had dark spots remaining in the microstructures that at first appeared to be carbides. The micrograph of such a sample which was austenitised at 955℃ and quenched to form martensite at 60℃/s is shown in Figure 4.4.6.

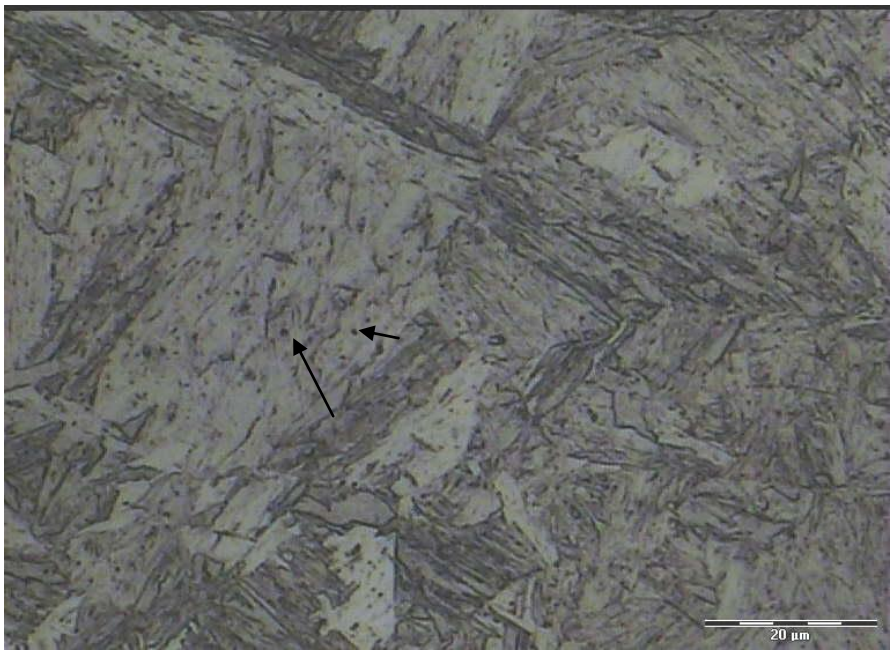

Figure 4.4.6 Microstructure of a HCrLMo steel sample austenitised at 955℃ and soaked for 20 minutes before cooling at 60℃/s. The spots arrowed were found to be etch pits and not second phases.

The suspicion that the spots are carbides was verified by SEM-EDS examination of the sample. The dark spots had the same approximate composition as the matrix and when the sample was viewed in backscatter mode, no compositional contrast was observed. Therefore what appeared to be carbides or nitrides appear may have been to be etch pits. Therefore, it was ascertained that carbides were in solution at the solution treatment temperature of 955℃.

4.4.1.3 Tests for A_{c1} and A_{c3} temperatures

In this section, attempts at finding the equilibrium A_{c1} and A_{c3} temperatures of the HCrLMo steel were made by using slow cooling rates after austenitising.

The first trial run was done by heating a dilatometer sample to 900℃ followed by cooling over the duration of 1 hour at a rate of 0.22℃/s to about 100℃. The temperatures were

UNIVERSITEIT VAN PRETORIA
UNIVERSITY OF PRETORIA
YUNIBESITHI YA PRETORIA

measured from dilatometric signals by reading off the points of inflection on cooling in Figure 4.4.8.

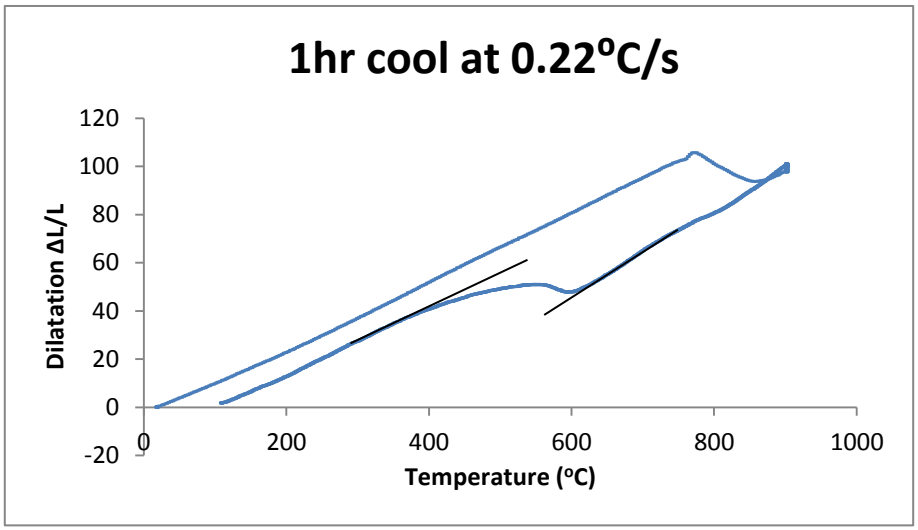

(a)

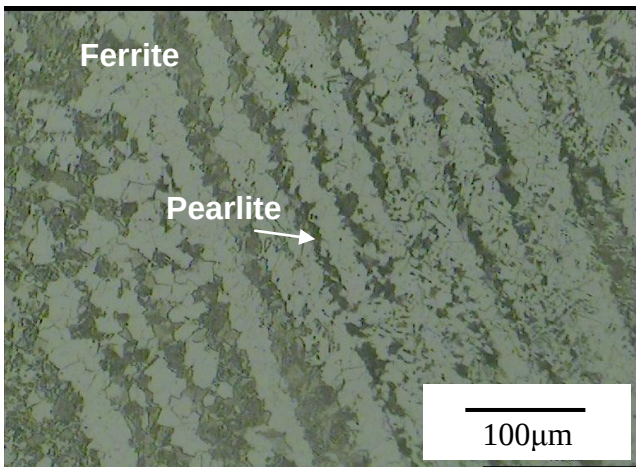

(b)

Figure 4.4.7 (a) Dilatometric signal of the HCrLMo steel using a 0.22℃/s cooling rate after austenitising at 900℃. The A_{r3} and A_{r1} temperatures recorded were 621℃ and 452℃ respectively.(b) Optical micrograph showing the microstructure obtained.

The A_{r3} and A_{r1} temperatures of 621℃ and 452℃ respectively were lower than expected. Bands of ferrite and pearlite were obtained with possibly some martensite or bainite in the grey areas of the micrograph in Figure 4.4.7. To obtain equilibrium temperatures, a lower

UNIVERSITEIT VAN PRETORIA
UNIVERSITY OF PRETORIA
YUNIBESITHI YA PRETORIA

cooling rate of 0.07°C/s was then used. The heating rate used for both the 0.22°C/s and the 0.07°C/s cooling rates was 1.5°C/s.

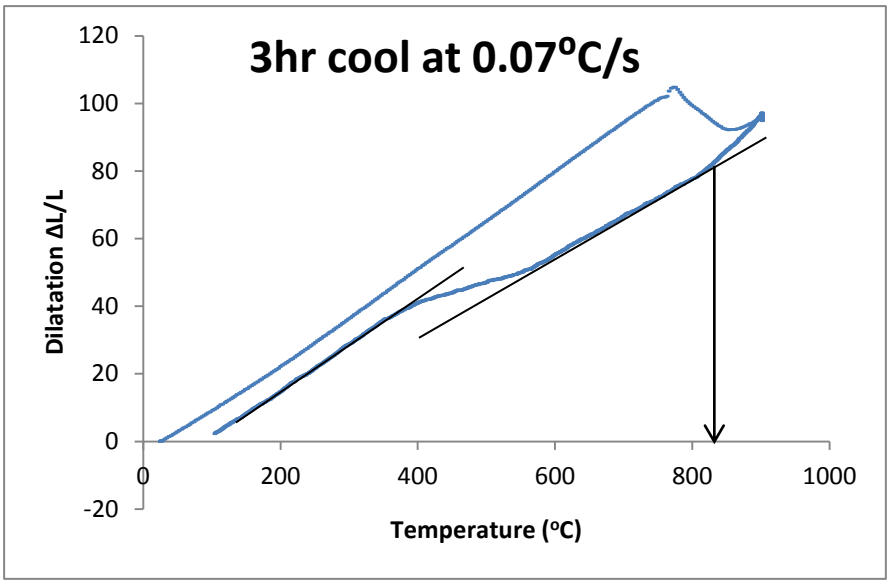

(a)

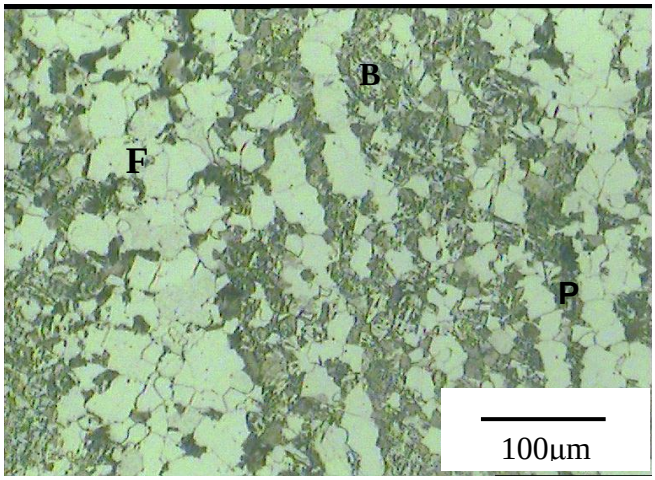

(b)

Figure 4.4.8 (a) The graph and (b) microstructure of the decomposition product in the steel HCrLMo after slow cooling at 0.07°C/s. The product is a mixture of ferrite (F), pearlite (P) and bainite (B).

The temperatures of the transformation obtained in this case were A_{r3} = 553°C and A_{r1} = 404°C. The result was still lower than was previously obtained and it seems that the slower degree of cooling did not result in the equilibrium conditions as was expected. Before the

UNIVERSITEIT VAN PRETORIA
UNIVERSITY OF PRETORIA
YUNIBESITHI YA PRETORIA

expansion at 553°C, a slight deviation from linearity on cooling was observed at 836°C as indicated by the arrow in the graph in Figure 4.4.8. The corresponding micrograph shows three distinct phases. In accordance with this, it was deduced that the ferrite formed at the higher temperature of 836°C, although no contraction was detected at this point and that 553°C should not be regarded as the A_{r3} temperature. It also explains why a lower 'A_{r3}' was found at this cooling rate than at the higher cooling rate of 0.22°C/s.

The sample heating rate was reconsidered since an equilibrium heating is more likely to produce a more homogeneous austenite and the slow cooling that follows will thus give transformation temperatures within a more acceptable range. A sample of the steel HCrLMo was thus heated at 0.246°C/s to 900°C then cooled at the rate previously employed of 0.07°C/s. The result is given below.

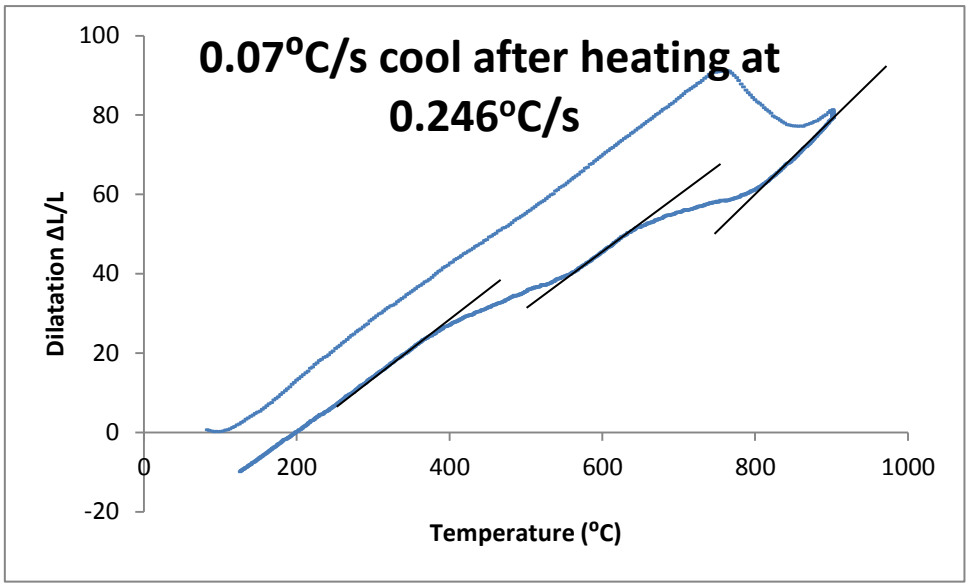

Figure 4.4.9 Graph of a sample of the steel HCrLMo with a 0.074°C/s cooling rate showing two transformations at A_{r3} = 813.5°C, A_{r1} = 656.9°C, B_s = 561.8°C and B_f = 398.5°C.

The A_{r3} temperature of 813.5°C obtained in this instance was much higher than previously found. Two distinct transformations were observed on the dilatometric signal in Figure 4.4.9. The first transformation as indicated by the inflection at the higher transformation temperature of 813.5°C was a ferrite transformation. The corresponding micrograph in Figure 4.4.10 confirmed this. The second inflection at the lower transformation temperature of 561.8°C was where bainite began to form from the remaining austenite. These results confirm

UNIVERSITEIT VAN PRETORIA
UNIVERSITY OF PRETORIA
YUNIBESITHI YA PRETORIA

the importance of slow heating in addition to slow cooling when searching for equilibrium critical temperatures.

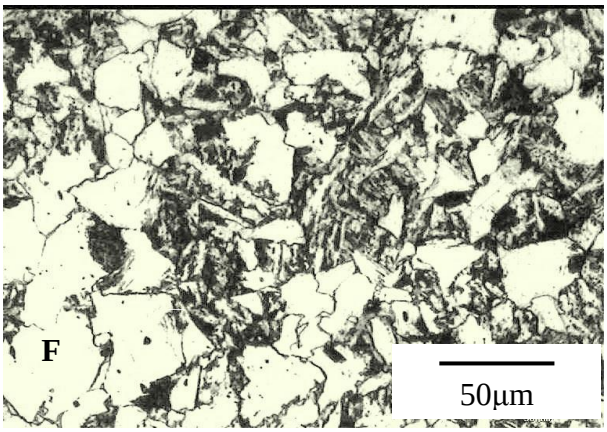

Figure 4.4.70 Microstructure of sample of the steel HCrLMo slow heated at 0.246℃/s and cooled at a cooling rate of 0.074℃/s.

Since there was a second transformation after the pearlite-ferrite formed, this showed that not all the austenite transformed to pearlite, as would be expected in an equilibrium cool. Therefore a final attempt at obtaining the A_{r1} and A_{r3} temperatures approaching A_{c1} and A_{c3} equilibrium temperatures respectively was made by cooling at a rate of 0.028℃/s. Figure 4.4.11 shows the dilatometric signal with the transformation temperatures obtained.

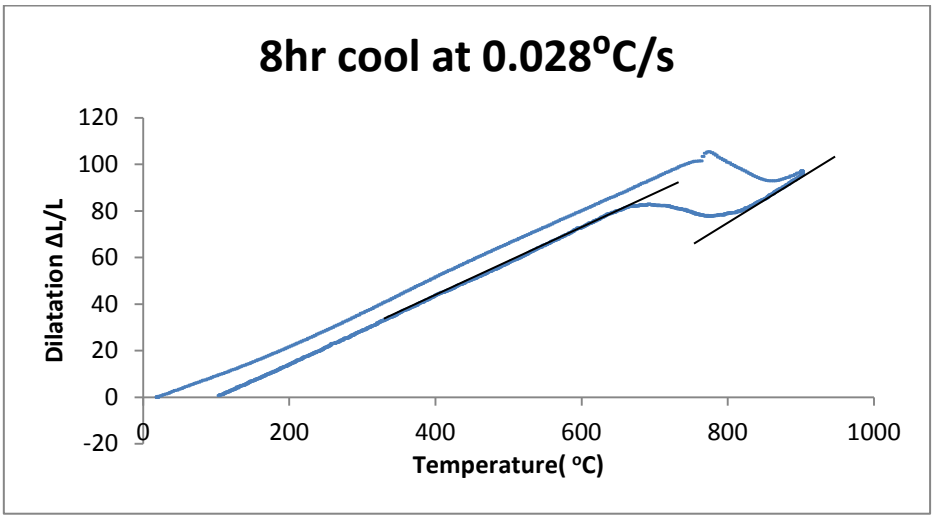

Figure 4.4.11 Graph of a sample of the steel HCrLMo with a cooling rate of 0.02 °C/s and where the critical transformation temperatures were found at A_{r3} = 829.7°C and A_{r1} = 682.4°C.

The A_r temperatures found after cooling a sample at 0.028°C/s, which was the lowest cooling rate used, were found to be closest to equilibrium and thus the final critical temperatures were taken as A_{c3} = 829.7°C and A_{c1} = 682.4°C.

Note that the dilatometer cannot distinguish between pro-eutectoid ferrite and pearlite formation hence a single expansion is recorded where the ferrite forms below the A_{c3} temperature [64].

4.4.2 Partial CCT diagrams

The partial CCT diagrams of the HCrLMo and HMoLCr steels were constructed by austenitising dilatometer samples at 900°C and 930°C respectively, followed by continuous cooling at various linear cooling rates to room temperature. The same followed for the C-Mn steel which was austenitised at 916°C. Figure 4.4.12 shows the CCT diagrams that were constructed from the transformation temperatures given in the dilatometry curves. The cooling rates plotted on a logarithmic scale show a slight curvature not visible on the figure.

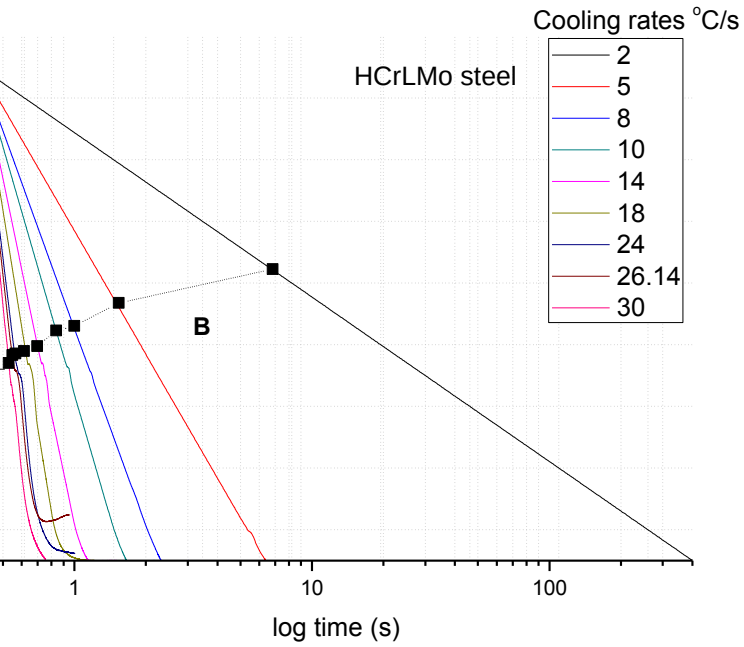

(a)

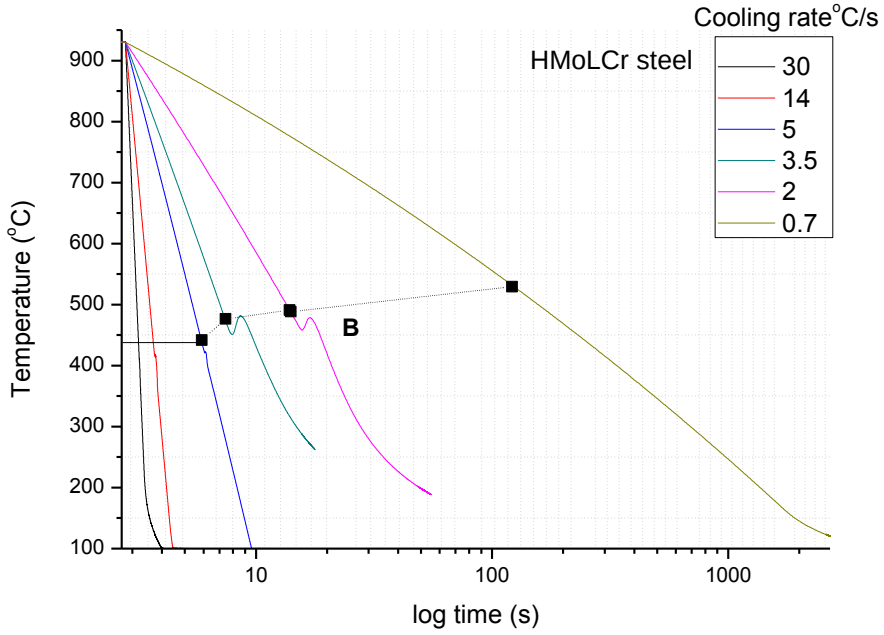

(b)

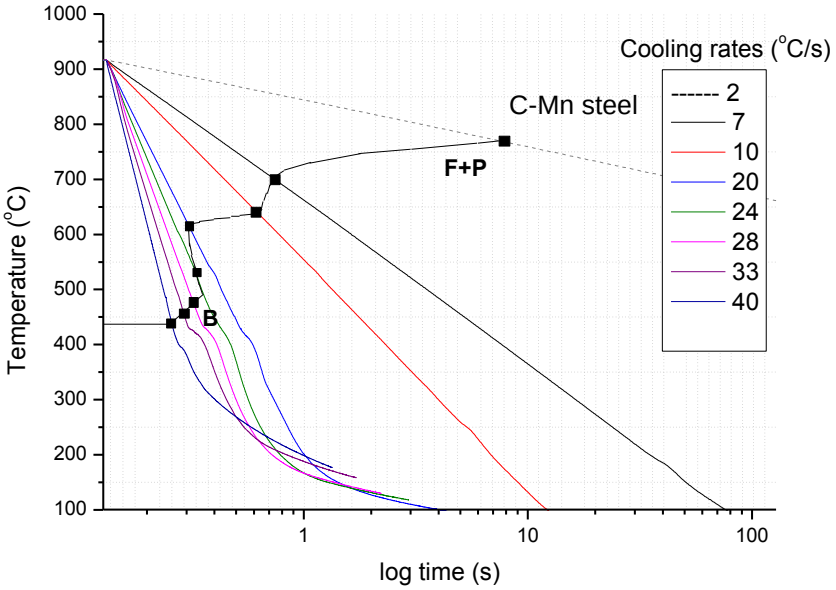

(c)*Figure 4.4.12 Partial CCT diagrams for (a) the HCrLMo steel (b) the HMoLCr steel and (c) the C-Mn steel. F represents ferrite, P pearlite and B bainite.*

The M_s temperatures of the HCrLMo steel were found from an average of four cooling rates and were 423℃, 432℃, 430℃ and 421℃ with an average M_s of 426.5℃.

A critical cooling rate of 5℃/s to form only martensite was found for the HMoLCr steel while that for the HCrLMo steel of 30℃/s was found. This reflects the higher hardenability imparted by the high Mo content in the steel HMoLCr if compared to that of a high Cr content in the steel HCrLMo. The change in hardness with cooling rate is given in Table 4.4. Since the partial CCT consisted of only a bainite nose, the decreasing hardness with lower cooling rates was due to the bainitic ferrite which is a phase that is much softer than martensite. Cooling rates of 14℃/s and 5℃/s for the HMoLCr steel produced martensite. A larger quantity of bainite was produced when a sample was cooled at 0.7℃/s, this gave a lower hardness. The same followed for the HCrLMo steel, where the slowest cool of 2℃/s passed through a wider region of the bainite nose and resulted in more bainite in the microstructure.

UNIVERSITEIT VAN PRETORIA
UNIVERSITY OF PRETORIA
YUNIBESITHI YA PRETORIA

Table 4.4 HMoLCr steel micro-Vickers hardness with cooling rate. Load = 300 gf.

Cooling rate /$^{o}Cs^{-1}$	Hardness/HV
14	391.3
5	377.6
2	313.4
0.7	283.7

Table 4.5 HCrLMo steel micro-Vickers hardness with cooling rate. Load = 100 gf.

Cooling rate/$^{o}Cs^{-1}$	Hardness/HV
100	381.9
30	402.7
26	409.7
24	387.8
14	391.5
10	376.0
8	360.8
5	335.7
2	272.4

4.5 Isothermal transformations

4.5.1 Preliminary tests

A preliminary test was conducted on a HCrLMo steel dilatometer sample to show the feasibility of producing a bainite-martensite structure. In this trial run the sample was heated to 900℃ and solution treated at this temperature for 15 minutes. The sample was then cooled to 443℃ at 5℃/s and subsequently quenched in He at 60℃/s. The cooling rate was chosen to enter the bainite nose without any isothermal incubation time.

When analysed individually, the 5℃/s cool is slow enough to allow bainite to form and the 60℃ is a fast quench that results in martensite forming from any remaining austenite. Therefore, cooling a sample at the two cooling rates combined in the sequence given was expected to result in a microstructure containing bainite and martensite. The dilatometric curve in Figure 4.5.1 was used to verify this.

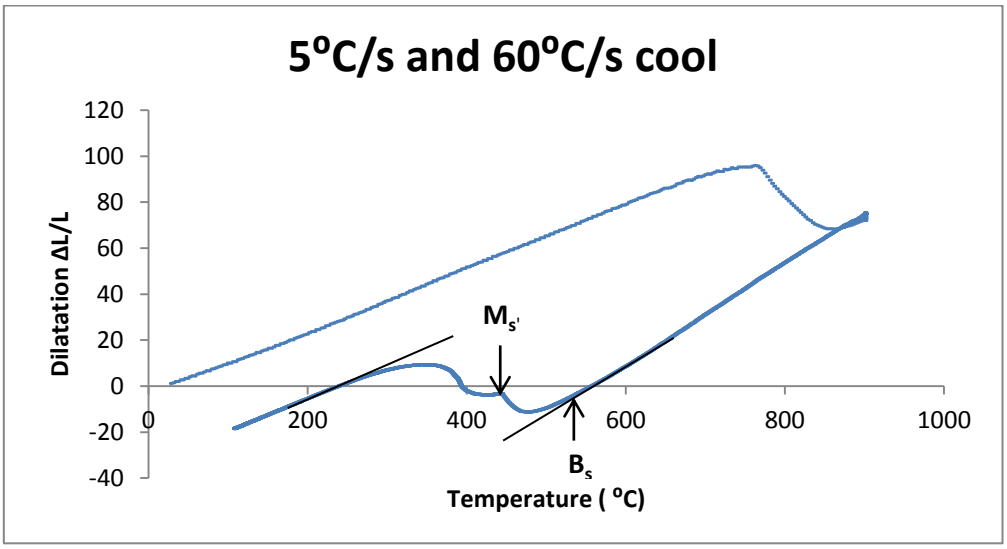

Figure 4.5.1 Double quench on steel HCrLMo, cooling rate interrupted at 443°C, B_s = 520°C.

Notice that the two transformations occurred as expected. The temperature of the first transformation corresponded to the B_s temperature found on quenching at 5°C/s. The arrow at the point labelled $M_{s'}$ indicates the start of the second transformation at which martensite forms from the untransformed austenite. Microstructural evidence in Figure 4.5.2 also showed that the two transformation products were indeed bainite and martensite.

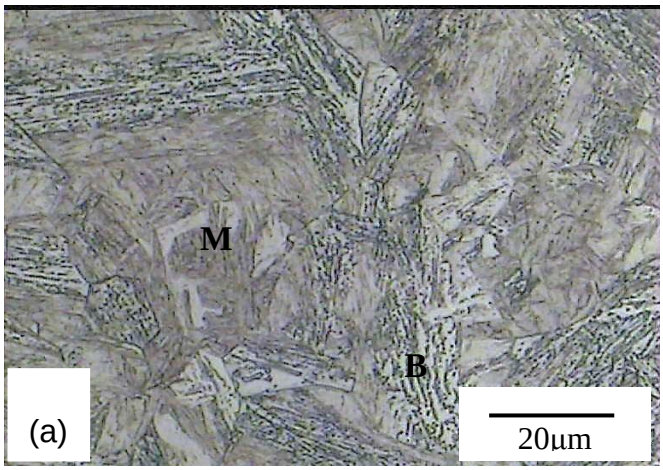

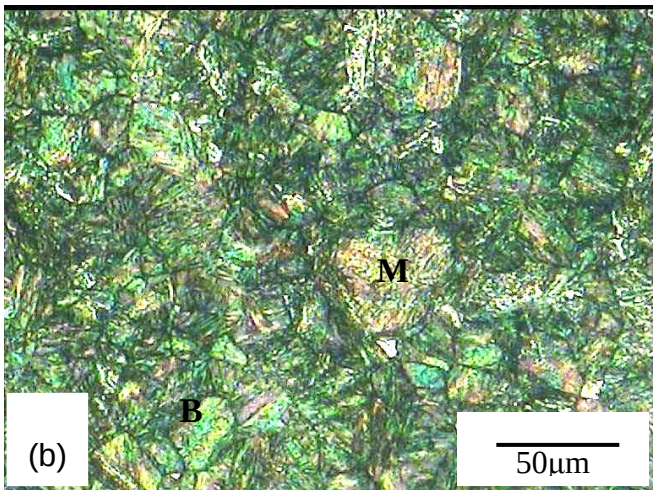

Figure 4.5.2 Optical micrographs of the mixed upper bainite-martensite microstructures in steel HCrLMo obtained after continuous cooling at 5℃/s and 60℃/s after (a) a Nital etch and (b) a 10% SMB etch. B is bainite and M is martensite.

The sample was first etched in a 2% Nital solution to reveal the microstructure. The same sample was polished and then etched in a 10% Sodium Metabisulphite (SMB) solution. This solution is a colour etchant that gives bainite a blue appearance and martensite a brown appearance when viewed in an optical microscope under polarised light.

4.5.2 Measurement of the volume fraction of bainite.

Isothermal heat treatments to form mixed structures of bainite and martensite were conducted and the volume fraction of bainite was calculated from the expansion line of the dilatometric signal. Figure 4.5.3 shows the dilatometric curve when dual phase bainite/martensite is obtained on cooling.

UNIVERSITEIT VAN PRETORIA
UNIVERSITY OF PRETORIA
YUNIBESITHI YA PRETORIA

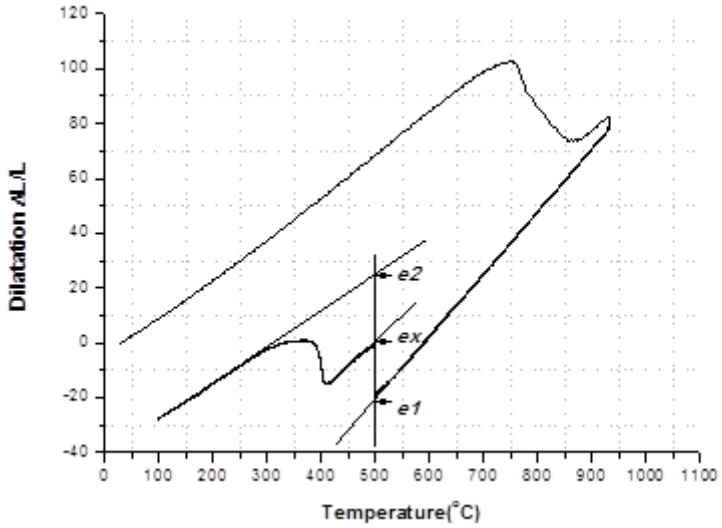

Figure 4.5.3 Dilatometric signal of isothermal transformation on a sample of the steel HCrLMo austenitised at 900℃ then cooled at 8℃/s to 484℃ and held for 20 s to form 67.8% bainite before cooling at 30℃/s to form martensite. The strains measured at e_1, e_2 and e_x were used to calculate the bainite volume fractions.

The magnitude of expansion of the dilatometric signal at the isothermal holding temperature was a measure of the amount of bainite that formed and was taken as a fraction of the maximum possible expansion of the sample at this temperature. This was done in accordance with the standard ASTM A1033-10. The formula for calculating the volume fraction of bainite is essentially derived from the lever rule:

Volume fraction = $\frac{ex-e1}{e2-e1}$……..……eq 4.1

Where e_i is the dilatation ΔL/L for:

i=2 at the maximum possible expansion at isothermal treatment temperature,

i=1 at the extrapolated cooling curve and

i=x at the point where the transformation of austenite to bainite is terminated by the quench.

UNIVERSITEIT VAN PRETORIA
UNIVERSITY OF PRETORIA
YUNIBESITHI YA PRETORIA

4.6 Johnson Mehl Avrami Kolmogorov (JMAK) kinetics

4.6.1 Sigmoidal curves and Avrami Exponents

The Johnson Mehl Avrami approach was applied to the isothermal transformation of austenite to bainite in the HCrLMo and HMoLCr steels. Upper bainite was formed in the steels by isothermal heat treatment at 484℃ for the HCrLMo steel samples and at 498℃ for the HMoLCr steel samples. The temperatures used resulted in similar estimated undercoolings of 132℃ and 134℃ below the B_s temperatures. Similar undercoolings below the B_s were used to ensure that the estimated driving forces for the bainite transformation were approximately similar by assuming an equivalent enthalpy of formation in the two steels. The driving force to form bainite was calculated in Thermo-Calc from the difference in free energies of the system at the austenitising temperatures and at the T_o temperature. The difference in free energy for the HCrLMo steel was -13409.1J/mol and for the HMoLCr steel -15274J/mol. The driving forces for the formation of bainite in the two steels differed by about 14% and were, therefore, relatively similar.

The volume fractions obtained after varying the isothermal holding time were plotted as a function of isothermal transformation time.

UNIVERSITEIT VAN PRETORIA
UNIVERSITY OF PRETORIA
YUNIBESITHI YA PRETORIA

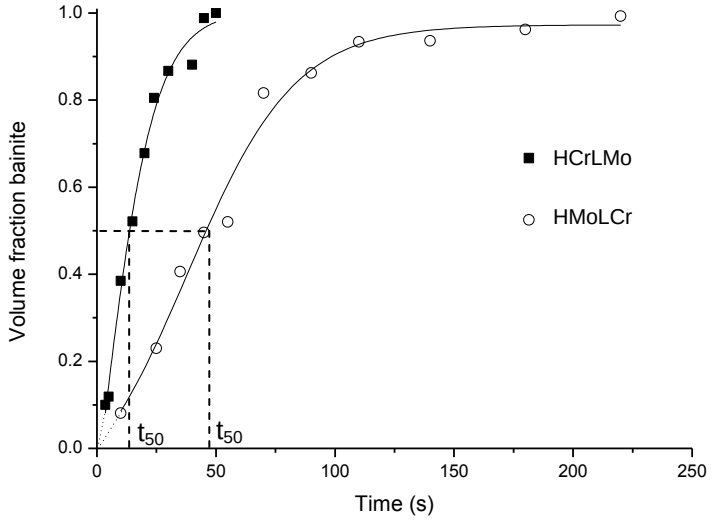

Figure 4.6.1 Volume fractions of bainite plotted as a function of time at isothermal temperatures for the two steels HCrLMo and HMoLCr. The time taken for 50% to form is shown as t_{50}.

The sigmoidal curves for the two steels give some indication of the growth kinetics under the conditions employed. Figure 4.6.1 shows that the HMoLCr steel took a significantly longer time to transform to a fully bainitic structure than the HCrLMo steel. The transformation was halfway complete in 47 seconds in the HMoLCr steel whilst it took a mere 14 seconds in the HCrLMo steel. This shows that the nucleation and growth rate of upper bainite was significantly higher in the HCrLMo steel than in the HMoLCr steel. The results are further discussed in section 5.4.

4.6.2 Depression of M_s temperatures

Using the above dilatometric curves, the progressive lowering of the M_s temperature of the remaining austenite could be followed as the volume fraction of bainite increased.

UNIVERSITEIT VAN PRETORIA
UNIVERSITY OF PRETORIA
YUNIBESITHI YA PRETORIA

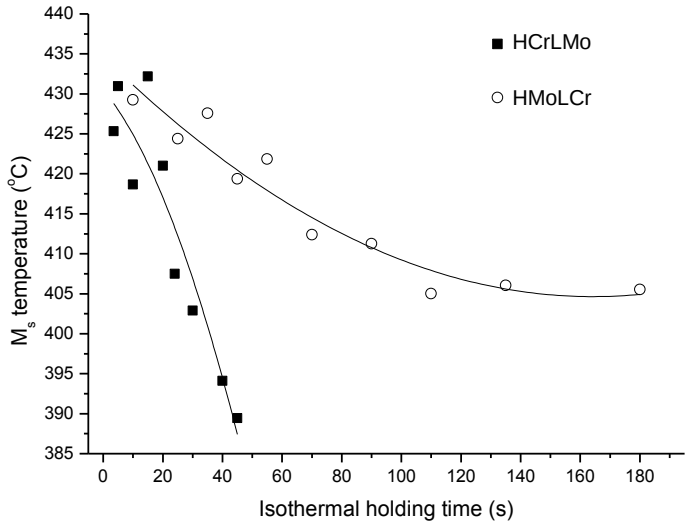

Figure 4.6.2 Graph of M_s temperatures with isothermal holding time for both steels.

A decrease in the M_s temperatures as increasing amounts of bainite were formed was evident in both steels. Nash et al observed the same reduction of M_s in a 0.58%C – 0.82%Mn – 0.04%Si – 1.9%Ni – 0.55%Cr – 0.77%Mo – 0.028%Al and 0.82%C – 0.86%Mn – 0.04%Si – 1.9%Ni – 0.55%Cr – 0.77%Mo – 0.031%Al (in wt%) steels. The M_s is dependent on carbon content and thus a decrease in M_s for both steels suggests that the carbon content in the untransformed austenite increased as more bainite formed [26, 65], a known feature of the bainite transformation as carbon is rejected from the ferritic bainite into the austenite.

UNIVERSITEIT VAN PRETORIA
UNIVERSITY OF PRETORIA
YUNIBESITHI YA PRETORIA

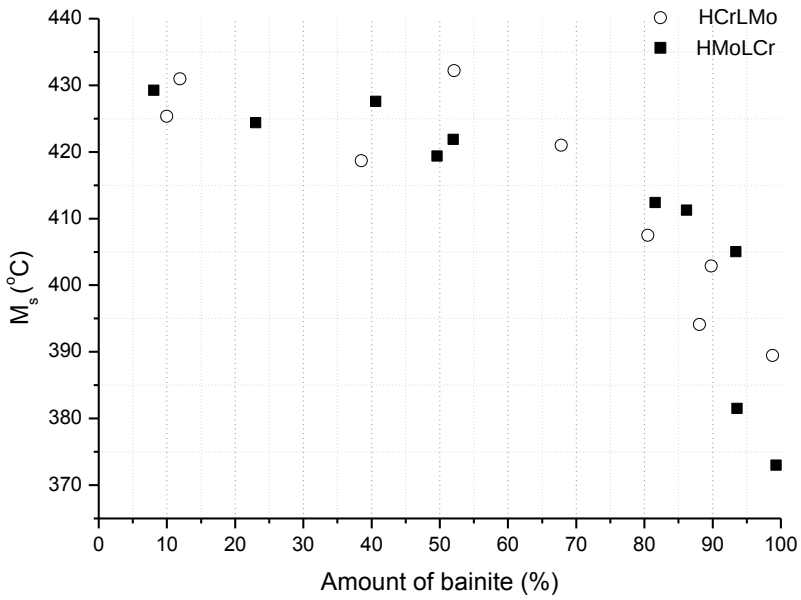

Figure 4.6.3 Graph of the effect of increasing volume fractions of bainite on the measured M_s temperatures.

The data in Figure 4.6.3 shows the effect of increasing amounts of bainite on the M_s temperatures of the untransformed austenite. There is an overlap of the M_s temperatures in the HCrLMo and HMoLCr steels which decrease as more bainite is formed. The dependence of the M_s temperatures on the volume fraction of bainite rather than the chemical composition, already points to a volume-driven effect, whereby the accumulation of rejected carbon in the untransformed austenite is the same for both steels in spite of large differences in the rate of transformation.

4.6.3 Electrolytic extraction of precipitates

The differing rates of decrease in the M_s temperature as can be seen from the graph of Figure 4.6.2, suggests that the rate of carbon rejection into the untransformed austenite was higher in the HCrLMo steel samples than in the HMoLCr samples. Together with the higher rates of formation of bainite (see Figure 4.6.1.) in the HCrLMo steel, this implies that bainite formation in the HMoLCr steel is slower due to the influence of the alloying elements Cr and

UNIVERSITEIT VAN PRETORIA
UNIVERSITY OF PRETORIA
YUNIBESITHI YA PRETORIA

Mo on the reaction. One possible cause of slower growth kinetics is the formation of cementite containing Cr or Mo (M_3C) rather than pure Fe_3C.

To determine if the upper bainite carbide is cementite containing some alloying elements, carbon extraction replicas were made from the HMoLCr steel sample consisting of a completely upper bainitic microstructure. The experiment was unsuccessful as AlN and TiN precipitates rather than cementite were extracted using this technique. The failure to extract the cementite using carbon extraction replicas was likely the result of insufficient etching depth. Figure 4.6.4 shows TEM images of the extracted particles.

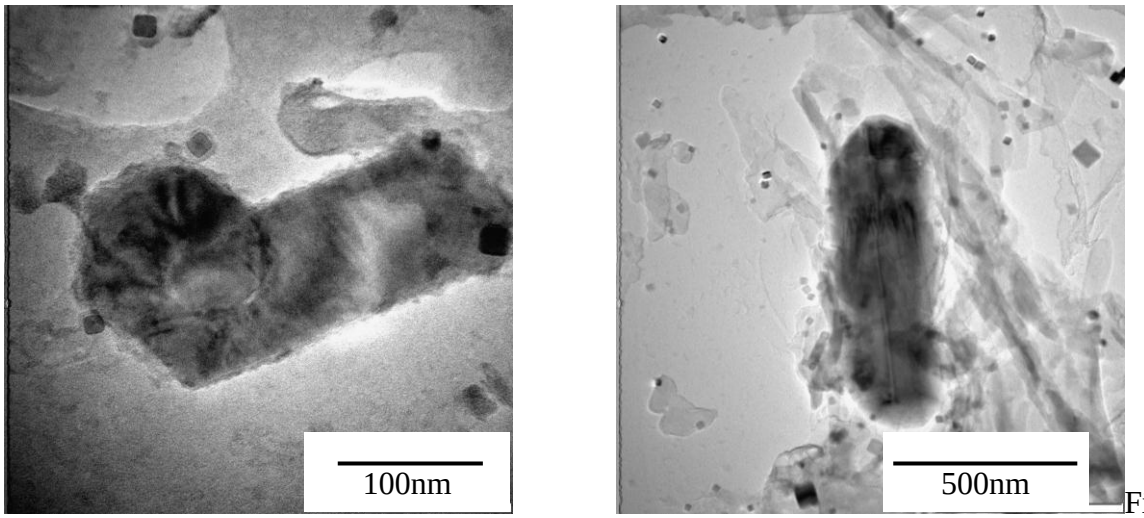

Figure 4.6.4 TEM images taken from carbon extraction replicas of HCrLMo steel with a 100% bainitic structure.

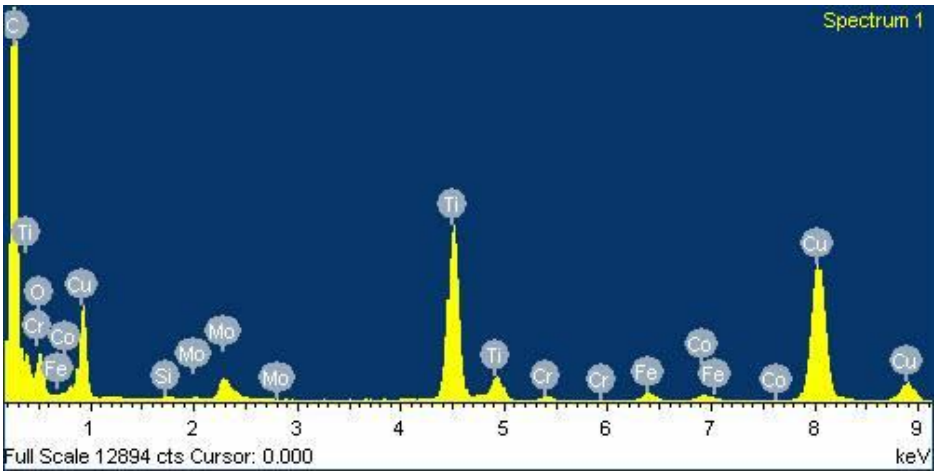

(a)

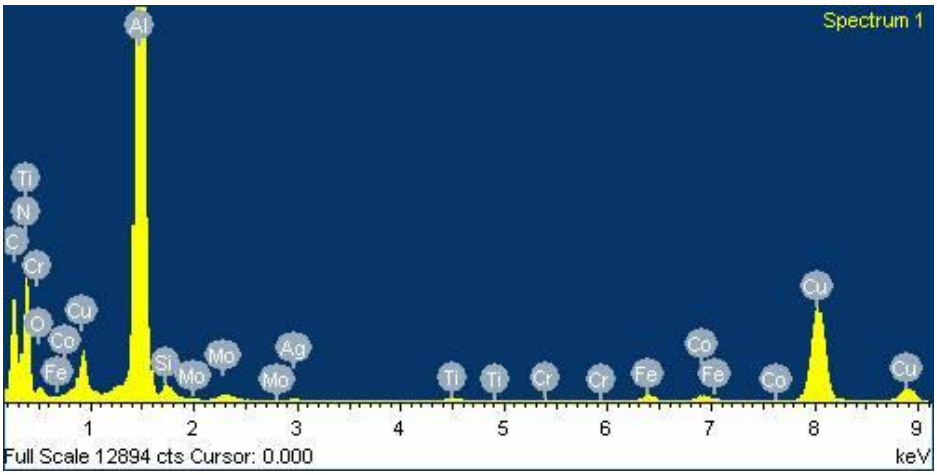

(b)

Figure 4.6.5 EDS spectra of (a) AlN and (b) TiN precipitates.

The high levels of copper detected in the spectra of Figure 4.6.5 are due to the copper TEM grids on which the specimens were mounted while the high carbon levels were detected from the carbon film which held the precipitates.

An alternative method was then used to extract larger volumes of carbide particles by electrolytic extraction. As before, a sample in which 100% upper bainite was formed was used. The precipitates were examined in a TEM in scanning mode. Images of particles were taken at randomly selected areas where their corresponding element maps and EDS spectra gave their chemical composition. Many of the larger precipitates extracted were TiN and AlN.

The TEM micrograph in Figure 4.6.6 shows a blocky precipitate which was likely a Titanium nitride particle. EDS maps of the precipitate had a high concentration of Titanium and Nitrogen. In addition to this, the spectrum affirmed the high Titanium and Nitrogen levels shown in the maps.

UNIVERSITEIT VAN PRETORIA
UNIVERSITY OF PRETORIA
YUNIBESITHI YA PRETORIA

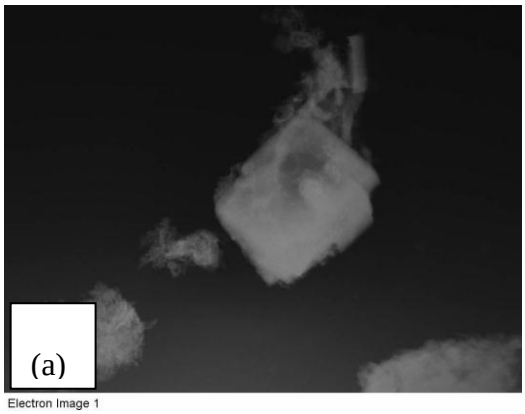

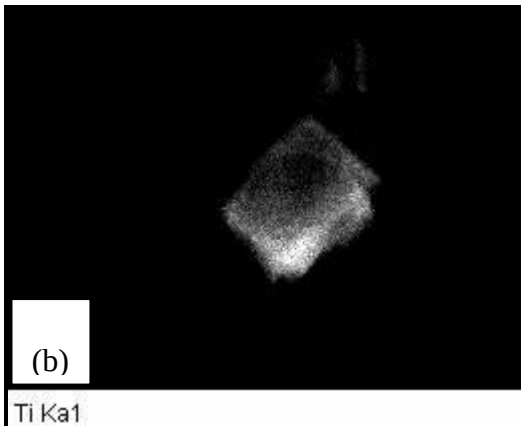

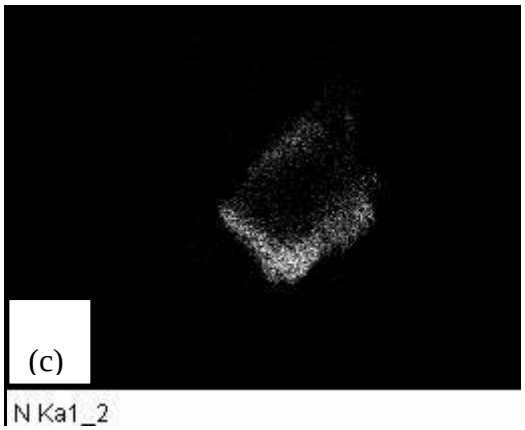

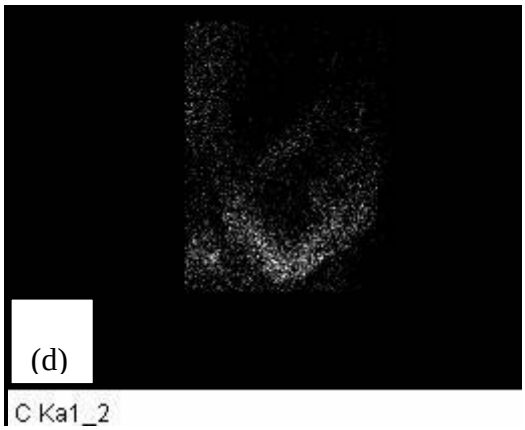

(d)

UNIVERSITEIT VAN PRETORIA
UNIVERSITY OF PRETORIA
YUNIBESITHI YA PRETORIA

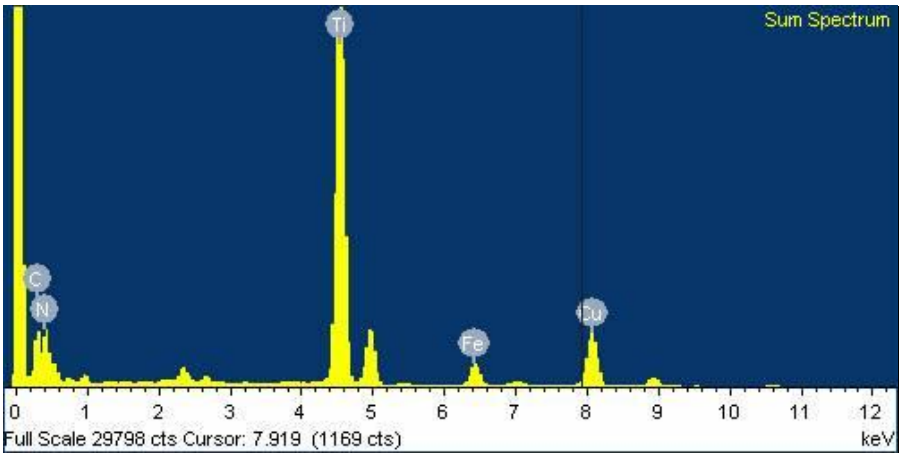

(e)

Figure 4.6.6 (a) TEM image of TiN particle. EDS maps of theTiN particle showing the distributions of (b) Ti, (c) N and (d) C. The spectrum of the particle is shown in (e).

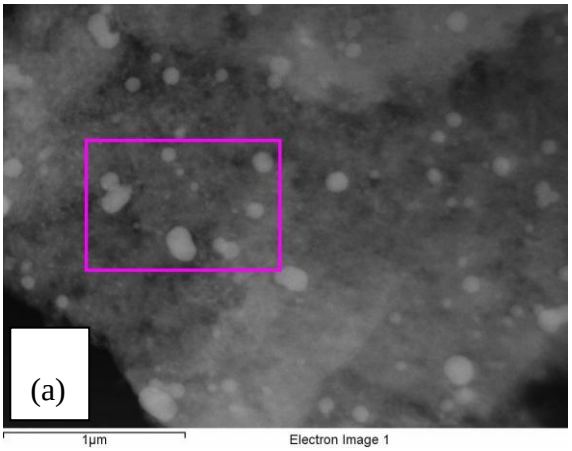

(a)

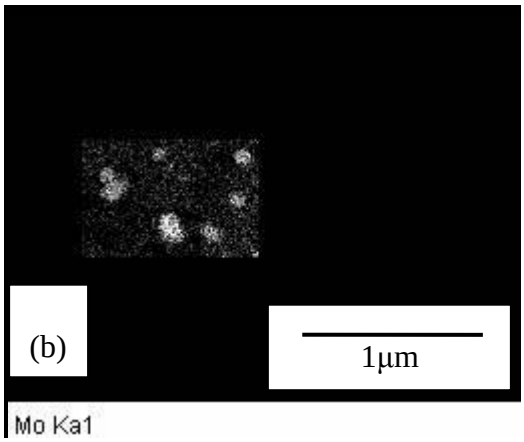

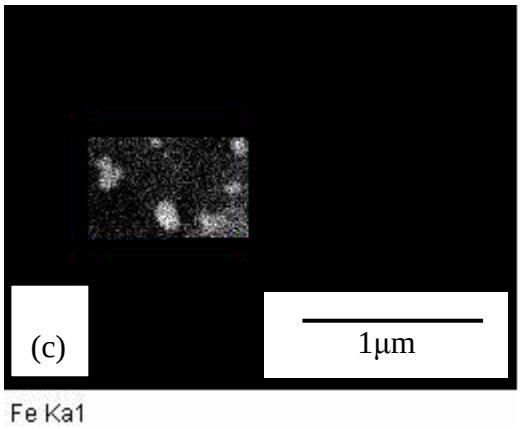

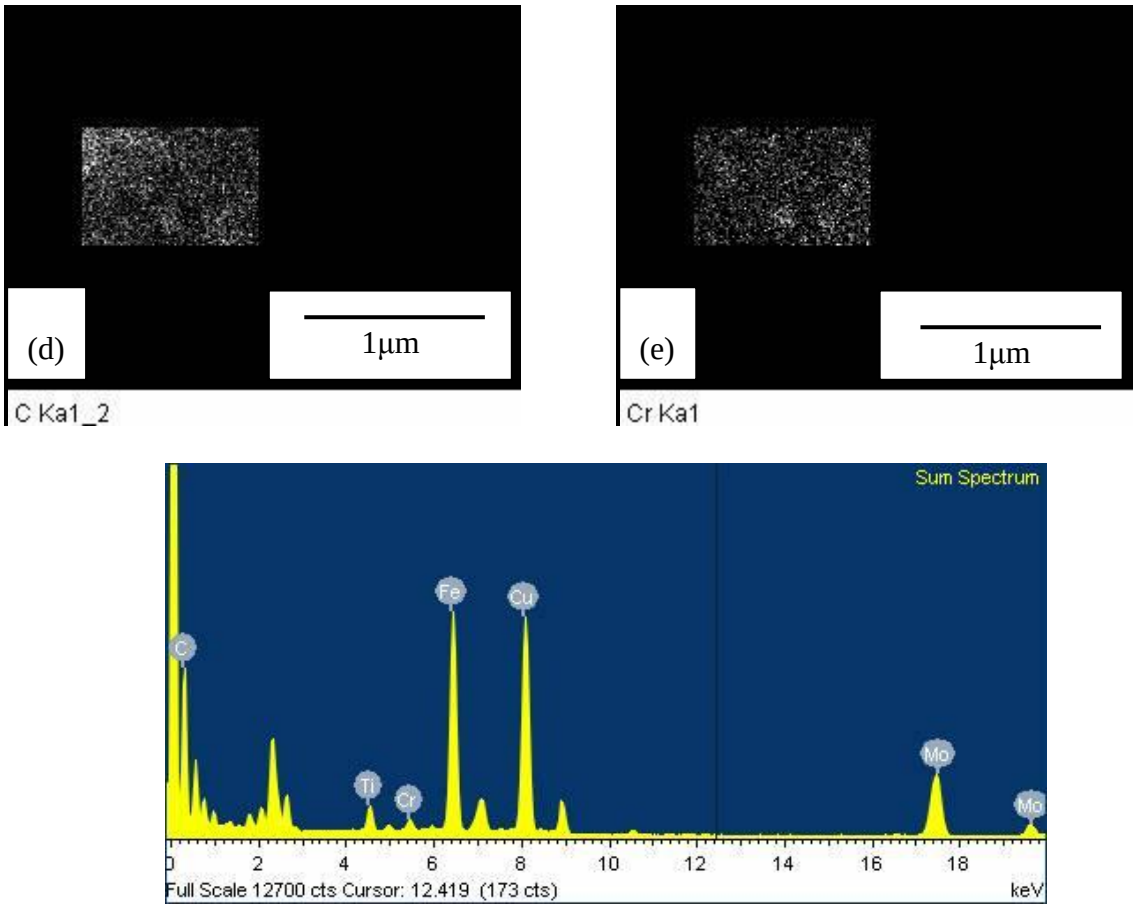

(f)

Figure 4.6.7 (a) TEM image of a Mo rich particle and EDS maps showing the distributions of (b) Mo (c) Fe (d) C (e) Cr and (f) is the spectrum of the particle.

The TEM micrograph in Figure 4.6.7 of round particles had a considerable concentration of Mo and Fe. The Mo and Fe EDS maps distinctively delineate the particles and their peaks on the spectrum are prominent. Minute amounts of Cr were also detected in these smaller particles as shown on the EDS map and the spectrum in Figure 4.6.7. The chemical compositions suggest that the particles are iron carbides with some Mo, most likely with a M_3C composition.

UNIVERSITEIT VAN PRETORIA
UNIVERSITY OF PRETORIA
YUNIBESITHI YA PRETORIA

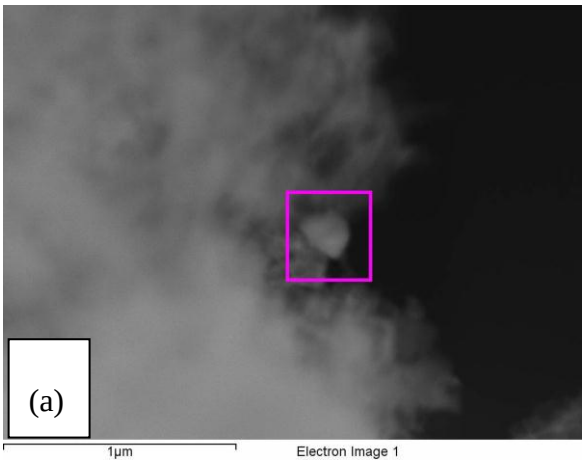

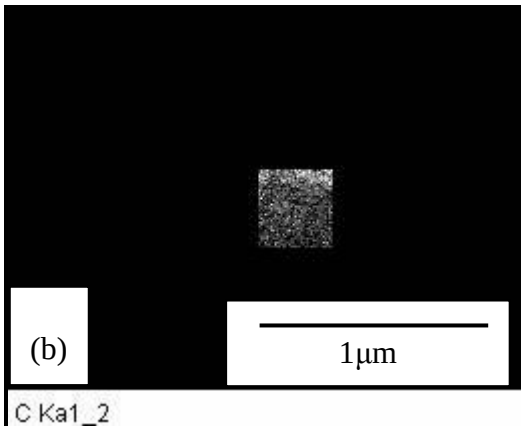

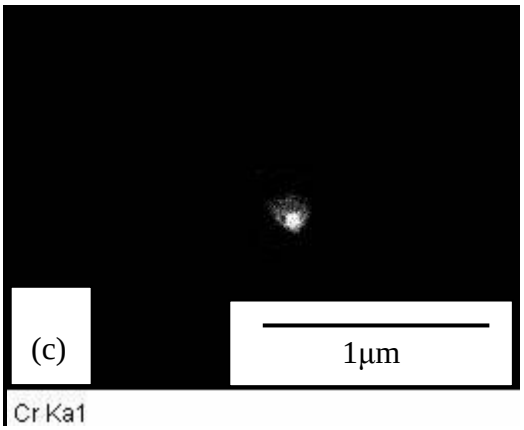

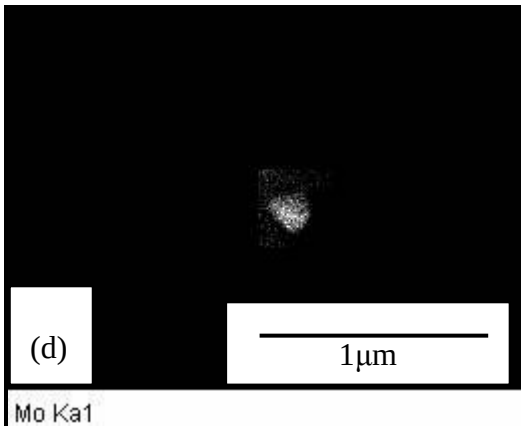

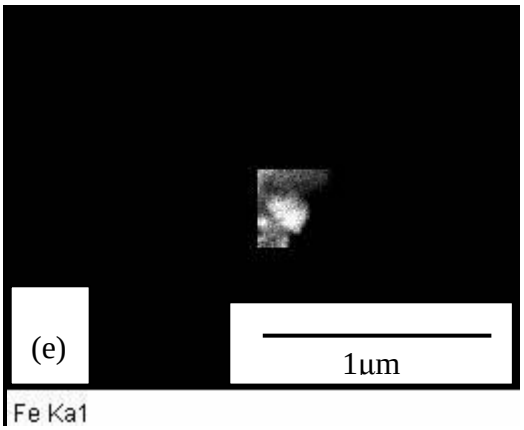

UNIVERSITEIT VAN PRETORIA
UNIVERSITY OF PRETORIA
YUNIBESITHI YA PRETORIA

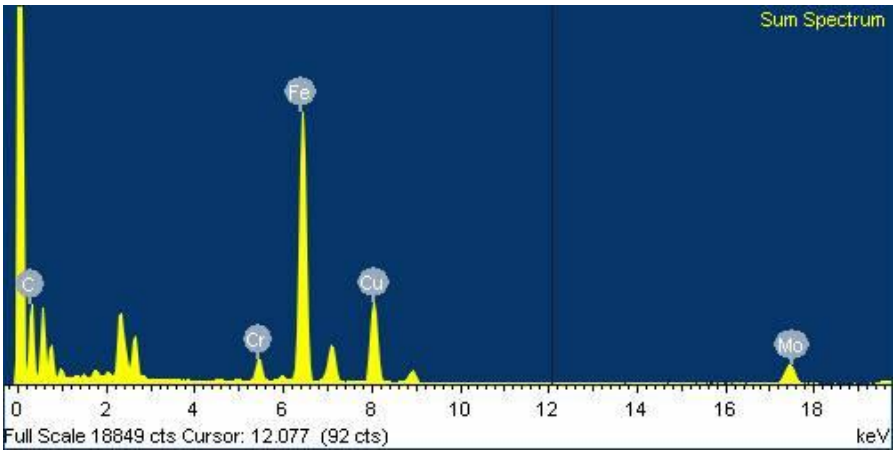

(f)

Figure 4.6.8 (a) TEM image of a Cr rich particle and EDS maps showing the distributions of (b) C (c) Cr (d) Mo and (e) Fe. The spectrum of the particle is shown in (f).

The particle analysed in Figure 4.6.8 shows the presence of Cr, Mo and Fe. The evidence from the EDS maps and spectra of the extracted particles suggests that the cementite contained some Cr and Mo elements.

4.7 Instrumented Charpy impact tests

4.7.1 Test parameters

4.7.1.1 Effect of tempering on hardness

Specimens cut from the HCrLMo and HMoLCr steel plates were machined into Charpy samples of dimension 10x10x55mm. The samples were heat treated in a thermomechanical simulator Gleeble 1500D^{TM} to produce various amounts of bainite in a martensitic matrix. The HCrLMo samples were cooled from the austenitising temperature at a rate of 8°C/s to 484°C, and the HMoLCr samples were cooled at 2°C/s to 498°C. The cooling rates were chosen to enter the bainite C-curve without any isothermal incubation time. After machining the Charpy groove, the samples were impact tested in an instrumented Instron Dynatup 9210.

The isothermal holding times to produce various amounts of bainite were found from the sigmoidal curves. Figure 4.7.1 shows the extrapolations from the selected amounts of bainite. The selected amounts were 10%, 25%, 60%, 75% and 90% bainite. Specimens with 100%

UNIVERSITEIT VAN PRETORIA
UNIVERSITY OF PRETORIA
YUNIBESITHI YA PRETORIA

martensite were produced by fast quenching from a muffle furnace into water and those with 100% bainite were produced in the muffle furnace after 20 minutes of isothermal holding.

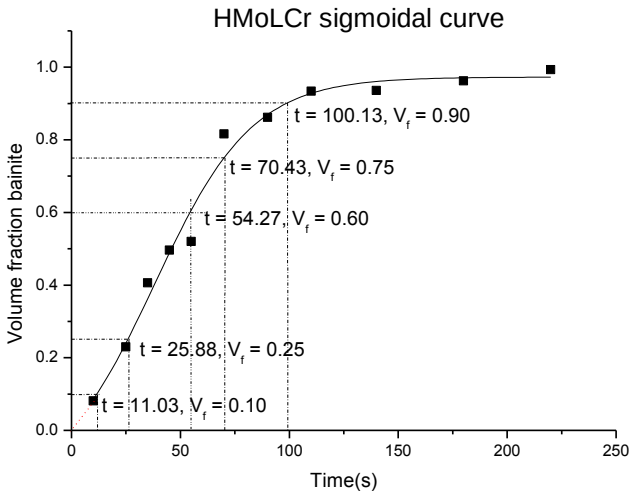

(a)

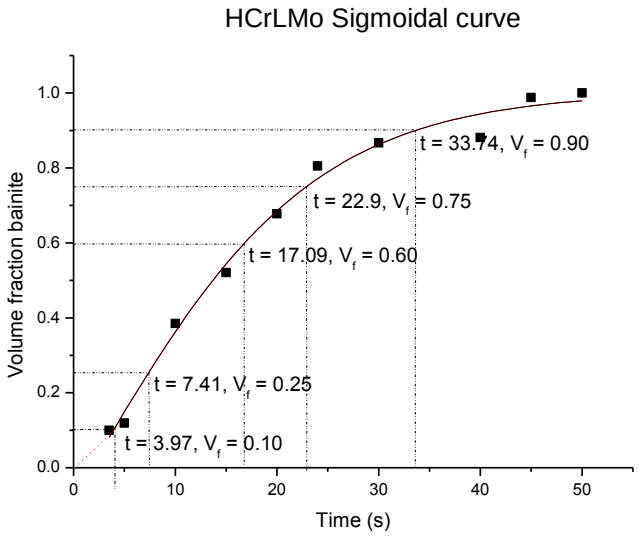

(b)

Figure 4.7.1 Sigmoidal plots and extrapolations used for heat treatment durations (a) in the HMoLCr and (b) HCrLMo steel Charpy specimens.

To ensure that the effect of bainite on toughness was isolated from that of the martensite which is brittle in the untempered state, the micro-hardness of the two phases was equalised

UNIVERSITEIT VAN PRETORIA
UNIVERSITY OF PRETORIA
YUNIBESITHI YA PRETORIA

by tempering. The hardness of untempered martensite was 419.3HV and that of the untempered bainite was 275.8HV. Tempering the mixed martensite-bainite samples at 500℃ for 30 minutes reduced the hardness of martensite to a level sufficient to eliminate the brittleness of martensite that in the untempered state would have obscured the effect of bainite. The bainite remained unaffected by tempering under these conditions. According to Bhadeshia [27], bainite has a greater degree of stability over a longer tempering period during tempering than does martensite. Figure 4.7.2 shows the effect of tempering on the Vickers hardness in a 0.14 wt% C steel containing bainite.

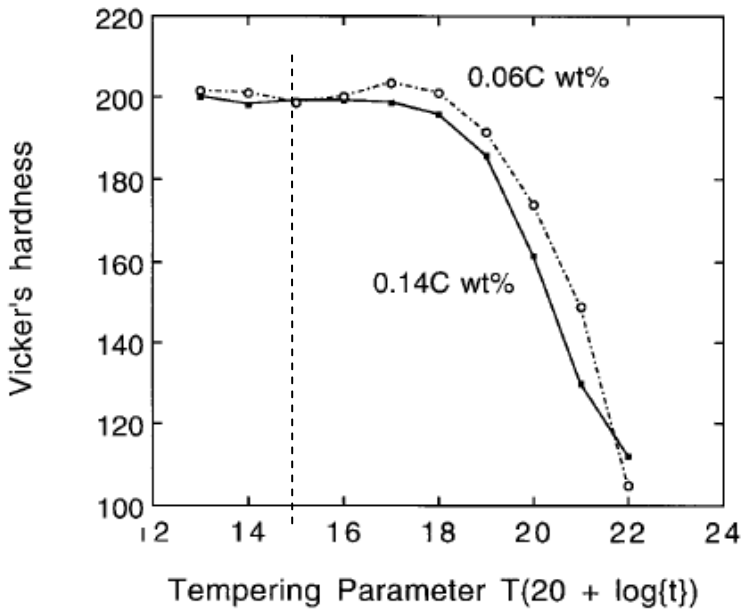

Figure 4.7.2 Change in hardness with tempering parameter (x10 ^{3}) for bainitic steel. T is the absolute temperature and t is time in hours. The dotted line represents the tempering parameter used in tempering the martensite in both of the steels HCrLMo and HMoLCr at 500℃ for 30 minutes to lower its hardness to that of the upper bainite [27].

When bainite forms much of the carbon is precipitated as cementite, there is therefore little carbon in solid solution in the ferrite, as opposed to quenched martensite. At the relatively high temperatures at which upper bainite forms, the microstructure undergoes recovery to a greater extent than does autotempered martensite. Tempered bainite therefore undergoes little recovery and negligible change in the morphology and density of the carbides. In contrast to this, the carbon in solid solution in martensite precipitates as fine carbides and the strength

UNIVERSITEIT VAN PRETORIA
UNIVERSITY OF PRETORIA
YUNIBESITHI YA PRETORIA

decreases. The coarsening rate of these very fine carbides after nucleation is thus higher in martensite than the already coarse cementite in upper bainite. The carbides in upper bainite in the untempered state are already coarse due to the inherent tempering that leads to growth during its formation. The tempering parameter calculated for the steels in this study which have a carbon content of 0.17 wt% was found to be 14 912 for 484℃ (757K) tempering and 15 188 for 498℃ (771K) tempering for a duration of 30 minutes. These values, with reference to Figure 4.7.1.2, show no change in the hardness of bainite when it is as-quenched versus when it is tempered. Therefore, tempering upper bainite did not produce any change in its toughness.

On the contrary, there is a definite increase in the toughness of martensite after it is tempered. An impact test on tempered and untempered Charpy samples of martensite in the steel HCrLMo was conducted. The Charpy impact energy of the tempered martensite sample was 69.7J and that of the untempered martensite sample was 28.3J of energy. Thus tempering mixed upper bainite-martensite samples isolated the effect of bainite on toughness by eliminating the brittleness of the martensite.

4.7.1.2 Effect of the notch position relative to the rolling direction

As the steel plates from which the Charpy samples were machined were hot rolled during their production, it was necessary to examine the effect on the impact toughness of the position of the V-notch relative to the rolling direction. This would serve to eliminate the effect of banding in the microstructure on toughness.

Two Charpy samples were machined from the HMoLCr steel plate in the rolling direction. One sample was notched on a plane transverse to the rolling direction, i.e. in the so-called L-T orientation and the other was notched on an orthogonal plane also transverse to the rolling direction or in the L-S orientation (see Figure 4.2.1). The specimens were then fractured and the impact energies obtained were 71.6 J and 67.7 J respectively. The difference of 3.9 J was not significant and it was thus concluded that the effect of microstructural banding was not significant in this steel if at all present. In addition to this, the hardness profiles taken along the two transverse directions were relatively constant, as Figure 4.7.3 below shows.

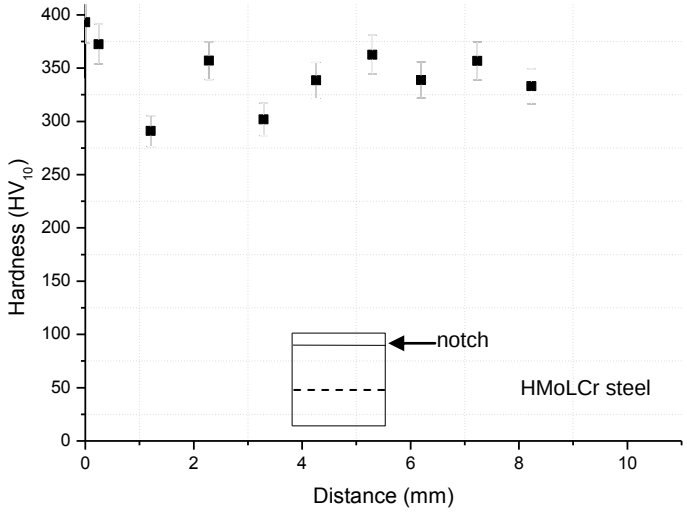

(a)

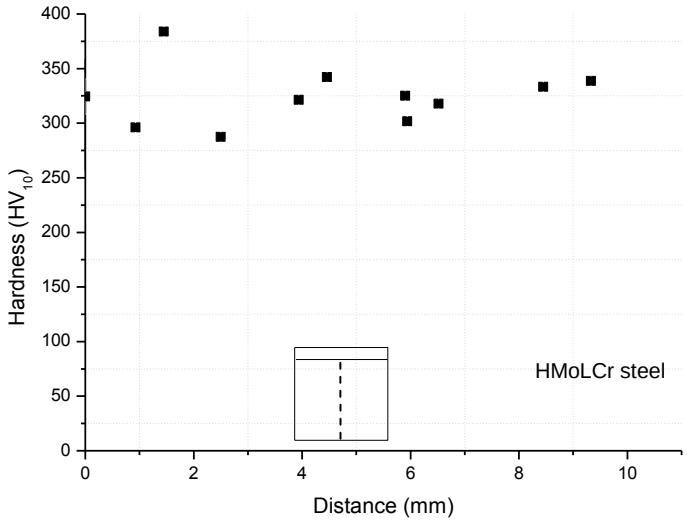

(b)

Figure 4.7.3 Hardness profiles in the HMoLCr steel across a Charpy sample taken (a) parallel to the Charpy V-notch and (b) transverse to the notch.

4.7.1.3 Distribution of bainite in martensite

The heat treatment of the Charpy samples was conducted in a Gleeble 1500D™ thermomechanical simulator which heats samples by direct electric current. The thermal

UNIVERSITEIT VAN PRETORIA
UNIVERSITY OF PRETORIA
YUNIBESITHI YA PRETORIA

cycles used to obtain the various amounts of bainite in the Charpy samples were based on measurements from a Bähr dilatometer which uses induction heating, where the small sample size of 5 mm diameter enables the thermal cycle to be followed or adhered to with a high degree of response precision. During direct electrical heating of the Charpy samples where the electric current tends to concentrate more on the surface, the sample is heated from the surface inwards and a temperature gradient may result between the surface and the centre of the sample within the plane on which the thermocouple is attached. The thermal gradient may be tolerable for some purposes, however for the purpose of this experimental work where the amount of bainite transformed had strict time-temperature dependence, it was important to understand the effects of any likely thermal gradient. This would ensure that a homogeneous distribution of bainite in martensite in the plane below the Charpy groove is achieved. To obtain some idea of the distribution of these phases, the hardness profiles were taken across a Charpy specimen of the steel HMoLCr in which 50% bainite had been formed. The hardness profiles were taken along orthogonal, intersecting paths and the results are shown in Figure 4.7.4.

Some periodic scatter was observed, which was expected from hardness indentations on the softer bainite which would give lower readings and higher readings on the harder martensite. Apart from the scatter, no definite trend was observed. It was concluded that the bainite was reasonably evenly distributed in the martensitic matrix.

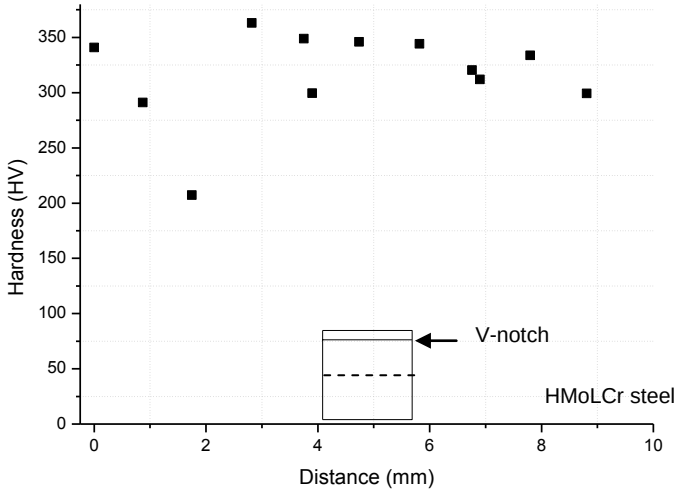

UNIVERSITEIT VAN PRETORIA
UNIVERSITY OF PRETORIA
YUNIBESITHI YA PRETORIA

(a)

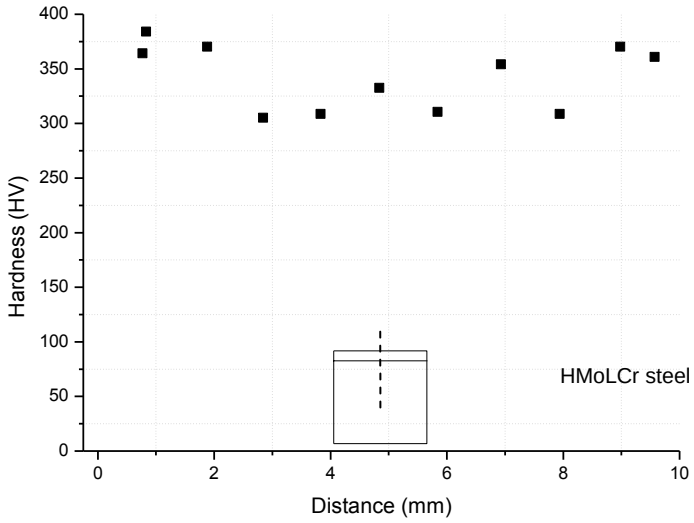

(b)

Figure 4.7.4 Hardness profiles measured (a) parallel to the Charpy V-notch and (b) transverse to the V-notch across a HMoLCr steel Charpy specimen heat treated to form 50% upper bainite.

4.7.1.4 Temperature gradients

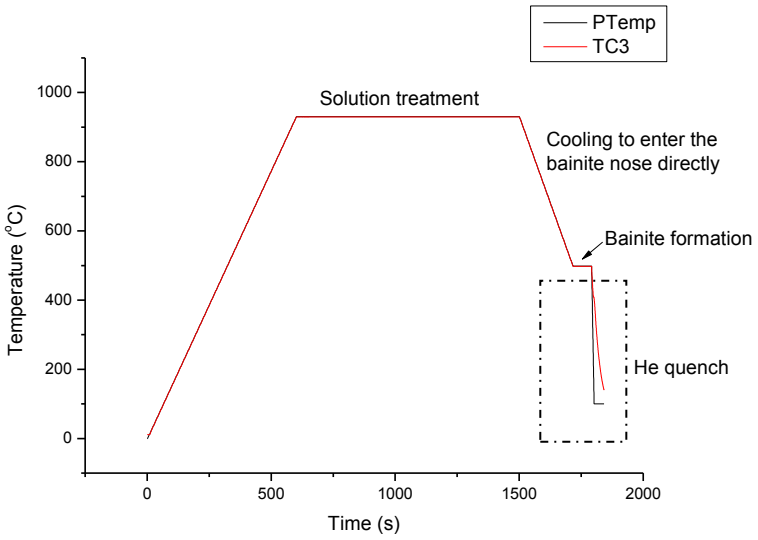

(a)

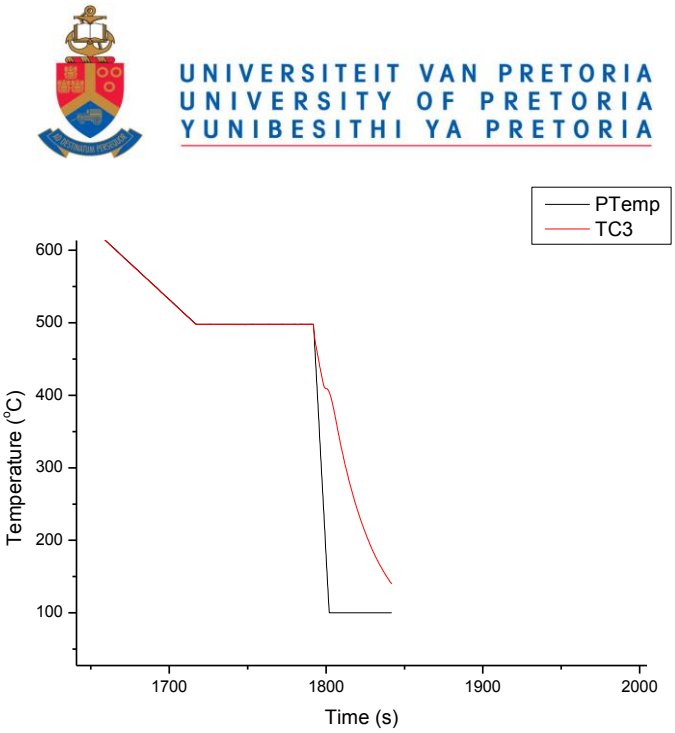

(b)

Figure 4.7.5 (a) Time-Temperature profile on Gleeble of the heat treatment to produce bainite (b) a magnified view of the quenching process. PTemp is the programme temperature and TC3 the control temperature.

Figure 4.7.5 (a) shows the time – temperature profile used on the Charpy samples. There was a discrepancy between the temperature of the thermocouple to which the sample was welded (TC3) and the program temperature (PTemp) but only during the final quench. A magnified section of the He quench is shown in Figure 4.7.5 (b) which shows that the final quench temperature of 150℃ was reached at an average cooling rate of about 9℃/s. Since the M_s temperatures are significantly higher than the quench temperature, it can be ascertained that the martensite volume fraction attained was within the expected range.

4.7.2 Effect of the amount of bainite on the impact energy

The total Charpy impact energy was plotted as a function of the amount of bainite in Figure 4.7.6.

UNIVERSITEIT VAN PRETORIA
UNIVERSITY OF PRETORIA
YUNIBESITHI YA PRETORIA

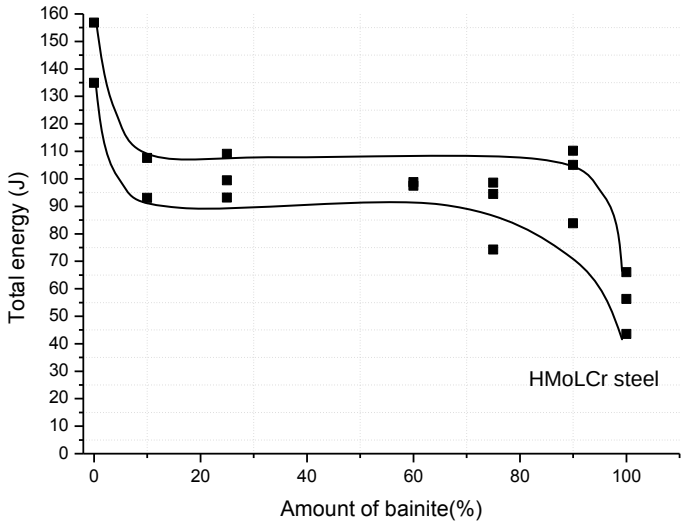

(a)

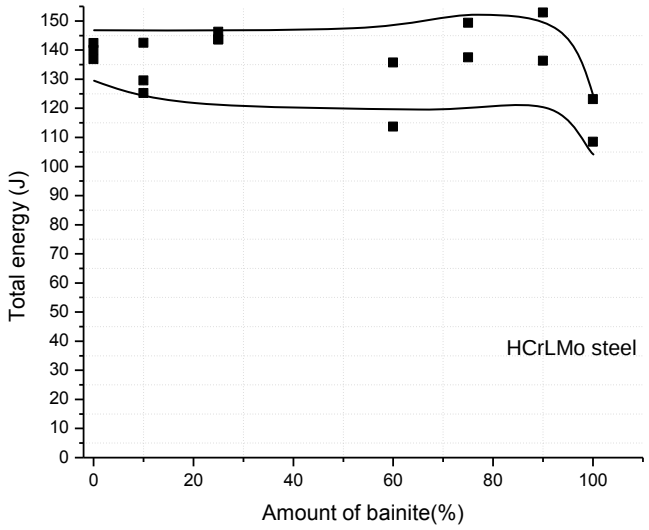

(b)

Figure 4.7.6 Graphs of the total energy absorbed as a function of the amount of bainite in the Charpy samples of (a) steel HMoLCr and (b) steel HCrLMo.

The trend from Figure 4.7.6 (a) for the HMoLCr steel shows that the total absorbed impact energy already decreased when only 10% bainite was present in the microstructure but there

UNIVERSITEIT VAN PRETORIA
UNIVERSITY OF PRETORIA
YUNIBESITHI YA PRETORIA

after in the range of 10 - 80% bainite, the impact energy seems to level out until a second decrease is found at 100% bainite.

The HCrLMo steel, on the other hand, showed no significant variation in the absorbed energy throughout the entire range of mixed structures, although the fully bainitic samples had the lowest total absorbed energy.

4.7.3 Crack initiation and propagation energies

The total energy absorbed in an impact fracture consists of the energy required to initiate a crack and the energy to propagate the crack. From the instrumented Charpy impact data the initiation and propagation energies were obtained from the individual load-deflection curves as typically shown in Figure 4.7.7.

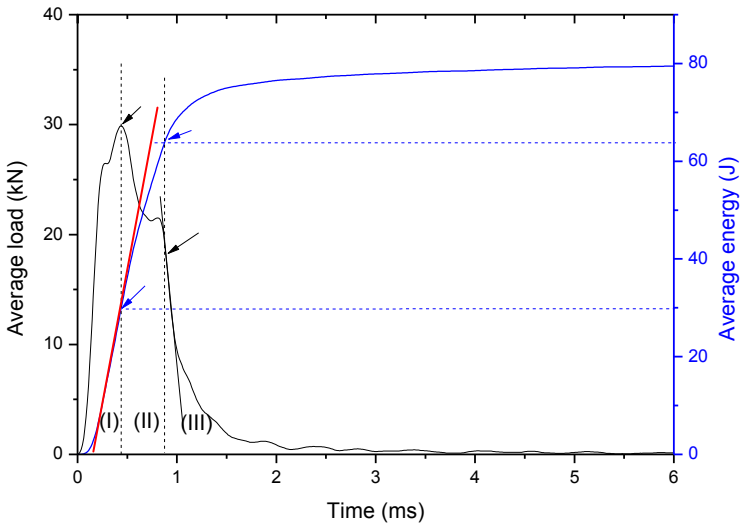

Figure 4.7.7 Graphical output from instrumented impact tests showing different regions of fracture on load and energy curves plotted as a function of time.Taken from a HMoLCr steel sample with 50% bainite.

The arrows on the peak load and the corresponding energy are indicative of the energy expenditure in initiating a crack, since beyond this point, a decrease in load occurs as the energy is dissipated in crack movement. The regions (I), (II) and (III), are demarcated by the two vertical lines. The load sustained up to the intersection of the first vertical line

UNIVERSITEIT VAN PRETORIA
UNIVERSITY OF PRETORIA
YUNIBESITHI YA PRETORIA

demarcates region (I). This load is the maximum sustainable load before plastic deformation begins at the root of the notch. Region (I) is therefore the area under the load-time curve representing the crack initiation energy. Plastic deformation at the notch root mentioned above is represented in region (II). The area under the remaining part of the curve, region (III), is the energy expended on rapid crack growth where the unstable crack propagation begins at the point where the load markedly drops. The energy given by regions (II) and (III) are collectively taken as representing the crack propagation energy for each sample, which includes both ductile and brittle crack growth. Note that the maximum rate of energy absorption during the impact test occurs in regions (I) and (II).The regions of the Charpy sample that can be associated with crack initiation and propagation fracture regions are shown in Figure 4.7.8 below for the steel HCrLMo.

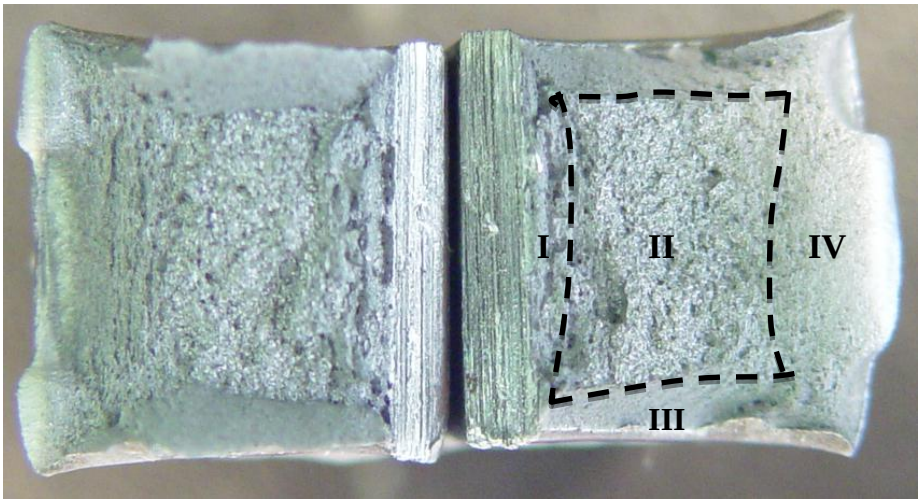

Figure 4.7.8 Characterisation of Charpy fracture surface in a HMoLCr steel sample consisting of 75% bainite. I is the fracture initiation region, II is the britte propagation region, III is a shear lip and IV is the final fracture.

The morphology of the fracture initiation region I is plastic deformation characterised by ductile tearing. The initiation region is formed by shearing along slip lines. It is followed immediately by ductile crack propagation. At the rapid load drop, brittle fracture begins and is visible as the relatively flat central region on a fracture surface.

UNIVERSITEIT VAN PRETORIA
UNIVERSITY OF PRETORIA
YUNIBESITHI YA PRETORIA

4.7.3.1 The HMoLCr steel

Following the method to find the crack initiation energy in Figure 4.7.7 the graphs of crack initiation and propagation energy were plotted as a function of % bainite and are shown in Figure 4.7.9 for the HMoLCr steel.

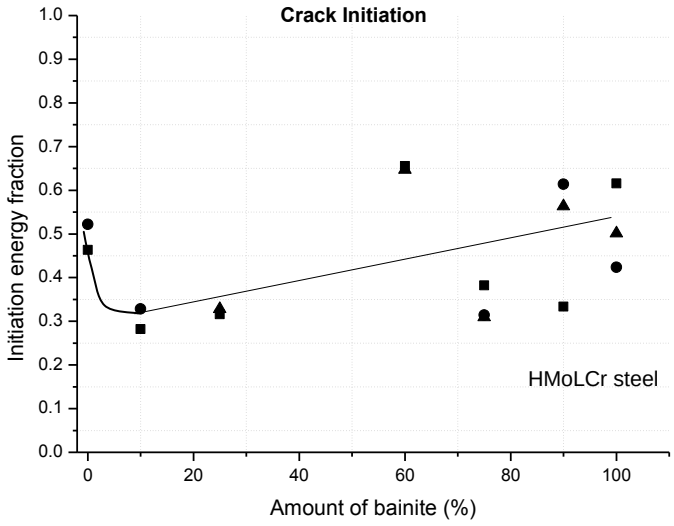

(a)

UNIVERSITEIT VAN PRETORIA
UNIVERSITY OF PRETORIA
YUNIBESITHI YA PRETORIA

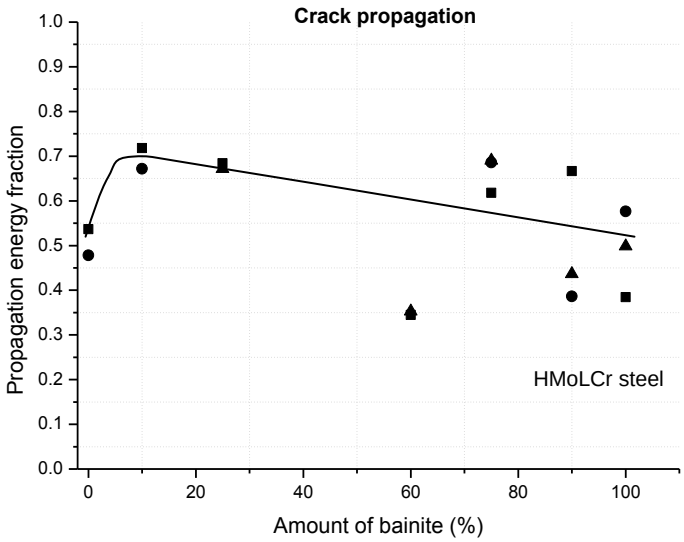

(b)

Figure 4.7.9 Plots of (a) crack initiation and (b) crack propagation energies in the HMoLCr steel Charpy samples. The respective energies were measured as a fraction of the total energy.

The crack initiation energy graph in Figure 4.7.9 shows a significant drop in crack initiation energy between 100% martensite specimens and 10% bainite specimens. The decrease is to less than 0.5 of the total absorbed energy and precedes an increase in crack initiation energy as the amount of bainite increases. It is evident that the effect of low volume fractions of bainite in the HMoLCr steel is to increase its susceptibility to brittle cracking as little energy is required to initiate a crack. This finding is the reason for the decrease in total absorbed energy in Figure 4.7.6 between 0% bainite (or 100% martensite) and 10% bainite.

The crack propagation energy decreased with an increase in the amount of bainite. This is a result of an increase in the amount of the brittle carbide phase. The images in Figure 4.7.10 show the fracture surfaces of samples containing various amounts of bainite.

UNIVERSITEIT VAN PRETORIA
UNIVERSITY OF PRETORIA
YUNIBESITHI YA PRETORIA

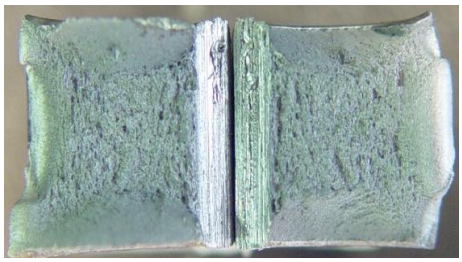

(a) 100%M

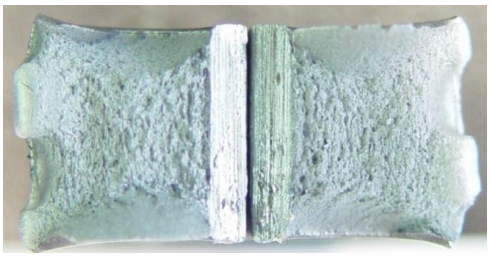

(b) 10% B

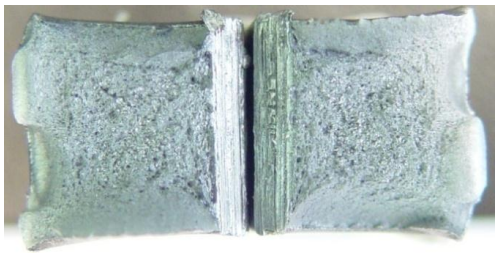

(c) 25%B

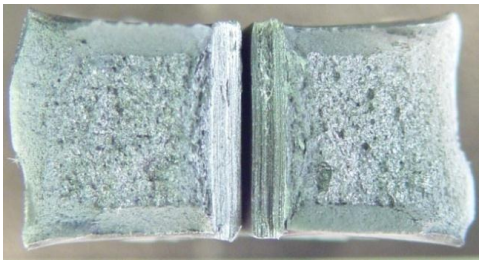

(d) 90%B

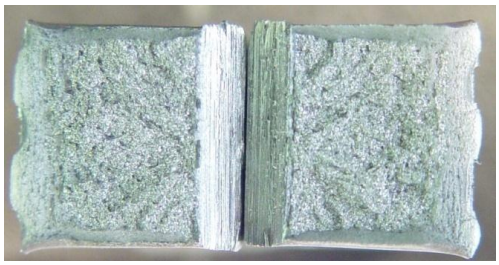

(e) 100%B

Figure 4.7.10 Optical images of fracture surfaces of HMoLCr samples containing (a) 100% M, (b) 10% B, (c) 25% B, (d) 90% B and (e) 100% B. M = martensite and B = bainite Note the reduced ductile appearance from 10 to 100% bainite.

It can be seen from the optical images of the fracture surfaces, that there is a marked transition from predominantly ductile fracture at the 10% B sample surface to a largely brittle fracture surface at 100%B. This is consistent with the decreasing crack propagation energy with increasing amounts of bainite.

The total absorbed energy plot shows a horizontal midsection between 10% and 80% bainite. Consider the crack initiation energy fraction plot in Figure 4.7.9 where the energy fractions of the 10%, 25% and 75% bainite specimens are all roughly 0.3. Because of the relation of the total absorbed energy to the crack initiation and propagation energies described earlier, the

UNIVERSITEIT VAN PRETORIA
UNIVERSITY OF PRETORIA
YUNIBESITHI YA PRETORIA

corresponding crack propagation energy fraction for these specimens are all approximately 0.7. This consistency resulted in the plateau of the total absorbed energy.

4.7.3.2 The HCrLMo steel

The samples from the HCrLMo steel, on the other hand, had the highest crack initiation energies in the microstructures containing small amounts of bainite and a trend in crack propagation energy that increased with increasing amounts of bainite. Figure 4.7.11 shows the respective initiation and propagation energies for the HCrLMo steel samples.

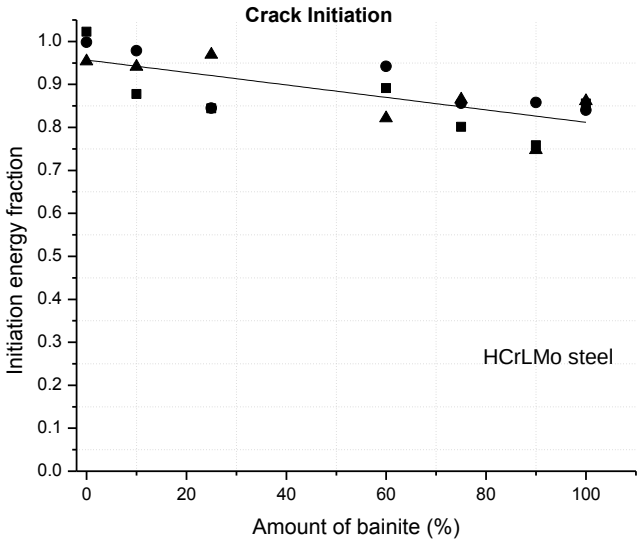

(a)

UNIVERSITEIT VAN PRETORIA
UNIVERSITY OF PRETORIA
YUNIBESITHI YA PRETORIA

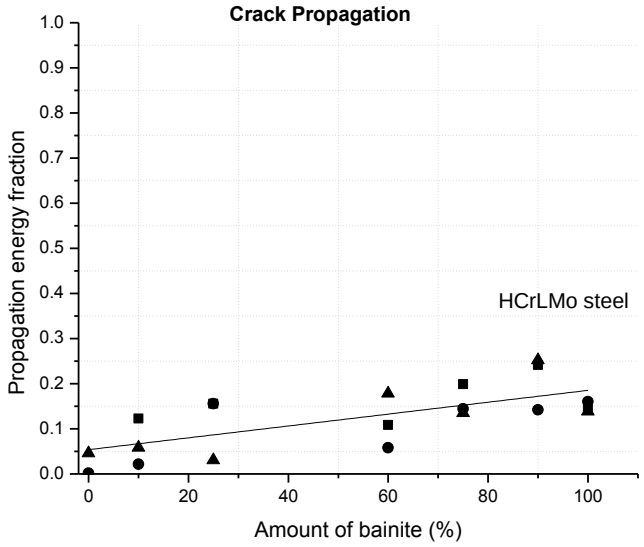

(b)

Figure 4.7.11 Plots of the fractions of (a) the crack initiation energy and (b) the crack propagation energy of the HCrLMo steel.

The crack initiation energies in the HCrLMo contribute a significant amount to the total absorbed energy as they lie within 95 to 75% of the total energy. This means that a large amount of ductility predominates the HCrLMo specimens and corresponds with the high amounts of total absorbed energy shown in Figure 4.7.6.

4.7.4 Fractography of the Charpy fracture surfaces

The SEM micrographs in Figure 4.7.12 below were taken within the crack initiation region at the ductile/plastic deformation zones where shear fracture produced elongated dimples.

The density of dimples present on a fracture surface is a function of the number of nucleation sites available. Ductile dimples occur by a microvoid coalescence mechanism and are nucleated at any point of strain discontinuity such as at inclusions, which is evident in the inclusions found in many dimples. Other possible points of nucleation are grain or subgrain boundaries and second phase particles.

UNIVERSITEIT VAN PRETORIA
UNIVERSITY OF PRETORIA
YUNIBESITHI YA PRETORIA

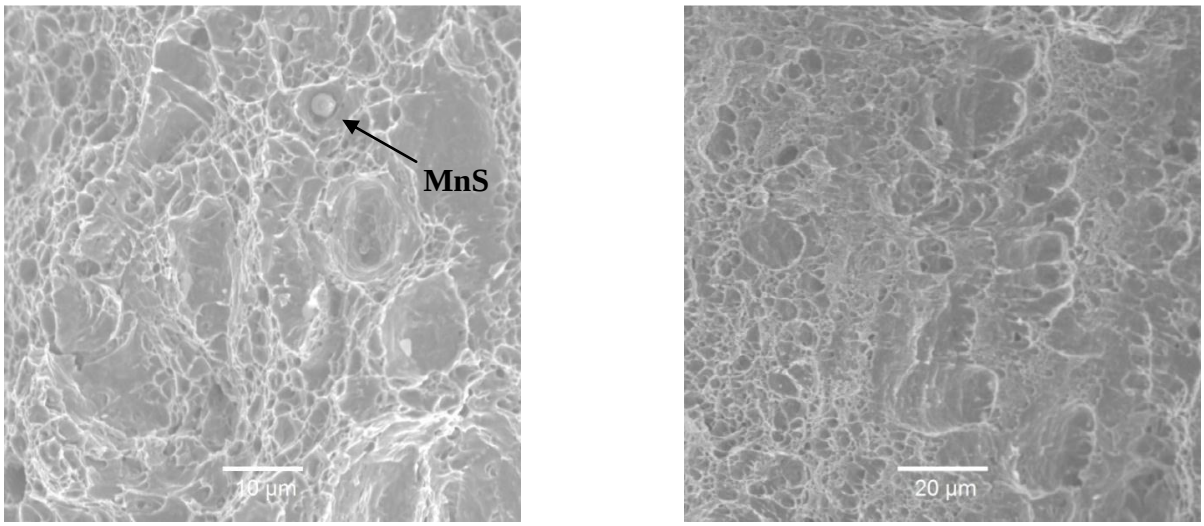

(a) (b)

Figure 4.7.12 SEM micrographs of the fracture initiation region in (a) a HCrLMo steel Charpy sample with 75% bainite and (b) in a HMoLCr steel Charpy sample with 10% bainite. Note the particles within ductile dimples, most likely MnS inclusions.

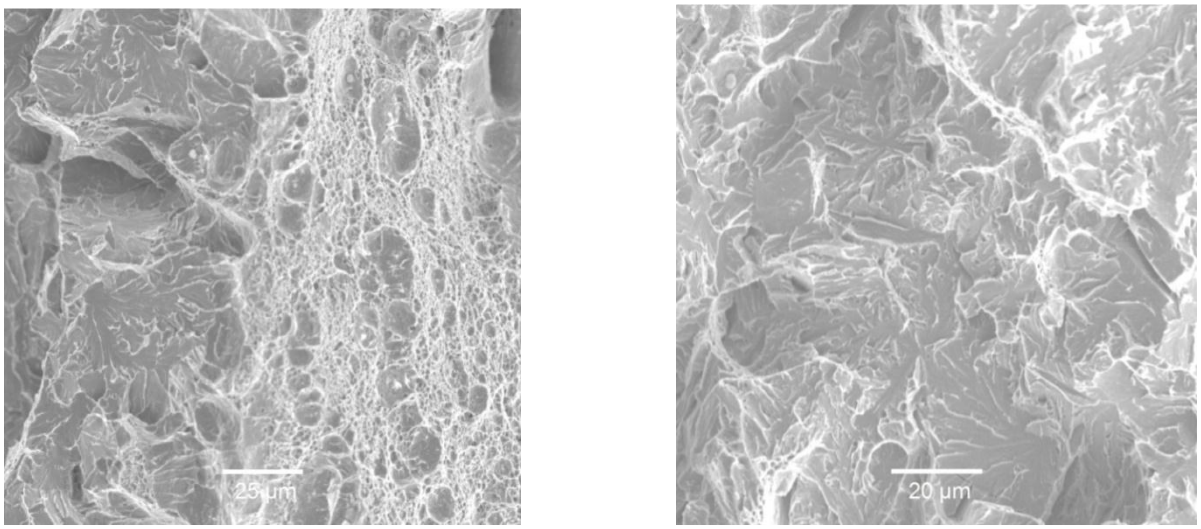

(a) (b)

Figure 4.7.13 SEM micrograph taken in a HMoLCr steel Charpy sample containing10% bainite at (a) the transition region between crack initiation and brittle fracture region (b) a region of brittle fracture with numerous cleavage facets.

The mode of fracture changed from ductile fracture in the crack initiation region to brittle fracture in the rapid crack propagation region. Cleavage facets were found in these brittle crack propagation regions.

UNIVERSITEIT VAN PRETORIA
UNIVERSITY OF PRETORIA
YUNIBESITHI YA PRETORIA

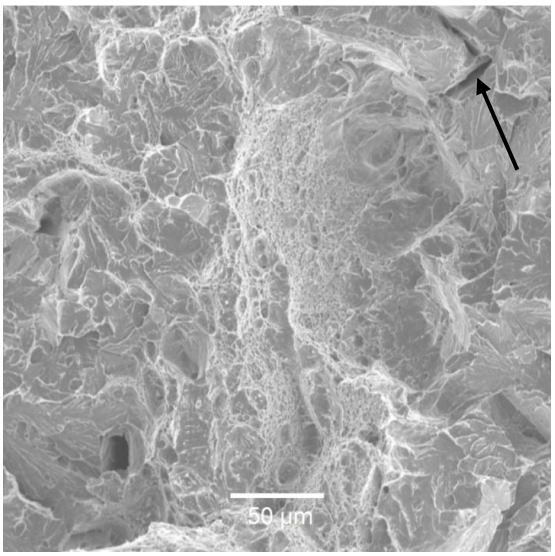

Figure 4.7.14. SEM micrograph of tear ridges within the brittle fracture region of a HCrLMo steel Charpy sample with 75% bainite. Note the secondary cracks (arrowed) that developed amongst the cleavage facets.

Tear ridges were found within the brittle fracture region as shown in Figure 4.7.14. Tear ridging is a sign of local energy absorption during cleavage crack propagation. The connection of these cleavage facets by tear ridges is a dominant energy absorption mechanism during cleavage crack propagation [66]. The occurrence of localized features exhibiting both cleavage and plastic deformation is known as quasi-cleavage [67] and is said to be caused by tri-axial stress states, material embrittlement and or impact loading within the DBTT region. However, the occurrence of localised plastic deformation on a largely cleavage fractured surface is thought to be due to ductile tearing of regions that were not broken or opened by the cleavage crack path.

The occurrences of secondary cracks shown by the arrow in Figure 4.7.14 during crack propagation in the area of the main cleavage crack propagation indicate areas of local energy absorption.

4.7.5 Shear fracture measurements

The lateral expansion was measured as a function of the amount of bainite. Figure 4.7.15 shows the graphs of the lateral expansion of Charpy samples of the HCrLMo and HMoLCr steels.

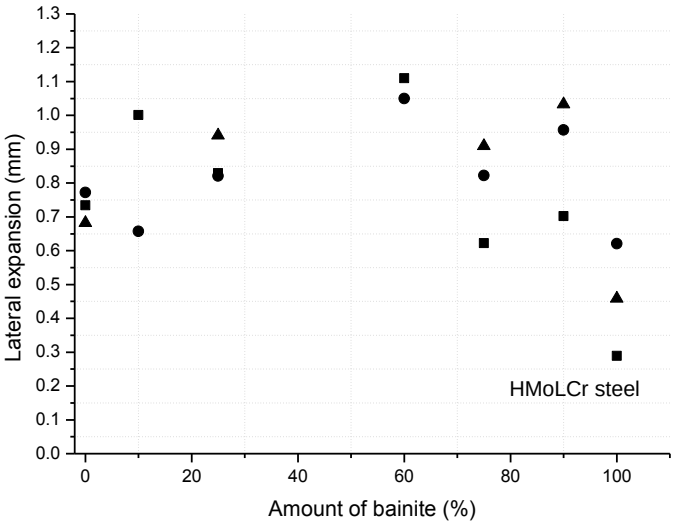

(a)

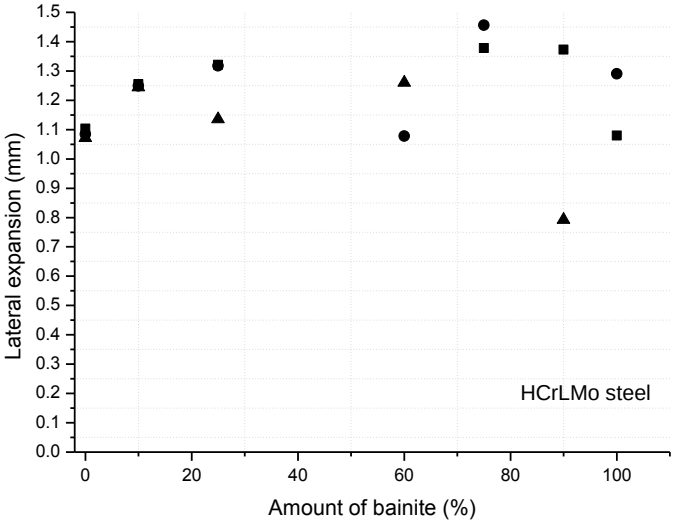

(b)

Figure 4.7.15 Lateral expansions measured on (a) the HMoLCr steel Charpy samples and (b) on the HCrLMo Charpy samples.

The HCrLMo steel showed an increase in the lateral expansion at 10% bainite, indicating an increased amount of ductile deformation and thereafter remained approximately constant.

UNIVERSITEIT VAN PRETORIA
UNIVERSITY OF PRETORIA
YUNIBESITHI YA PRETORIA

The HMoLCr steel's lateral expansion also increased up to 50% bainite but thereafter decreased to its lowest value at 100% bainite.

The amount of ductile fracture was estimated from digital images of the fracture surfaces. The shear fracture was distinguished from the brittle fracture region by the large flat area in the centre of the specimen. The amount of shear fracture was calculated as a fraction of the total fracture area. Figure 4.7.16 shows the graphs of shear fracture measured on Charpy samples of the two steels.

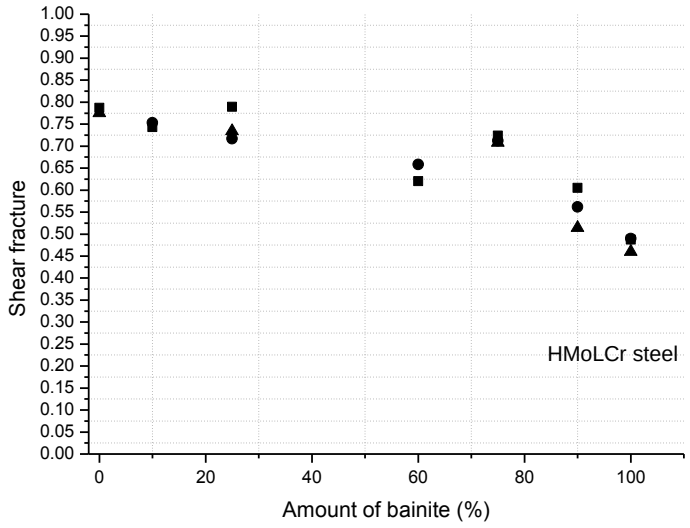

(a)

UNIVERSITEIT VAN PRETORIA
UNIVERSITY OF PRETORIA
YUNIBESITHI YA PRETORIA

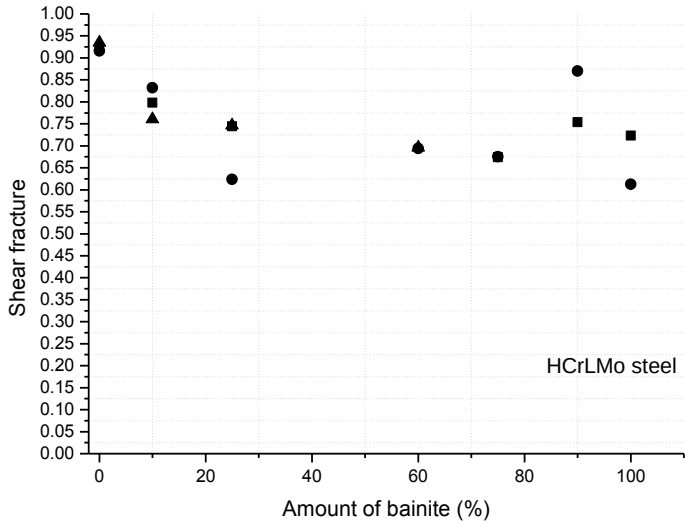

(b)

Figure 4.7.16 Shear fracture measured on fractured Charpy samples of (a) the HMoLCr and (b) HCrLMo steels as a function of the % bainite.

The shear fracture plot of steel HMoLCr confirms the decrease in ductility with increasing amounts of bainite that is evident in the lateral expansion plot. In steel HCrLMo, the shear fracture decreased up to 25% bainite and remained fairly constant thereafter. According to the shear fracture plot, therefore, smaller amounts of bainite are more critical to the toughness of tempered martensite in the HCrLMo steel if compared to larger amounts of bainite.

UNIVERSITEIT VAN PRETORIA
UNIVERSITY OF PRETORIA
YUNIBESITHI YA PRETORIA

5 Chapter 5: Discussion

In this chapter, the effect of Cr and Mo on the bainite transformation is discussed by examining the impact of these elements on hardenability, the growth rate and on the M_s temperatures. Finally, the impact energy of martensite-bainite Charpy samples is examined together with the effect of various amounts of bainite on the crack initiation and crack propagation energies.

5.1 Tempering characteristics of the C-Mn and HCrLMo steels

Both the C-Mn and HCrLMo steels have relatively low carbon contents of 0.11wt% and 0.17wt% respectively and therefore their M_s temperatures (which are 441.1℃ for the C-Mn steel and 419.9℃ for the HCrLMo steel) are significantly above room temperature. It is expected that autotempering of the martensite may have occurred during quenching. Therefore, prior to tempering the steel specimens, the first stages of tempering of martensite had already occurred through autotempering. The carbon atoms segregated to dislocations and the matrix was relieved of strain. Decomposition of martensite to a less supersaturated martensite and ε-carbide occurs up to 200℃.

The hardness data in Figure 4.3.1 shows a hardness peak at 200℃ in the tempering curve of the HCrLMo steel. The peak in hardness is ascribed to the formation of coherent epsilon carbides that precipitate during tempering from the carbon-supersaturated martensite. According to Leslie et al the precipitation of epsilon carbides that produces a coherency peak is more pronounced in steels containing amounts of carbon in excess of 0.2wt% than in steels containing lower carbon contents [68]. This is consistent with the absence of a hardness peak in the C-Mn steel tempering curve, in which the carbon content was less than 0.2wt%.

It is known that the as-quenched hardness of martensite is dependent upon the carbon concentration in the martensite. This relationship is reflected in the as-quenched hardness values obtained which for the C-Mn steel was lower at 357.50HV compared to 443.2HV for the HCrLMo steel.

UNIVERSITEIT VAN PRETORIA
UNIVERSITY OF PRETORIA
YUNIBESITHI YA PRETORIA

The secondary hardening peaks from coherent carbides such as M_2X (in 12% Cr steels), Mo_2C and V_4C_3 [69] that are typical in steels with alloying elements Cr, V, Mo, were not observed in this study as the quantity of these alloying elements in the steels were present in too small concentrations.

UNIVERSITEIT VAN PRETORIA
UNIVERSITY OF PRETORIA
YUNIBESITHI YA PRETORIA

5.2 Effect of the steel compositions on the partial CCT diagrams

The partial Continuous Cooling Transformation diagrams which were obtained for the HCrLMo and HMoLCr steels consisted of only the bainite nose which was the area of interest. The absence of the ferrite nose in both CCT diagrams over the range of cooling rates used is attributed to the effect of boron. Boron segregates to austenite grain boundaries and reduces the grain boundary energy thus rendering the grain boundaries less effective as potential nucleation sites for ferrite. As little as 0.002wt% boron is typically sufficient to achieve this effect. The steels from which the CCT's in Figure 4.4.13 were constructed contain 0.0035 and 0.002wt% boron, both in sufficient quantities to achieve the hardenability effect illustrated in Figure 5.2.1 below.

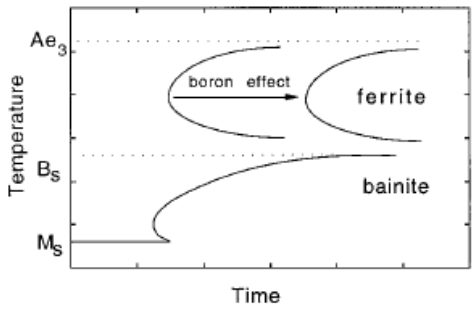

Figure 5.2.1 Effect of boron on transformation [27] .

In addition to the absence of the ferrite C-curve over the range of cooling rates used, the bainite C-curve was shifted to longer times in the HMoLCr steel. A useful measure of the position of the bainite C-curve with respect to time is the critical cooling rate for 100% martensite to form upon the initial quench. From the CCT diagrams in Figure 4.4.13 (a) and (b) the critical cooling rate for the formation of martensite from the initial quench was 30℃/s for the HCrLMo steel and only 5℃/s for the HMoLCr steel. Despite a higher level of Cr in the HCrLMo steel, the steel is significantly less hardenable than the HMoLCr steel.

UNIVERSITEIT VAN PRETORIA
UNIVERSITY OF PRETORIA
YUNIBESITHI YA PRETORIA

The effects of boron in combination with Cr or Mo was delineated in the work by Han et al [70] who found that Mo was more effective than Cr in enhancing the hardenability of boron added steels. The authors compared the hardenability of two low carbon steels of which one was a Mo-B steel (Fe-0.1C-1.5Mn-0.2Mo-0.002B) and the other a Cr-B steel (Fe-0.1C-1.5Mn-0.5Cr-0.002B) with a boron baseline steel of composition Fe-0.1C-1.5Mn-0.002B (in wt%). After cooling at various cooling rates, the fastest cooling rate during which pearlite and polygonal ferrite evolved was 3℃/s in the boron steel, 1℃/s in the Cr-B steel and 0.2℃/s in the Mo-B steel. It was thus demonstrated that Mo has a more substantial effect on hardenability than Cr [70]. Han and co-workers ascribed the hardenability effect of Mo to the deterioration of phase stability of $M_{23}(C,B)_6$ which reduces hardenability by providing nucleation sites for ferrite.

The Wagner Interaction coefficient ϵ_C^i was introduced as a measure of the strength of interaction of an alloying element i with carbon [41, 71] and is given by the expression $\epsilon_C^i = \frac{\partial ln f_C}{\partial x_C}$ where f_C is the activity coefficient for carbon which is given by the carbon activity a_C divided by the carbon concentration: $f_C = \frac{a_C}{[\%C]}$.

Aaronson , Reynolds and Purdy [41] found that more negative values of ϵ_C^i produced a pronounced solute drag effect [41]. In the work done by Wada, the Wagner interaction coefficient for carbon in Fe-C-Cr alloys with between 0.2 and 8wt% Cr, was found to be $\epsilon_C^{Cr} = -72$ [72] and in Fe-C-Mo alloys of Mo content between 0.2 and 3wt% Mo, the interaction coefficient was $\epsilon_C^{Mo} = -100$ [73], showing that Mo has a stronger effect than Cr.

Therefore, the suppression of a ferrite C-curve in the partial CCT diagrams of both the HCrLMo and HMoLCr steels in Figure 4.4.13 is attributed to the hardenability effect of Boron. However, the difference observed in the bainite C-curves is ascribed to the stronger effect of Mo by its synergistic effect in combination with Boron and its higher negative Wagner interaction coefficient.

UNIVERSITEIT VAN PRETORIA
UNIVERSITY OF PRETORIA
YUNIBESITHI YA PRETORIA

5.3 JMAK kinetics of the isothermal transformations

The Johnson Mehl Avrami Kolmogorov model was used to fit the volume fraction – time data. By taking the natural logarithm of the JMAK equation, the linear equation below is obtained:

$$lnln\left[\frac{1}{1-Vf}\right] = nlnt + \ln k \qquad \text{eq 5.1}$$

where V_f is the volume fraction and k is a temperature dependent constant.

The Avrami exponent n was then calculated from the slope of the graphs of $ln\ t$ against $lnln\left[\frac{1}{1-Vf}\right]$ in Figure 5.3.1.

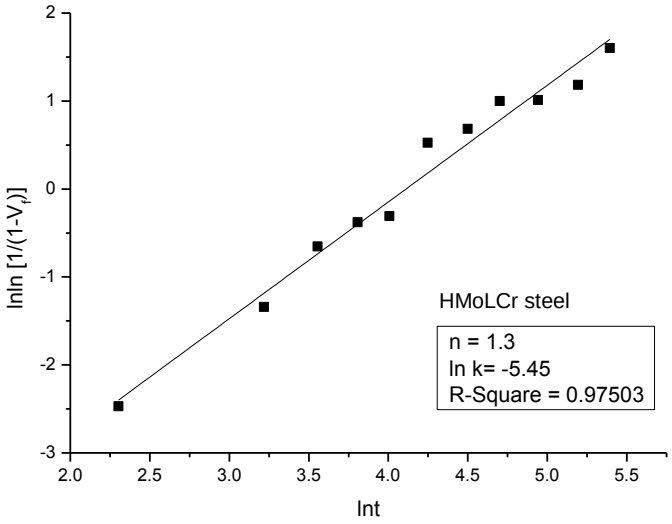

(a)

UNIVERSITEIT VAN PRETORIA
UNIVERSITY OF PRETORIA
YUNIBESITHI YA PRETORIA

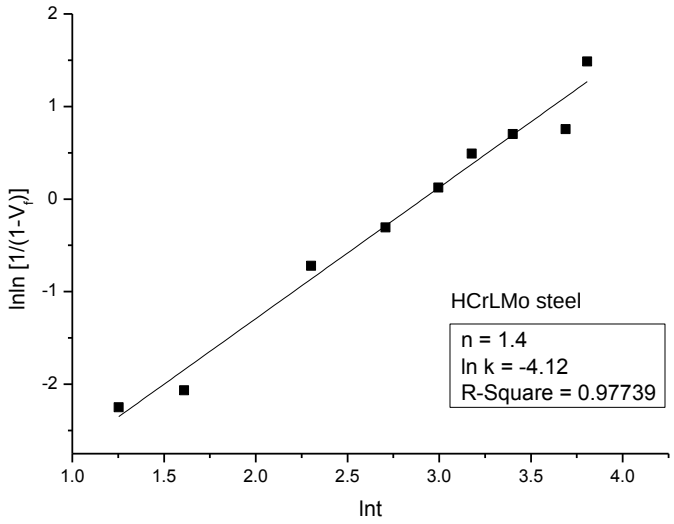

(b)

Figure 5.3.1 Plots of lnt versus lnln(1/1-V_f) for (a) the HMoLCr steel and (b) the HCrLMo steel isothermally transformed at 498℃ and 484℃ respectively.

The exponent n is, according to Christian [74] an indication of the dimensionality of the growth. Typically, an exponent of 2 represents constant nucleation and linear growth. Christian states that the general expression for volume transformed (equation 2.3) in the Avrami theory of nucleation at preferred sites is valid if $1 \leq n \leq 2$ which leads to one-dimensional growth and if $2 \leq n \leq 3$ leads to two-dimensional growth. One-dimensional growth in the case of bainite refers to the lengthening rate of ferrite laths. The thickening of bainitic ferrite laths is negligible and growth of the ferrite laths occurs mainly along the length of the lath. This has been demonstrated, for instance, in the work done by Kostic, Hawbolt and Brown [75] on volume diffusion controlled growth of bainite, which showed that the rate of lengthening of bainite plates occurred at least two orders of magnitudes higher than the rate of thickening of the plates. A typical aspect ratio of 4 was obtained for the bainite formed in this study. The exponents of 1.3 and 1.4 obtained for the HMoLCr and HCrLMo steels therefore indicate one dimensional growth.

UNIVERSITEIT VAN PRETORIA
UNIVERSITY OF PRETORIA
YUNIBESITHI YA PRETORIA

5.4 Effect of alloying elements on growth rates

The major question to be addressed here is that the rates of bainite formation during isothermal transformation shown in Figure 4.6.1 differed with the HCrLMo steel transforming significantly faster than the HMoLCr steel. Why does the addition of Mo in a relatively small amount to these plate steels have such a marked effect on the bainite formation if compared to Cr additions? Is this effect a thermodynamic or a kinetic one? As both steels were isothermally transformed at equivalent estimated undercoolings, the thermodynamic driving force for nucleation could be considered approximately equivalent.

The growth rate of bainite can be modelled according to the Trivedi model for diffusion controlled lengthening of plates in which the growth rate v is given by the equation [17, 75]:

$$v = \frac{2D}{\rho}\frac{9}{16\pi}\Omega_*^2 \qquad \text{eq 5.2}$$

where Ω_*^2 is the carbon supersaturation, D is the average carbon diffusivity and ρ the radius of the tip of the advancing interface.

The equation depicts a linear proportional relationship between the diffusivity of carbon and the growth velocity v. This implies that factors affecting the diffusivity of carbon consequently affect the growth rate directly.

The effect of various alloying elements on carbon diffusivity in austenite has been studied by several researchers [73, 76-78]. It is well documented that the diffusivity of carbon in an alloy steel is a function of its chemical composition. For instance manganese and chromium tend to decrease the carbon diffusivity while carbon and nickel increase it [71]. It is thought that elements which reduce the carbon activity such as Cr and Ni, attract C atoms, slowing them down whilst elements that increase carbon activity do so by repelling C atoms. The lowering of carbon activity and consequently diffusivity and mobility usually occurs where carbide-forming elements are present. Čermák et al put forward the relationship between the carbon tracer diffusivity and the carbon activity coefficient [76].

$$D = D(0)\left(\frac{\gamma}{\gamma^0}\right)^m \qquad \text{eq 5.4}$$

UNIVERSITEIT VAN PRETORIA
UNIVERSITY OF PRETORIA
YUNIBESITHI YA PRETORIA

where D(0) is the diffusion coefficient in the unalloyed metal, γ is the carbon activity coefficient in an alloyed metal and γ^{o} is the carbon activity coefficient in unalloyed steel. From equation 5.4 it is evident that as $\gamma \rightarrow \gamma^{o}$, D ~ D(0). The relationship was tested by measuring the diffusivity of carbon in Fe-Ni-Cr alloys [76]. The carbon diffusion coefficient was found to increase as γ approached γ^{o}. This held for temperatures ranging from 570℃ to 850℃. Diffusivity is related to carbon activity and chemical potential and it has been shown that the effect of Mo and Cr is to decrease the thermodynamic activity of carbon in austenite [79].

Based on the equation for carbon diffusivity (eq 5.5) in binary Fe-C alloys introduced by Ågren [80]; Seok-Jae Lee et al [78] derived an equation for the activity coefficient of carbon in austenite (eq 5.6).

$$D_C\left(\frac{cm^2}{s}\right) = 4.53\ x\ 10^{-3}\left(1 + y_C(1 - y_C)\frac{8339.9}{T}\right) x \exp\left(-\left(\frac{1}{T} - 2.221x10^{-4}\right)(17767 - 26436y_C)\right) \quad \text{eq 5.5}$$

The equation expresses the activity coefficient f_C in a multi-component alloy as a function of the absolute temperature and a concentration parameter unique to each alloying element.

$$logf_C^{Fe-C-M} = \frac{2300}{T} - 0.92 + \left(\frac{3860+10000y_{Si}}{T}\right)y_C - \left(\frac{2200}{T}\right)y_{Mn} + \left(\frac{3200}{T} + 2.1\right)y_{Si} + \left(\frac{2000}{T} + 0.30\right)y_{Ni} - \left(\frac{9500}{T} - 3.05\right)y_{Cr} - \left(\frac{9500}{T} - 2.5\right)y_{Mo} - \left(\frac{10700}{T}\right)y_V \quad \text{eq 5.6}$$

In a separate experiment to verify carbon diffusivity at temperatures in the range 500℃ to 900℃ [81] the authors found good correlation between their experimental data at the lower temperature of 500℃ with the expression proposed by Ågren. They concluded that the latter can thus be used in the temperature range 500℃ to 900℃. On this basis, the use of equation 5.6 in the upper bainitic temperature range is qualified. From this equation it can be seen that at equivalent Cr and Mo amounts $y_{Cr} = y_{Mo}$ and at the same temperature, Mo reduces the activity coefficient of carbon slightly more than Cr.

UNIVERSITEIT VAN PRETORIA
UNIVERSITY OF PRETORIA
YUNIBESITHI YA PRETORIA

To verify the activity of carbon in the HCrLMo and HMoLCr steels during isothermal conditions, the thermodynamic activities were simulated by Thermo-Calc software with data from the TCFE7 database. The activities of carbon in fcc austenite and bcc ferrite in the HMoLCr steel at 498℃ were found to be 0.21 and 3.41 respectively. The activity of an element is related to the chemical potential μ_i through the expression $\mu_i = \mu_i^* + RTlna_i$ where μ_i^* is the chemical potential of component i in the standard state, which for carbon is graphite. Using this expression, the difference in chemical potential between austenite and ferrite in the HMoLCr steel calculated at the transformation temperature of 771K is -18368.76 J/mol. In the HCrLMo steel, the activities of carbon in fcc austenite and bcc ferrite at 484℃ were 0.20 and 3.70 respectively and the difference in chemical potential at the transformation temperature of 757K is -17825.56J/mol. The chemical potential of carbon in the HMoLCr steel thus is lower than in the HCrLMo steel, implying the presence of a reduced chemical potential gradient in the HMoLCr steel. The implication of a lower chemical potential on the transformation may be considered according to Christian's [71] treatment of diffusional transformations. The diffusion current or flux of a species i as related to its chemical potential is given by: $I_i = -c_i M_i \nabla \mu_i$ where μ_i is the chemical potential, M_i is the mobility and c_i is the density of atoms. The lower chemical potential gradient in steel HMoLCr causes a reduction in the thermodynamic driving force to form upper bainite from austenite, which is in agreement with the experimental findings of a much reduced growth rate in the HMoLCr steel.

It has been shown that Mo reduces the carbon diffusivity [70]. As carbon diffusion is central to the formation of bainite, a reduction in the rate of carbon diffusion will retard the growth of the bainite. The diffusivities of carbon in the HCrLMo and HMoLCr steels as estimated by Dictra were found to be of the same order of magnitude and did not differ significantly between the two steels. It therefore seems that the observed greater retarding effect of Mo on upper bainite formation may not necessarily be carbon diffusion related if compared to that of the higher Cr steel.

However, given that the undercoolings are equivalent, another variable that is likely to affect the growth rates of the two steels is the nature of the substitutional alloying elements present. Solute drag models assume solute accumulation at growth interfaces and short range

UNIVERSITEIT VAN PRETORIA
UNIVERSITY OF PRETORIA
YUNIBESITHI YA PRETORIA

diffusion of these solute atoms as they move with the interface. Substitutional solute atoms can therefore cause a delay in the growth kinetics of the reaction. In the light of such a model, substitutional atoms can be said to slow down or retard growth if they participate in the growth of either bainitic ferrite or cementite. In verifying the involvement of substitutional atoms, the chemical composition of iron carbides extracted from upper bainite samples by electrolytic means were analysed and Mo and Cr peaks were observed in the spectra of numerous carbide particles. As these are strong carbide formers, the results suggest that the cementite in the upper bainite in these steels was alloyed iron carbide M_3C rather than iron carbide Fe_3C. The diffusivity of Cr and Mo in ferrite in the HCrLMo and HMoLCr steels at the respective transformation temperatures was predicted to be of the order 10^{-22} m^2/s and 10^{-23} m^2/s in the respective steels. These values are many orders of magnitude lower than the carbon diffusivities. It can therefore be speculated that the formation of alloy carbides rather than pure cementite in bainite slows the growth rate of bainite in both alloys by the involvement of alloying atoms because of the significantly lower diffusion rate for the substitutional alloying elements than for carbon. It can also be seen that the slower diffusivity of Mo (10^{-23} m^2/s) during the formation of M_3C is a likely cause of the low growth rates.

However, according to equation 5.2 it is not only diffusion that affects the growth rate but also the radius of the advancing interface. Figures 5.6.3 and 5.6.4 show the microstructures of the steels. The bainite laths in the steel HCrLMo were smaller or narrower than the laths in steel HMoLCr where widening or merging of the laths had occurred. The difference in lath size suggests that the radii of the tip of the advancing interface ρ was also a variable contributing to the difference in growth rate. By virtue of the inverse relationship between υ and ρ, thicker bainite laths in steel HMoLCr imply a slower growth rate than the thinner bainite laths in steel HCrLMo.

The difference in carbon activity obtained for the two steels implied that a lower chemical potential gradient at the growth front in the HMoLCr steel could have caused slower bainite growth. Furthermore, the observed participation of Cr and Mo in the formation of bainitic carbide may also have been a rate limiting factor and it is likely that a solute drag like effect, which accounts for the involvement of alloying elements, was operative during the growth of bainite in the HMoLCr steel.

UNIVERSITEIT VAN PRETORIA
UNIVERSITY OF PRETORIA
YUNIBESITHI YA PRETORIA

5.5 Effect of isothermal holding on M_s temperatures

The M_s temperature of the remaining austenite after bainite formation was found to decrease when measured as a function of the isothermal holding time in Figure 4.6.2. Since the M_s temperature is sensitive to the amount of carbon in the austenite from which it forms, its decrease with longer holding times indicates that some carbon enrichment occurs in the remaining austenite after bainite has formed. The carbon enrichment of austenite from bainite has been used in quench and partitioned (Q&P) steels where carbide-free bainite is preferred. The steels of which the M_s temperatures in Figure 4.6.2 were measured, contain alloyed cementite as is the case when upper bainite forms. Although the formation of cementite in the upper bainite consumed some of the carbon, the decreasing M_s testifies to a non-negligible carbon enrichment in the remaining austenite. The possible carbon content in the austenite was calculated at each M_s temperature according to the equation [38]:

$$M_s = 561 - 474C - 33Mn - 17Cr - 17Ni - 21Mo \qquad \text{eq 5.7}$$

The experimental M_s temperatures are plotted in Figure 5.5.1 as a function of the carbon content.

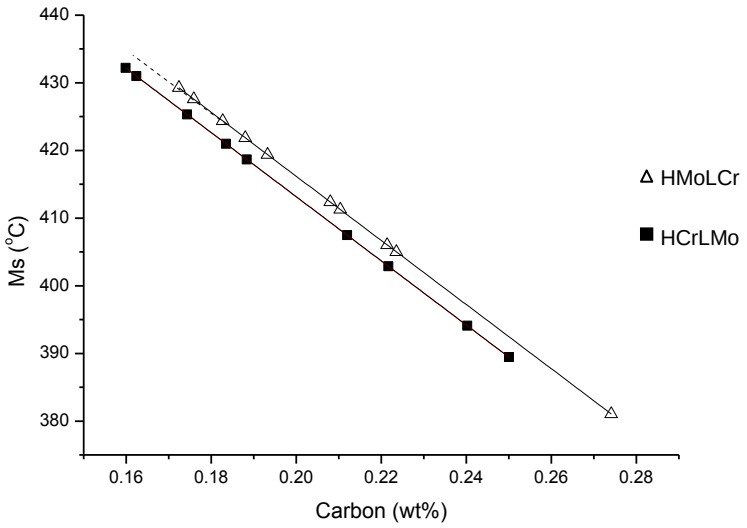

UNIVERSITEIT VAN PRETORIA
UNIVERSITY OF PRETORIA
YUNIBESITHI YA PRETORIA

Figure 5.5.1 Graph of the measured M_s depression with carbon content as modelled according to the equation by Krauss [38].

The implication of the carbon enrichment predicted in Figure 5.5.1 as derived from equation 5.7, is that the austenite that forms martensite is more enriched in carbon with the progressive formation of bainite. It follows that the martensite thus formed should be harder, yet hardness tests on samples did not reveal an increase in as-quenched hardness. When plotted as a function of time as in Figure 4.6.2 the M_s – time curves correspond with the volume fraction – time sigmoidal curves in Figure 4.6.1. The HCrLMo steel which grows at a higher rate than the HMoLCr steel also has a higher M_s – time gradient. However, the M_s plotted as a function of the amount of bainite for the two steels shows no significant difference in the two steels.

Furthermore, the question arises whether the estimated carbon concentrations in the untransformed austenite in Figure 5.5.1 as the percentage bainite increases, are realistic? The T_o curves for the steels were modelled using Thermo-Calc and are shown in Figure 5.5.2 below. The plots show that the carbon enrichments predicted in Figure 5.5.1 are well below the T_o carbon concentrations (w_{To}). The plots also show that the T_o temperature for bainite is ~727℃ in steel HMoLCr and ~717℃ in steel HCrLMo and therefore the undercoolings below the T_o at the isothermal transformation temperatures used were 229℃ and 233℃ respectively which are practically the same. This supports the earlier objective that the driving forces for bainite formation in both steels were practically the same in the selection of the two respective transformation temperatures.

UNIVERSITEIT VAN PRETORIA
UNIVERSITY OF PRETORIA
YUNIBESITHI YA PRETORIA

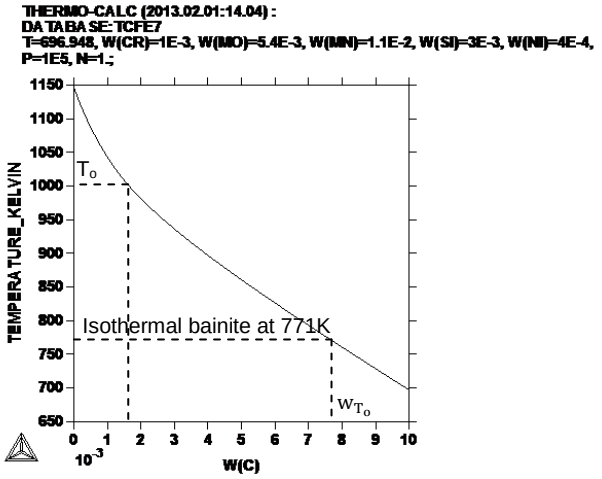

(a)

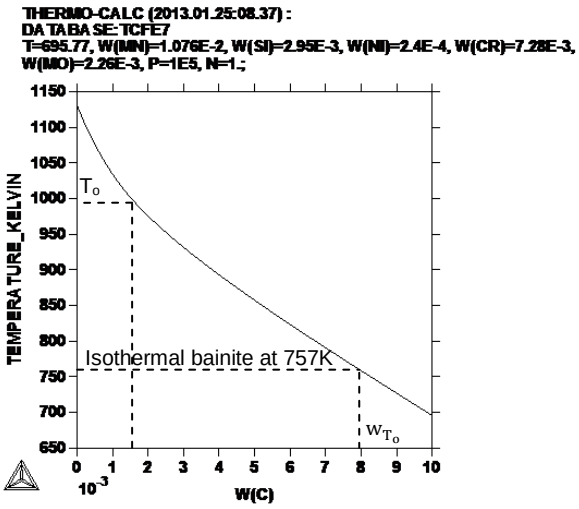

(b)

Figure 5.5.2 T-zero temperature plotted against carbon content (weight fraction) for (a) steel HMoLCr and (b) steel HCrLMo showing the T-zero temperatures T_o *and the maximum carbon content* w_{T_o} *at the isothermal treatment temperatures, as estimated by Thermocalc.*

UNIVERSITEIT VAN PRETORIA
UNIVERSITY OF PRETORIA
YUNIBESITHI YA PRETORIA

5.6 Impact toughness

5.6.1 Effect of bainite on the total absorbed energy

As Figure 4.7.6 shows, both steels had the lowest total absorbed energy in specimens with 100% bainite and it confirmed the effective brittleness of upper bainite in contrast to tempered martensite. However, the graphs did not show a consistent decrease in total absorbed energy with an increasing amount of bainite. The total energy in the figure for the HMoLCr steel initially decreased and reached a plateau between 10% and 80% bainite before a further decrease at more than 90 % bainite leading up to 100% bainite whilst the decreasing trend in the HCrLMo steel graph was of a more general nature with some considerable amount of scatter. In the mixed bainite/martensite samples a crack can initiate in either tempered martensite or bainite, and the distribution of bainite in the martensite matrix may have been the underlying reason for the scatter. This especially applies to the distribution of phases at the root of the notch. Studies on the fracture toughness of bainite-martensite steels showed that the overall toughness depends on the phase in which the cleavage fracture is first initiated. Some studies revealed that [82] cleavage will occur at a critical distance ahead of the precrack tip, in this case the V-notch. The occurrence of cleavage crack commencing in the bainite or martensite will depend on the probability of the occurrence of either phase at this critical distance. This implies that the impact energy of mixed bainite-martensite samples may approach the impact energy of 100% martensite or 100% bainite specimens where the energies of the latter are upper and lower bounds or limits. Consequently, the toughness of the mixed microstructures ought not be any higher than that of 100% martensite or lower than that of 100% bainite.

Overally, the mixed microstructures in the HCrLMo steel exhibited a greater degree of toughness as their absorbed energies were within a higher range if compared to that of the steel HMoLCr.

UNIVERSITEIT VAN PRETORIA
UNIVERSITY OF PRETORIA
YUNIBESITHI YA PRETORIA

5.6.2 Crack initiation and propagation energies

5.6.2.1 Comparison of crack initiation energies

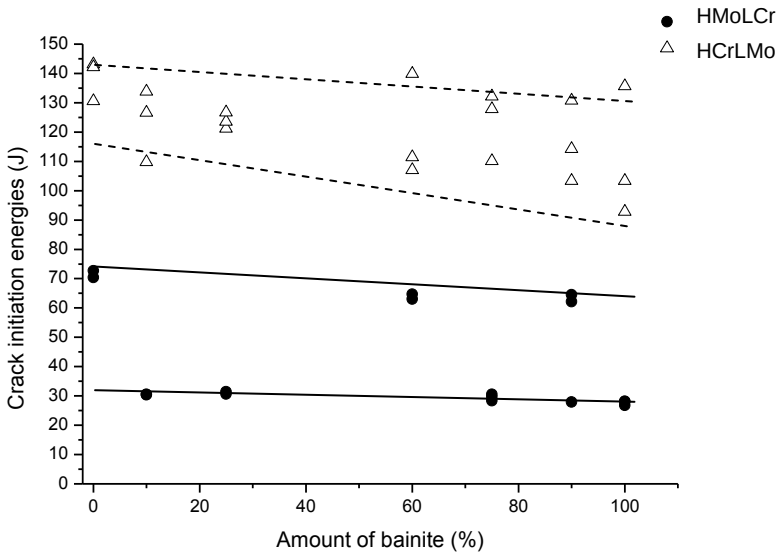

Figure 5.6.1 Plots of absolute crack initiation energies of steels HCrLMo and HMoLCr as a function of the amount of bainite in the Charpy specimens

Figure 5.6.1 shows how the absolute values of crack initiation energy vary with the amount of bainite. From the figure, it can be seen that the crack initiation energy levels for the HCrLMo steel are distinctly higher than those of the HMoLCr steel and in both steels there is an initial decrease in the crack initiation energy from 100% martensite to 10% bainite. The decreasing trend in the absolute value of crack initiation energy for the HCrLMo steel is consistent with its corresponding trend of the initiation energy as a fraction of the total as shown in Figure 4.7.11 and the crack initiation energy of steel HMoLCr is relatively independent of the quantity of bainite, with the exception of outliers at 60% and 90% bainite.

5.6.2.2 Comparison of crack propagation energies

Figure 5.6.2 shows how the absolute crack propagation energy varies with the amount of bainite for steels HMoLCr and HCrLMo.

UNIVERSITEIT VAN PRETORIA
UNIVERSITY OF PRETORIA
YUNIBESITHI YA PRETORIA

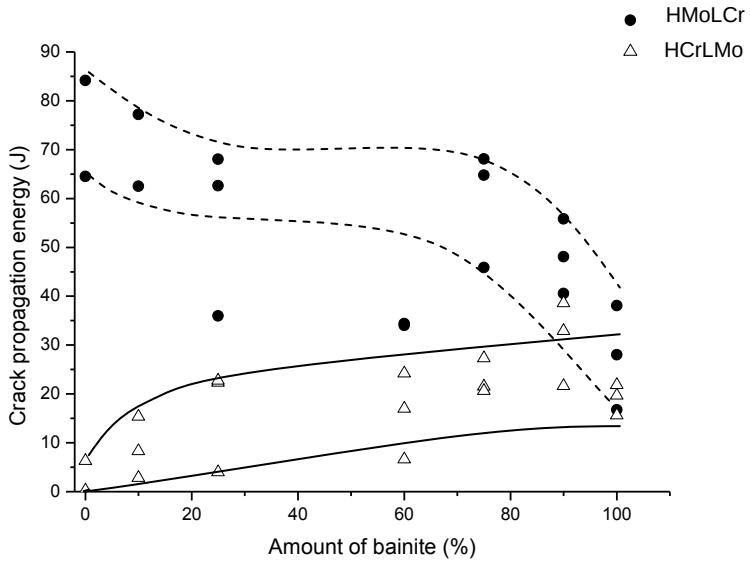

Figure 5.6.2 Plots of crack propagation energies of steels HCrLMo and HMoLCr as a function of the amount of bainite in the Charpy specimens.

The figure above shows a decrease of crack propagation energy in steel HMoLCr from roughly 85J at 100% martensite to an average of 28J at 100% bainite. However, the HCrLMo steel exhibited an increase in the crack propagation energy from the lowest energies at 100% martensite to about 20J at 100% bainite. At higher amounts of bainite, the crack propagation energies of the two steels overlap, showing that the effect of bainite on crack propagation energy in the two steels is roughly the same, although that of the HMoLCr steel remains within the higher range. The latter is consistent with the crack propagation energy fractions in Figure 4.7.9 which are between 0.4 and 0.6 at 100% bainite whereas the propagation energy fractions in steel HCrLMo (Figure 4.7.11) are ~ 0.2.

UNIVERSITEIT VAN PRETORIA
UNIVERSITY OF PRETORIA
YUNIBESITHI YA PRETORIA

5.6.2.3 Relation of microstructure to energies

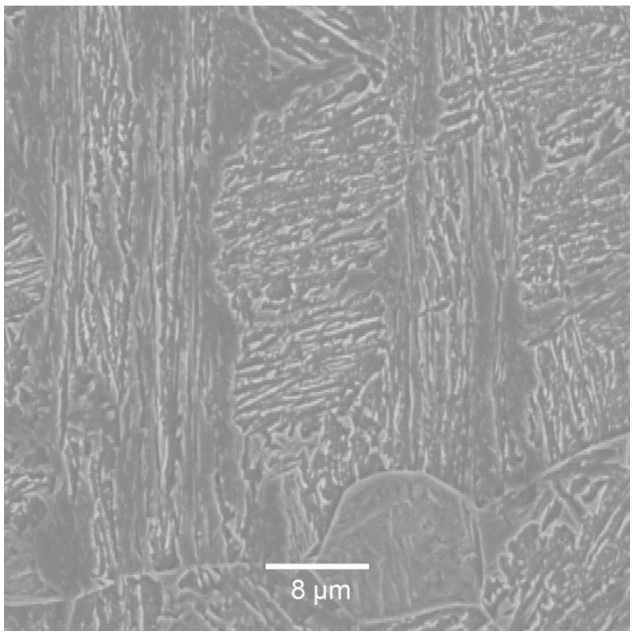

Figure 5.6.3 SEM micrograph of bainite in the HCrLMo steel with 90% bainite

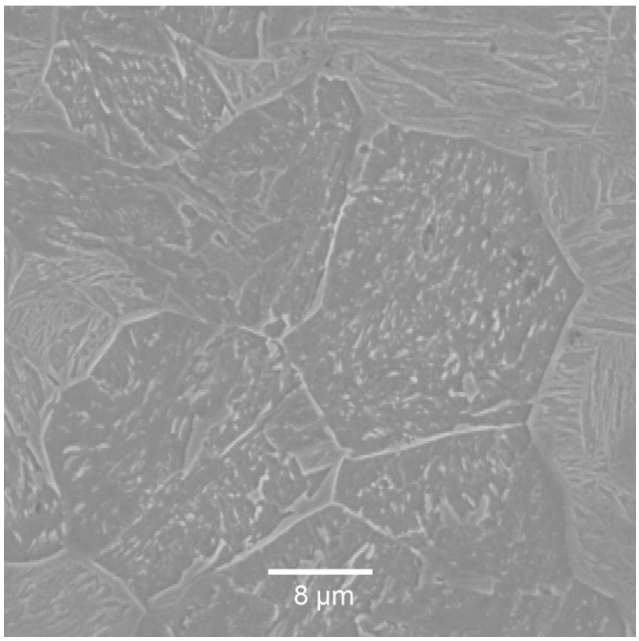

Figure 5.6.4 SEM micrograph of bainite in the HMoLCr steel. Sample contains 56% bainite.

The respective microstructures of the upper bainite in the two steels are shown in the SEM micrographs in Figures 5.6.3 and 5.6.4. In steel HCrLMo, the bainite appears to have a well-defined lath structure with longer carbide particles whereas the structure of the bainite in steel

UNIVERSITEIT VAN PRETORIA
UNIVERSITY OF PRETORIA
YUNIBESITHI YA PRETORIA

HMoLCr can be described as being similar to coalesced bainite, The term *coalesced* indicates a merging of bainite plates [83] and the lack of a distinctly lath structure in the HMoLCr steel suggests the possibility of coalesced bainite. The coalesced platelets with identical crystallographic orientation result in regions devoid of crystallographic discontinuities such as packet or block boundaries, thereby reducing the ability to deflect propagating cracks [83]. Therefore, the decrease of crack propagation energy in the HMoLCr steel shown in Figure 5.6.2 is attributed to this effect.

The high angle boundaries at block boundaries cause significant deviation of cracks. Hindrance to the movement of a microcrack that has nucleated and is now propagating in the matrix, will be most effective at high angle boundaries [84]. Generally a misorientation greater than 30° between grains is likely to lead to crack arrest. Despite the relatively larger appearance of the carbides in steel HCrLMo, the bainitic block substructure deviates propagating cracks to an appreciable extent as is evident in the increasing crack propagation energy in Figure 5.6.2. The same effect is depicted in the increasing trend of crack propagation energy fractions in Figure 4.7.11. However, the low crack propagation energy fractions of at most 0.2 are a consequence of the bainitic carbide.

The bainitic carbide can reduce the crack propagation energy as it is prone to cracking and debonding with the matrix [84], however it also acts as a point of crack initiation as a result of the stress concentration produced by its elongated shape. Thus the progressive reduction in crack initiation energy in the HCrLMo steel is related to the increase in crack initiation sites most of which are possibly due to cementite in bainite.

The Smith theory [51] for brittle fracture incorporates the effect of second phase particles on grain boundaries during cracking. The model takes into account the thickness of brittle second phase particles on grain boundaries or, as in this case, on interlath boundaries. The condition for the particle cracking is given by the expression:

$$\sigma_f > \left[\frac{4E\gamma_f}{\pi(1-\nu^2)C_o}\right]^{\frac{1}{2}} \qquad \text{eq 5.5}$$

UNIVERSITEIT VAN PRETORIA
UNIVERSITY OF PRETORIA
YUNIBESITHI YA PRETORIA

where σ_f is the fracture stress, C_o is the precipitate thickness, E is Young's Modulus, υ is Poisson's ratio and γ_f is the effective surface energy of the interface between the carbide and ferrite. The cracking of a large carbide particle is usually continued in the adjacent matrix [30]. The coarse cementite in upper bainite 'influences' the impediment of dislocations by the lath boundary [54].

Thus the elongated bainitic carbides in the HCrLMo steel samples appear to have been responsible for the reduction in the crack initiation energy, however, the lath structure of bainite in this steel was an effective barrier to the propagation of cracks. As a result, although the crack initiation energy trend decreased with increasing amounts of bainite, their absolute values were much higher than those of the HMoLCr steel samples. In addition to this, the beneficial effects of the subgrain structure showed in the increasing crack propagation energy trend of steel HCrLMo. A large proportion of the total absorbed impact energy in the HCrLMo steel (75-95%) consisted of the crack initiation energy. The absence of a distinct lath bainite structure in steel HMoLCr led to lower crack initiation energies and reduced resistance to crack propagation.

UNIVERSITEIT VAN PRETORIA
UNIVERSITY OF PRETORIA
YUNIBESITHI YA PRETORIA

6 Chapter 6: Conclusions

Two low alloy steels containing different Chromium and Molybdenum ratios were isothermally treated to form upper bainite. The growth and transformation kinetics of the steels were examined in the light of the effects of these alloying elements and it may be concluded that:

- Mo had a stronger effect than Cr on the hardenability as well as on the measured upper bainite formation with a markedly lower growth rate of bainite in the HMoLCr steel than in the HCrLMo steel.
- The undercoolings below the T_o temperatures obtained from Thermo-Calc predictions were approximately similar at 229℃ and 233℃ for the two steels.
- It was confirmed by TEM-EDS of extracted carbides from the upper bainite, that the carbide composition was not pure cementite but rather a $(Fe,Cr,Mo)_3C$ or M_3C. Substitutional diffusion or participation in the bainite transformation, therefore, has taken place in these steels transformed under these conditions;
- The lower growth rate of bainite in the HMoLCr steel compared to the HCrLMo steel may be attributed to the formation of M_3C bainitic carbide rather than pure cementitie Fe_3C. This is possible by the diffusional involvement of Cr and Mo during the formation of M_3C where diffusivity of Cr and Mo in the HMoLCr steel were found to be an order of magnitude lower than in the HCrLMo steel.
- The differences in carbon activities of 0.17 in steel HCrLMo and 0.31 in steel HMoLCr suggest the occurrence of a solute drag like effect during the growth of bainite in the HMoLCr steel.
- The progressive formation of larger amounts of bainite during isothermal transformation caused the untransformed austenite to become more enriched in carbon, thereby lowering the measured M_s temperature of this remaining austenite progressively as the bainite transformation proceeded. The carbon enrichments were within the limits set by the predicted T_o temperature.

UNIVERSITEIT VAN PRETORIA
UNIVERSITY OF PRETORIA
YUNIBESITHI YA PRETORIA

The Charpy impact energy of steels HCrLMo and HMoLCr heat treated to form 0%, 10%, 25%, 60%, 75%, 90% and 100% upper bainite was measured in an instrumented impact tester. The following conclusions were reached:

- Upper bainite in the steels HCrLMo and HMoLCr reduced the total absorbed energy with the lowest impact energy obtained in 100% bainite samples.
- The absolute crack initiation energies in the HCrLMo steel were higher than those of the HMoLCr steel.
- The plot of crack initiation energy as a fraction of the total energy in the HCrLMo steel decreased to ~ 0.8 at 100% bainite indicating that most of the total absorbed impact energy was expended on crack initiation.
- The absolute values of crack propagation energy decreased in the HMoLCr steel and increased in the HCrLMo steel with % bainite formed. In the latter, crack propagation energy increased to only 20% of the total absorbed energy.
- Microstructural examination of the bainite formed in the HCrLMo steel revealed a structure consisting of well-defined bainite packets and blocks that developed from the fragmentation of the prior austenite grains during the growth of bainite. The block structure forms an effective barrier to cracks and therefore resulted in the high crack initiation energies and the increasing trend of crack propagation energy in steel HCrLMo. The low values of crack propagation energy in this steel are attributed to the embrittling effect of bainitic carbides.
- The decreasing crack propagation energies in the HMoLCr steel are attributed to the absence of the distinct subgrain structure that was evident in the HCrLMo steel.
- Crack propagation in the HCrLMo steel consumed the least amount of energy and is therefore more critical to impact toughness than crack initiation.
- Despite the reduction in toughness, the overall Charpy impact energy for both HCrLMo and HMoLCr steel's mixed microstructures was within acceptable toughness ranges.

UNIVERSITEIT VAN PRETORIA
UNIVERSITY OF PRETORIA
YUNIBESITHI YA PRETORIA

7 References

1. S.V. Belikov, K.I. Sergeeva, O.Yu. Kornienko, I.N. Ashikhmina, A.I. Stepanov, *Special features of the formation of structure and properties of steels with heterogeneous bainite-martensite structure for oil and gas pipelines.* Metal Science and Heat Treatment, 2011. **52**: p. 581-587.

2. A. Gulyaev, Y.S. Golovanenko, and V. Zikeev, *Effect of the quantity of nonmartensitic transformation products on the resistance to fracture of quenched and tempered structural steels.* Metal Science and Heat Treatment, 1978. **20** (7): p. 584-594.

3. W. Lee, S. Hong, C. Park and S. Park, *Carbide precipitation and high-temperature strength of hot-rolled high-strength low-Alloy Steels containing Nb and Mo.* Metallurgical and Materials Transactions A, 2002. **33**: p. 1689-1698.

4. X.L. He, X.M. Wang, *Effect of boron addition on structure and properties of low carbon bainitic steels.* ISIJ International, 2002. **42** (S38-S46).

5. B. Hwang, D.W. Su, S.J Kim, *Austenitising temperature and hardenability of low-carbon boron steels.* Scripta Materialia, 2011. **64**.

6. W. Garlipp, M. Cilense, S.I. Novaes Gomes, *Austenite decomposition of C-Mn steel containing boron by continuous cooling.* Journal of Materials Processing Technology, 2001. **114**: p. 71-74.

7. Y. Jung, K. Nakai, H. Ohtsubo, Y. Ohmori, *Isothermal transformation behaviour of extremely low carbon 3%Mn - 1%Cr steels.* ISIJ International, 1994. **34** (1): p. 43-50.

8. H. Asahi, *Effects of Mo addition and austenitizing temperature on hardenability of low alloy B-added steels.* ISIJ International, 2002. **42** (10): p. 1150-1155.

9. A. Clarke, J.G. Speer, M.K. Miller, R.E. Hackenberg, D.V. Edmonds, D.K. Matlock, F.C. Rizzo, K.D. Clark, E. De Moor, *Carbon partitioning to austenite from martensite or bainite during the quench and partition (Q&P) process: A critical assessment.* Acta Materialia, 2008. **56** (1): p. 16-22.

10. F.G. Caballero, M.K. Miller, A.J. Clark, C. Gracia-Mateo, *Examination of carbon partitioning into austenite during tempering of bainite.* Scripta Materialia, 2010. **63** (4): p. 442-445.

11. J.G. Speer, D.V Edmonds, F.C. Rizzo, D.K. Matlock, *Partitioning of carbon from supersaturated plates of ferrite with application to steel processing and fundamentals*

UNIVERSITEIT VAN PRETORIA
UNIVERSITY OF PRETORIA
YUNIBESITHI YA PRETORIA

of the bainite transformation. Current Opinion in Solid State and Materials Science, 2004. **8** (3): p. 219-237.

12. A. Borgenstam, M. Hillert, J. Agren, *Metallographic evidence of carbon diffusion in the growth of bainite.* Acta Materialia, 2009. **57**: p. 3242-3252.

13. D. Quidort, Y. Brechet, *Isothermal growth kinetics of bainite in 0.5% C steels.* Acta Materialia, 2001. **49** (20): p. 4161-4170.

14. J. Wang, P.J. Van Der Wolk, S. Van Der Zwaag, *On the influence of alloying elements on the bainite reaction in low alloy steel during continuous cooling.* Journal of Materials Science 2000. **35**: p. 4393-4404.

15. D.H. Kim, J.G. Speer, H.S. Kim, B.C. De Cooman, *Observation of an isothermal transformation during quenching and partitioning processing.* Metallurgical and Materials Transactions A, 2009. **40** (9): p. 2048-2060.

16. L. Fang, W.E. Wood, D.G. Atterdge, *Identification and range quantification of steel transformation products by transformation kinetics.* Metallurgical and Materials Transactions A, 1997. **28 A**: p. 5-14.

17. D. Quidort, Y.J.M. Brechet, *A Model of isothermal and non-isothermal transformation kinetics of bainite in 0.5% C steels.* ISIJ International, 2002. **42** (9): p. 1010-1017.

18. F.G. Caballero, M.J. Santofimia, C. Gracia-Mateo, C. Gracia de Andres, *Time - temperature - transformation diagram within the bainitic temperature range in a medium carbon steel.* Materials Transactions, 2004. **45** (12): p. 3272-3281.

19. H.K.D.H. Bhadeshia, *Bainite: Overall transformation kinetics,* Journal DePhysique Colloques 1982. p. C4-443 - C4-448.

20. C. Gupta, G.K. Dey, J.K. Chakravartty, D. Srivastav, S. Banerjee, *A study of the bainite transformation in a new CrMoV steel under continuous cooling conditions.* Scripta Materialia, 2005. **53**: p. 559-564.

21. M.K. Kang, D.M. Chen, S.P. Yang, G.L. Hu, *The time-temperature-transformation diagram within the medium temperature range in some alloy steels.* Metallurgical Transactions A, 1992. **23 A**: p. 785-795.

22. H.K.D.H. Bhadeshia, D. Edmonds, *The bainite transformation in a silicon steel.* Metallurgical and Materials Transactions A, 1979. **10** (7): p. 895-907.

23. M. Takahashi, *Recent progress: kinetics of the bainite transformation in steels.* Current Opinion in Solid State and Materials Science, 2004. **8** (3): p. 213-217.

24. S.A. Sajjadi, Z.M. Zebarjad, *Isothermal transformation of austenite to bainite in high carbon steels.* Journal of Materials Processing Technology, 2007. **189**: p. 107-113.

UNIVERSITEIT VAN PRETORIA
UNIVERSITY OF PRETORIA
YUNIBESITHI YA PRETORIA

25. R.F. Hehemann, K.R. Kinsman, H.I. Aaronson, *A Debate on the Bainite Reaction.* Metallurgical Transactions, 1972. **3**: p. 1077-1094.

26. S. Chupatanakul, P. Nash, D. Chen, *Carbon partitioning during bainite transformation in 4317 type steels.* Metals and Materials International, 2006. **12** (6): p. 453-458.

27. H. Bhadeshia, *Bainite in Steels*, 2001. London, Institute of Materials.

28. Z. Ławrynowicz, A. Barbacki, *Features of bainite transformation in steels.* Advances in Materials Science, 2002. **2** (1): p. 5-32.

29. R. Bakhtiari, A. Ekrami, *The effect of bainite morphology on the mechanical properties of a high bainite dual phase (HBDP) steel.* Materials Science and Engineering A, 2009. **252**: p. 159-165.

30. A. Vashurin, E.S. Palatnikova, E.M. Ushakova, A.P. Chuchvaga , *Effect of structure on bainite embrittlement of steel 30Kh3MF.* Metal Science and Heat Treatment, 1971. **13** (11): p. 963-965.

31. A. Ali, H. Bhadeshia, *Growth rate data on bainite in alloy steels.* Materials Science and Technology, 1989. **5** (4): p. 398-402.

32. M. Hillert, *The Nature of Bainite.* ISIJ International 1995. **35** (9): p. 1134-1140.

33. H. Bhadeshia, D. Edmonds, *The mechanism of bainite formation in steels.* Acta Metallurgica, 1980. **28** (9): p. 1265-1273.

34. J.M. Prado, *Bainitc transformations of steels.* Journal of Materials Science Letters, 1986. **5**: p. 1075-1076.

35. M. Hillert, *Diffusion in Growth of Bainite.* Metallurgical and Materials Transactions A, 1994. **25**: p. 1957-1966.

36. M. Enomoto, *Partition of carbon and alloying elements during the growth of ferrous bainite.* Scripta Materialia, 2002. **47**: p. 145-149.

37. S.W. Thompson, D.J. Colvin, G. Krauss, *Continuous cooling transformations and microstructures in a low-carbon high-strength low-alloy plate steel.* Metallurgical and Materials Transactions A, 1990. **21 A**: p. 1493-1507.

38. A.A. Gorni, *Steel forming and heat-treating hand book*, 2004, Sao Vicente, Brazil.

39. Z. Ławrynowicz, *Influence of cementite precipitation on the extent of bainite reaction in Fe-Cr-Si-C steel.* Journal of Polish CIMAC Selected full texts, 2011. **6** (3): p. 137-144.

UNIVERSITEIT VAN PRETORIA
UNIVERSITY OF PRETORIA
YUNIBESITHI YA PRETORIA

40. J.W. Cahn, *The impurity-drag effect in grain boundary motion.* Acta Metallurgica, 1962. **10** (9): p. 789-798.

41. H. Aaronson, W.T. Reynolds, G. Purdy, *Coupled-solute drag effects on ferrite formation in Fe-C-X systems.* Metallurgical and Materials Transactions A, 2004. **35** (4): p. 1187-1210.

42. G. Shiflet, H. Aaronson, *Growth and overall transformation kinetics above the bay temperature in Fe-C-Mo alloys.* Metallurgical and Materials Transactions A, 1990. **21** (6): p. 1413-1432.

43. H. Goldenstein, H. Aaronson, *Overall reaction kinetics and morphology of austenite decomposition between the upper nose and the M_s of a hypoeutectoid Fe-C-Cr alloy.* Metallurgical and Materials Transactions A, 1990. **21** (6): p. 1465-1478.

44. H.I. Aaronson, W.T. Reynolds Jr, G.J. Shiflet, G. Spanos, *Bainite viewed three different ways.* Metallurgical Transactions A 1990. **21** p. 1343-1380.

45. E. Humphreys et al., *Molybdenum accumulation at ferrite: austenite interfaces during isothermal transformation of an Fe-0.24 pct C-0.93 pct Mo alloy.* Metallurgical and Materials Transactions A, 2004. **35** (4): p. 1223-1235.

46. G.J. Shiflet, R.E. Hackenberg, *Partitioning and the growth of bainite.* Scripta Materialia, 2002. **47**: p. 163-167.

47. W.T. Reynolds Jr, H.I. Aaronson, G. Spanos, *A summary of the present diffusionist views on bainite.* Materials Transactions, JIM (Japan), 1991. **32** (8): p. 737-746.

48. K. Mills, J.R. Davis, *ASM Handbook, Volume 12 - Fractography*, ASM International. p. 12-14.

49. R.J. Bishop, R.E. Smallman, *Strengthing and Toughening*. Modern Physical Metallurgy and Materials Engineering, 1999. p. 288-293.

50. A. Barbacki, *The role of bainite in shaping mechanical properties of steel.* Journal of Materials Processing Technology, 1995. **53**: p. 57-63.

51. E. Smith, *The nucleation and growth of cleavage microcracks in mild steel.* Proceedings of the conference on physical basis of yield and fracture, Institute of Physics and Physical Society, London, 1966: p 36.

52. L. Zhi-jun, S. Jun-chang, S. Hang, D. Yue-hua, Y. Cai-fu, Z. Xing, *Effect of substructure on toughness of lath martensite/bainite mixed structure in low carbon steels.* Journal of Iron and Steel Research International, 2010. **17** (11): p. 40-48.

53. D.R. Johnson, W.T. Becker, *Toughness of Tempered Upper and Lower Bainitic Microstructures in a 4150 Steel.* Journal of Materials Engineering and Perfomance, 1993. **2** (2): p. 255-263.

UNIVERSITEIT VAN PRETORIA
UNIVERSITY OF PRETORIA
YUNIBESITHI YA PRETORIA

54. D.V. Edmonds, R.C. Cochrane, *Structure-property relationships in bainitic steels.* Metallurgical Transactions A, 1990. **21**: p. 1527-1540.

55. Y. Tomita, K. Okabayashi, *Mechanical properties of 0.40 pct C - Ni - Cr - Mo High strength steel having a mixed structure of martensite and bainite.* Metallurgical Transactions A, 1985. **16 A**: p. 73-82.

56. F. Caballero, et al., *The microstructure of continuously cooled tough bainitic steels.* 2nd Int. conference super high strength steels, 2010.

57. G. Krauss, *Steels - Processing, structure and performance*, ASM International. 2005. p. 87-98. Online version available at www.knovel.org

58. N.G. Pokrovskaya, L.N. Belyakov, I.P. Zhegina, E.Y. Grigor'eva, *Influence of structure on the crack resistance of a high-strength structural steel.* Metal Science and Heat Treatment, 1997. **39** (9-10): p. 415-420

59. G.F. Vander Voort, *Metallography and Microstructures.* ASM Handbook, Volume 09, ASM International. p. 355-361.

60. *Standard Practice for Microetching Metals and Alloys.* ASTM E 407 - 99, 1999. www.astm.org

61. *Standard practice for quantitative measurement and reporting of hypoeutectoid carbon and low alloy steel phase transformation.* ASTM A1033 - 10, 2010. www.astm.org.

62. G. Béranger, G. Henry, G. Sanz, 1996. *The book of steel*. Andover, UK. Intercept. p.134.

63. *Standard test method for determining hardnenability of steel.* ASTM A255 - 02, 2002. www.astm.org.

64. T. Kop, J. Sietsma, S. Van Der Zwaag, *Dilatometric analysis of phase transformations in hypo-eutectoid steels.* Journal of Materials Science, 2001. **36** (2): p. 519-526.

65. S. Chupatanakul, P. Nash, *Dilatometric measurement of carbon enrichment in austenite during bainite transformation.* Journal of Materials Science, 2006. **41** (15): p. 4965-4969.

66. P. Hausild, I. Nedbal, C. Berdin, C. Prioul, *The Influence of ductile tearing on fracture energy in the ductile-to-brittle transition temperature range.* Materials Science and Engineering A, 2002. **335**: p. 164-174.

67. K. Mills, J.R. Davis, *Fractography*, ASM Handbook, Volume 12, ASM International.

UNIVERSITEIT VAN PRETORIA
UNIVERSITY OF PRETORIA
YUNIBESITHI YA PRETORIA

68. W.C. Leslie, 1981. *The physical metallurgy of steels.* Auckland, New York. McGraw-Hill: p. 396.

69. J.H. Woodhead, A.G. Quarrell, *Role of carbides in low-alloy creep-resisting steels.* J. Iron Steel Inst., 1965. **203** (6): p. 605-19.

70. F. Han et al., *Effect of molybdenum and chromium on hardenability of low-carbon boron-added steels.* Metals and Materials International, 2008. **14** (6): p. 667-672.

71. J. Kucera, K. Stransky, J. Dojiva, *Diffusion interaction coefficients* β_C^i *and thermodynamic interaction coefficients* ε_C^i *of carbon in alloyed austenitic steels.* Mater. Sci. Eng. A, 1990 (1): p. 75-82.

72. H. Wada, *Thermodynamics of the Fe-Cr-C system at 985 K.* Metallurgical and Materials Transactions A, 1985. **16** (8): p. 1479-1490.

73. H. Wada, *Thermodynamics of the Fe-Mo-C System at 985K.* Metallurgical Transactions A, 1986. **17 A**: p. 391-398.

74. J. Christian, *The theory of transformation in metals and alloys, Part 1.* Equilibrium and General Kinetic Theory, 1975: p. 542.

75. M. Kostic, E. Hawbolt, and L. Brown, *Growth kinetics of bainite plates and widmanstätten needles in the B′ phase of a Ag-45at. pct Cd alloy.* Metallurgical and Materials Transactions A, 1976. **7** (11): p. 1643-1653.

76. J. Cermak, J. Sopousek, K. Stransky, *Relation between carbon tracer diffusivity and carbon activity coefficient in austenitic Ni-Fe-Cr alloys.* Scr. Metall. Mater., 1993. **29** (12): p. 1581-1585.

77. T. Wada, H. Wada, J.F. Elliot, J. Chipman, *Activity of carbon and solubility of carbides in the fcc Fe-Mo-C, Fe-Cr-C and Fe-V-C alloys.* Metallurgical Transactions, 1972. **3**: p. 2865-2872.

78. S.J. Lee, D.K. Matlock, and C.J. Van Tyne, *Carbon diffusivity in multi-component austenite.* Scripta Materialia, 2011. **64** (9): p. 805-808.

79. J.A. Lobo, G.H. Geiger, *Thermodynamics of carbon in austenite and Fe-Mo austenite.* Metallurgical Transactions A, 1976. **7 A**: p. 1359-1364.

80. J. Ågren, *Computer simulations of the austenite/ferrite diffusional transformations in low alloyed steels.* Acta Metallurgica, 1982. **30** (4): p. 841-851.

81. P. Thibaux, A. Metenier, C. Xhoffer, *Carbon diffusion measurement in austenite in the temperature range 500* ℃ *to 900* ℃. Metallurgical and Materials Transactions A, 2007. **38** (6): p. 1169-1176.

UNIVERSITEIT VAN PRETORIA
UNIVERSITY OF PRETORIA
YUNIBESITHI YA PRETORIA

82. X.Z. Zhang, J.F. Knott, *Cleavage fracture in bainitic and martensitic microstructures.* Acta Metallurgica, 1999. **47** (12): p. 3483-3495.

83. F. Caballero et al., *Toughness deterioration in advanced high strength bainitic steels.* Materials Science and Engineering A, 2009. **525** (1): p. 87-95.

84. L. Lan, C.Qui, D. Zhao, X. Gao, L. Du, *Microstructural characteristics and toughness of the simulated coarse grained heat affected zone of high strength low larbon bainitic steel.* Materials Science and Engineering A, 2011. **529**: p. 192-200.

85 C.J. McMahon, M. Cohen, *Initiation of cleavage in polycrystalline iron.* Acta Metallurgica, 1965. **13**: p. 591-604